

76093

COMPUTER SIMULATION OF DYNAMIC
BEHAVIOR OF PNEUMATIC TIRES

A THESIS SUBMITTED TO
THE GRADUATE SCHOOL OF NATURAL AND APPLIED SCIENCES
OF
MIDDLE EAST TECHNICAL UNIVERSITY

BY

ERGİN TÖNÜK

IN PARTIAL FULFILLMENT OF THE REQUIREMENTS FOR THE DEGREE OF
DOCTOR OF PHILOSOPHY
IN
THE DEPARTMENT OF MECHANICAL ENGINEERING

SEPTEMBER 1998

Approval of the Graduate School of Natural and Applied Sciences



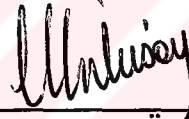
Prof. Dr. Fayfur ÖZTÜRK
Director

I certify that this thesis satisfies all the requirements as a thesis for the degree of Doctor of Philosophy.



Prof. Dr. Ediz RAYKOÇ
Head of Department

This is to certify that we have read this thesis and that in our opinion it is fully adequate, in scope and quality, as a thesis for the degree of Doctor of Philosophy.



Prof. Dr. Y. Samim ÜNLÜSOY
Supervisor

Examining Committee Members

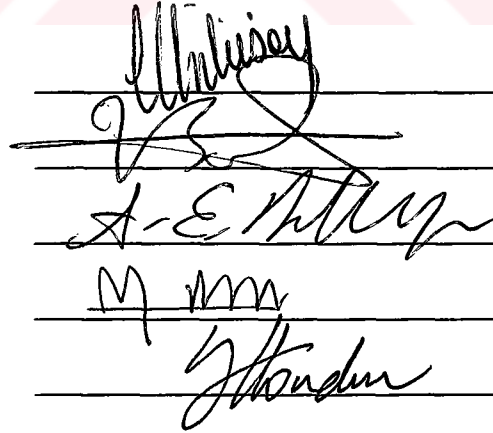
Prof. Dr. Y. Samim ÜNLÜSOY

Prof. Dr. A. Demir BAYKA

Prof. Dr. A. Erman TEKKAYA

Prof. Dr. Yalçın MENGİ

Prof. Dr. Yaşar HONDUR



ABSTRACT

COMPUTER SIMULATION OF DYNAMIC BEHAVIOR OF PNEUMATIC TIRES

Tönük, Ergin

Ph. D., Department of Mechanical Engineering

Supervisor: Prof. Dr. Y. Samim Ünlüsoy

September 1998, 185 pages

To predict the cornering characteristics of a pneumatic tire during the design stage, a detailed finite element model of the tire is constructed. The nonlinear stress-strain relationship of rubber, the reinforcement of the tire, large displacements and strains induced during normal service conditions, frictional contact with ground are modeled. To check the validity of the computer model, an external drum type tire testing setup is designed and constructed.

A static tire model is constructed first and its vertical force-deflection characteristics and contact patch shape are compared with the experimental tire to check the accuracy of the finite element model. Quasi-static cornering tire model is constructed to simulate the low-speed cornering behavior. Centrifugal load is added to the model to simulate the medium speed cornering behavior.

Comparison of computer model results and tire test results show that finite element modeling can be used to predict the cornering properties of a tire during early design stages, reducing the time and effort for prototyping and testing.

Keywords: Tire Cornering, Cornering Force, Pneumatic Tires, Tire Testing, Nonlinear Finite Element Analysis

ÖZ

OTOMOBİL LASTİKLERİN DİNAMİK DAVRANIŞLARININ BİLGİSAYARDA MODELLENMESİ

Tönük, Ergin

Doktora, Makina Mühendisliği Bölümü

Tez Yöneticisi: Prof. Dr. Y. Samim Ünlüsoy

Eylül 1998, 185 sayfa

Otomobil lastiklerinin viraj karakteristiklerini tasarım aşamasında belirlemek için ayrıntılı bir sonlu elemanlar modeli hazırlanmıştır. Kauçuk malzemenin doğrusal olmayan malzeme davranışı, lastiğin içinde bulunan karkas malzemesi, normal çalışma sırasında görülen büyük yer değiştirme ve gerilmelerle yerle lastik arasındaki sürtünmeli temas modellenmiştir. Modelden alınan sonuçların sınanması için tamburlu bir lastik deney düzeneği tasarlanmış ve kurulmuştur.

İlk olarak statik bir lastik modeli hazırlanmış, dikey yük-sehim ve temas alanı deneysel lastikle karşılaştırılmıştır. Sanki-statik yuvarlanan lastik modeliyle düşük hızlarda lastiğin viraj davranışı modellenmiştir. Lastik üzerine merkezkaç yük uygulanmasıyla hızın artmasının etkisi de modele katılmıştır.

Bilgisayar modelinden alınan sonuçların deneysel sonuçlarla karşılaştırılması, sonlu elemanlar yönteminin lastiklerin viraj karakteristiklerinin tasarım aşamasında kestirilebilmesi için kullanılabileceğini, böylelikle prototip üretimi ve deneyler için harcanan zaman ve paranın azaltılabileceğini göstermiştir.

Anahtar Kelimeler: Lastik Viraj Karakteristikleri, Viraj Kuvveti, Otomobil Lastiği, Lastik Deneyleri, Nonlineer Sonlu Elemanlar Yöntemi

ACKNOWLEDGMENTS

I would like to express my sincere thanks to my thesis supervisor Prof. Dr. Y. Samim Ünlüsoy for offering me this topic and for his perfect guidance and insight through the long working period. The support by the Ex-Chairman of the Mechanical Engineering Department, Prof. Dr. Rüknettin Oskay for the construction of the tire test machine is greatly appreciated. I am grateful to Mr. Pehril Yavuzuğruk, the technical staff of the Automotive Laboratory for his non-diminishing power and precise work, besides his assistance. The following staff from Turkish Governmental Railways, where the drum of the tire test machine is supplied worths mentioning: Mr. Fuat Açıkgöz, Director of Ankara Railway Factory, Mr. Zevki Saka, Assistant Director of Ankara Railway Factory, Mr. Erol Arıkan, Director of Diesel Locomotive Division, Mr. Mehmet Özkara, Director of Production Group, Mr. Metin Şahin, Mechanical Engineer and the staff who worked fastly and precisely. Mr. Mehmet Karabatur from Middle East Bearings, supplied the bearings of the tire testing machine. Prof. Dr. Necip Berme, the designer and producer of the six axis force transducer of the testing machine assisted the study by donating some portion of the transducer by Bertec Corporation. The Machinshop Staff; Mr. Mehmet Çakmak for his consultance, Mr. Hakverdi Yalçın and Mr. Taner Korkmaz for precise welding work, Mr. Yusuf Papur and Mr. Saim Seloğlu for precise chip removal machining and Mr. Mustafa Bulduklar for supplying the necessary tools, worths to mention here. The administrator of the workstation on which ABAQUS Finite Element Software is

installed, Mr. Umut Ali Yener (M.S.), had great help while working on mech1. While working on finite element software MARC, Dr. Robert Beck of MARC Software Deutschland GmbH and Mr. Aydın Kuntay of BİAS Engineering, the Turkey Representative of MARC provided great help. The Computer Center staff, Mr. Çağrı Çöltekin and Mr. Melih Bitim, the administrators of Nautilus workstations, Miss Filiz Yılmaz and Miss Mehtap Semiz, the hotline staff, had great help in solving technical problems about computers. Prof. Dr. A. Erman Tekkaya provided help in both theoretical aspects of finite element modeling and in MARC implementation. Finally I would like to thank to the thesis supervision comitee members Prof. Dr. Demir Bayka and Prof. Dr. Yalçın Mengi for their help and support during the progress of this thesis. The support of Professors Eres Söylemez, Turgut Tümer, Engin Kılıç and my friends Dr. Can Saygın, Mr. Cenk Güler and Mr. Ümit Coşkun also helped me.

The research is partly funded by Middle East Technical University Research Fund AFP-96-03-02-01 and The Scientific and Technical Research Council of Turkey (TÜBİTAK) MİSAG-86 projects, without which the experimental part of the research would be impossible. ABAQUS Finite Element Software is supplied by the CAD/CAM Robotics Center of the Middle East Technical University.

TABLE OF CONTENTS

ABSTRACT	iii
ÖZ	iv
ACKNOWLEDGMENTS	v
TABLE OF CONTENTS	vii
LIST OF TABLES	xv
LIST OF FIGURES	xvii
LIST OF SYMBOLS	xxiii
CHAPTER	
1. INTRODUCTION	1
1.1 Introduction	1
1.2 Functions of Tire in a Non Guided Ground Motor Vehicle	1
1.3 Brief Development History of Pneumatic Tires	1
1.4 Modern Tire Types, Materials, and Nomenclature	3
1.5 Handling Behavior of Tires	8
1.6 Need for a Tire Model	12

2. LITERATURE SURVEY	14
2.1 Introduction	14
2.2 Analytical and Empirical Tire Models for Cornering Analysis and Their Verification by Experimental Data ...	16
2.2.1 Experimental Data Used	16
2.2.2 Linear Spring Analogy	18
2.2.3 Model by Gim and Nikravesch	19
2.2.4 Model by Stribersky and Fancher	22
2.2.5 Model by Fancher and Bareket	23
2.2.6 Model by Dugoff	26
2.2.7 Polynomial Tire Model	28
2.2.8 Magic Tire Formula by Pacejka	30
2.2.9 Model by Segel	31
2.2.10 Model by Allen	33
2.3 Physical Tire Models in Literature	36
2.4 Specifications of a <i>Perfect</i> Tire Model	41
2.5 Need for Model Verification	42
2.6 Tire Testing Devices Found in Literature	43
2.6.1 Flat Bed Tire Testing Machines	44
2.6.2 Flat Surface Tire Testing Machines	45
2.6.3 Drum Type Tire Testing Machines	48

a) External Drum Tire Testing Machines	48
b) Internal Drum Tire Testing Machines	50
2.6.4 On Road (Mobile) Tire Testing Devices	51
3. TIRE TESTING SETUP AND EXPERIMENTS	55
3.1 Introduction	55
3.2 Properties of Test Setup	55
3.3 Design of the Test Setup	57
3.4 Running Procedure of the Test Setup	59
3.4.1 Mechanical Preparations	59
3.4.2 Electronic Preparations	61
3.4.3 Programming of Speed Control Unit	62
3.4.4 Technical Specifications of Force Transducer ..	64
3.4.5 Tire Testing	66
3.5 Static Tire Tests	67
3.5.1 Tests on Flat Surface	67
3.5.2 Tests on Curved Surface	69
3.6 Initial Cornering Test Results of the Setup	69
3.7 Error Analysis of Test Setup	73
3.7.1 Tire Positioning Errors	73
3.7.2 Force Transducer Accuracy	73

3.7.3 Electrical Noise	73
3.7.4 Analog-to-Digital Conversion Accuracy	73
3.7.5 Accuracy of a Data point on Carpet Plot	74
3.8 Test Results	75
3.8.1 Low Speed Cornering Test	75
3.8.2 Effect of Inflation Pressure on Cornering Characteristics	76
3.8.3 Effect of Test Speed on Cornering Characteristics	77
4. TIRE MATERIAL REPRESENTATIONS AND ELEMENT FORMULATIONS IN FINITE ELEMENT MODELING ...	79
4.1 Introduction	79
4.2 Geometric Nonlinearities	80
4.2.1 Large Displacements and Large Strains	80
4.2.2 Pressure Loading in Large Displacement and Rotation Analysis	83
4.2.3 Finite Element Formulation for Geometric Nonlinearities	84
4.3 Modeling the Composite Material Properties and Anisotropic Material Behavior	85
4.3.1 Some Approaches in Literature to Model Unidirectional Long Fiber Composites	85
4.3.2 Initiation of Rebar Concept in Finite Element Formulation	87

4.3.3 Unidirectional Fibrous Composite Material Modeling in ABAQUS/Standard: *REBAR Option	88
4.3.4 Unidirectional Fibrous Composite Material Modeling in MARC: Rebar Elements	90
4.3.5 Further Enhancements to Rebar Concept, Record Elements	94
4.4 Nonlinear Elasticity and Nearly Incompressible Behavior of Rubber	95
4.4.1 Introductory Definitions	95
4.4.2 Time-Independent Nonlinear Elasticity of Rubber	96
4.4.3 Herrmann Formulation for Incompressible and Nearly Incompressible Material Representation .	101
4.5 Contact and Friction Models in Finite Element Programs .	103
4.5.1 Deformable to Rigid Body Contact in ABAQUS	103
4.5.2 Coulomb Friction Model in ABAQUS	104
4.5.3 Deformable to Rigid Body Contact Model in MARC	104
4.5.4 Friction Models in MARC	105
4.6 Redefining a Mesh on Deformed Geometry	108
4.7 Modeling Centrifugal Loads in Cornering Analysis	110
5. STATIC FINITE ELEMENT MODELING OF TIRE	111
5.1 Introduction	111

5.2 Tire Modeled	111
5.3 Coarse Mesh Tire Model	112
5.3.1 Mesh	112
5.3.2 Inflation Analysis	114
5.3.3 Ground Contact Analysis	115
5.3.4 Effect of Tire Tread to Contact Patch	119
5.4 Fine Mesh Tire Model	121
5.4.1 Mesh	121
5.4.2 Inflation Analysis	123
5.4.3 Ground Contact Analysis	123
5.4.4 Effect of Tire Tread to Contact Patch	124
5.5 Attempts for More Precise Models	126
5.5.1 Axisymmetric Inflation and Rim Seating Models	126
5.5.2 Ground Contact Model	131
5.6 Conclusions About Static Tire Models	134
6. MODELING THE CORNERING BEHAVIOR OF TIRE	135
6.1 Introduction	135
6.2 Remeshing Using MARC's Rezoning Capability	135
6.3 Quasi-Static Cornering Tire Model	137
6.3.1 Coarse Mesh Cornering Model on Flat Surface	137

6.3.2 Coarse Mesh Quasi-Static Cornering Model on Test Machine's Drum	138
6.4 Conclusions about Quasi-Static Cornering Tire Models ..	145
7. CONCLUSION AND RECOMMENDATIONS FOR FURTHER STUDIES	147
7.1 Introduction	147
7.2 Conclusions about Present Work	147
7.2.1 Tire Testing Setup	147
7.2.2 Static Tire Models	148
7.2.3 Cornering Tire Models	149
7.3 Recommendations for Further Studies	149
7.3.1 Recommendations for Increased Model Accuracy	149
7.3.2 Recommendations for Increased Computational Efficiency	151
7.3.3 Improvements on Tire Testing Setup	151
APPENDIX	
A. REBAR SUBROUTINES IN MARC	153
A.1 Introduction	153
A.2 General Structure of REBAR Subroutine and BelongToSet Function.....	154

A.2.1 REBAR Subroutine for MARC Versions K6.x Family	154
A.2.2 REBAR Subroutine for MARC Versions K7.x Family	155
A.2.3 BelongToSet Function	155
A.2.4 Determination of Current Positions of Nodes ...	157
A.2.5 Determination of Equivalent Layer Thickness ..	158
A.3 Axisymmetric Rebar Subroutine for Quadratic Elements .	158
A.4 Rebar Subroutines for Three-Dimensional Solid Elements	162
A.4.1 Rebar Subroutine for 20 Node Continuum Element	163
A.4.2 Rebar Subroutine for 8 Node Continuum Element	167
 B. ANALYSIS OPTIONS IN MARC FOR CORNERING ANALYSIS	 172
 REFERENCES	 175
 CURRICULUM VITAE	 183

LIST OF TABLES

TABLE

2.1	Properties of the Experimental Tire	17
2.2	Cornering Stiffness at 28 psi Inflation Pressure	17
2.3	Polynomial Model Coefficients of G78-15 Tire	29
2.4	Coefficients of Pacejka Model for Firestone P195/70R14 Tire with 26 psi Inflation Pressure	31
2.5	Segel Model Coefficients	32
2.6	Saturation Function Coefficients for Allen Model	33
2.7	Tire Parameters for Allen Model	35
2.8	Laboratory Tire Testing Devices to Determine Handling Properties of Tires	54
2.9	On Road Tire Testing Devices to Determine Handling Properties of Tires	54
3.1	Motor Shaft and Corresponding Road Speeds	62
3.2	The Necessary Parameters of the Speed Control Unit	64
5.1	Properties of 155 R 13 78 S Tire	112

5.2	Material Properties	115
5.3	Mooney-Rivlin Material Constants of Rubber	127
5.4	Elastic Properties of Reinforcing Materials	128
5.5	Geometric Properties of Reinforcing Materials	128

FOR INFORMATION ONLY
BUKUMANSUN MELAKA



LIST OF FIGURES

FIGURE

1.1	Basic Functions of Modern Tire	2
1.2	The Common Nomenclature used for Pneumatic Tires	3
1.3	Two Basic Types of Tire Carcass Constructions, Cross Ply and Bias Belted and Radial Tires	4
1.4	Tread Nomenclature	6
1.5	Some Different Tread Patterns	7
1.6	Automobile Tire Designation	8
1.7	Commercial Vehicle Tire Designation	8
1.8	SAE Tire Coordinate Axes	10
1.9	Lateral Wheel Slip Phenomena	11
1.10	Cornering Force Characteristics of a Typical Passenger Car Tire.	11
2.1	Experimental Cornering Force Characteristics of G78-15 Tire ..	17
2.2	Lateral Deformation of Contact Patch and Lateral Stress due to Pure Slip Angle	19
2.3	Cornering Force Characteristics of G78-15 Tire by Gim and Nikravesh Model	21

2.4	Cornering Force Characteristics of G78-15 Tire by Stribersky and Fancher Model	23
2.5	Pressure Distribution along the Contact Patch	24
2.6	Cornering Force Characteristics of G78-15 Tire by Fancher and Bareket Model	26
2.7	Cornering Force Characteristics of G78-15 Tire by Dugoff Model	28
2.8	Cornering Force Characteristics of G78-15 Tire by Polynomial Model	29
2.9	Cornering Force Characteristics of a Firestone P195/70R14 Tire by Pacejka Model	31
2.10	Cornering Force Characteristics of G78-15 Tire by Segel Model.	33
2.11	Cornering Force Characteristics of G78-15 Tire by Allen Model.	35
2.12	Flat Bed Tire Testing Machine	45
2.13	Flat Surface Tire Testing Machine	46
2.14	External Drum Tire Testing Machine	49
2.15	Internal Drum Tire Testing Machine	50
2.16	Cornering Trailer	51
3.1	General View of Tire Testing Setup	58
3.2	The Vertical Tire Motion under Load	58
3.3	Laser Pointer for Slip Angle Adjustment	60
3.4	The Lower Two T-Slots for Slip and Camber Angle Adjustments	60

3.5	Hydraulic Jack for Lifting the Tire	61
3.6	The Control Pod of Speed Controller	63
3.7	Force Transducer Coordinate Axes	65
3.8	Transducer and SAE Coordinate Axes	66
3.9	Experimental Load-Deflection Characteristics of 155 R 13	68
3.10	Contact Patch of 155R13 on Flat Surface with 180 kPa Inflation Pressure and 4160 N Vertical Load	68
3.11	Load-Deflection Characteristics of Old and New 155R13 Tires on Test Drum	69
3.12	Cornering Force Characteristics of 175/70R13 at 7.4 km/h Speed with 2 Degrees Slip Angle Incrementation	70
3.13	Cornering Force Characteristics of 175/70R13 at 24.6 km/h Speed with 2 Degree Slip Angle Incrementation	70
3.14	The First Detailed Tire Testing of 175/70R13	71
3.15	Schematic Representation of Optical Positioning Instrument ...	72
3.16	The First Test with Laser Beam Positioning Device	72
3.17	Data Points and Their Dispersion on Carpet Plot	75
3.18	Cornering Force Characteristics of 155R13 at 180 kPa Cold Inflation Pressure and 10 km/h Road Speed	76
3.19	Effect of Cold Inflation Pressure on Cornering Characteristics ..	77
3.20	Tread Damage After High Speed High Slip Angle Test	78
3.21	Effect of Roadway Speed on Cornering Properties	78

4.1	Construction of a Typical Radial Tire	80
4.2	Axisymmetric, Linear and Quadratic Rebar Elements in MARC .	92
4.3	Three Dimensional, Linear and Quadratic Rebar Elements in MARC	92
4.4	Theoretical and Experimental Stress Stretch Curve for Natural Rubber	99
4.5	ASTM Tension Test Specimen	101
4.6	Regularized Coulomb Friction for Various C Values	107
4.7	Stick-Slip Model in MARC	107
5.1	Profile of Coarse Finite Element Mesh Used	112
5.2	Carcass Construction of Steel Belted Radial Tire	114
5.3	Coarse Mesh of Static Tire Model	115
5.4	Load-Deflection Characteristics of 155R13 Tire with Modified Material Elastic Constants	116
5.5	Load-Deflection Characteristics of 155 R 13 Tire with $\pm 10^\circ$ Tread Carcass	117
5.6	Load Deflection Characteristics of Textile Belted Radial Tire ...	117
5.7	Load Deflection Characteristics of Cross Ply Tire	118
5.8	Comparison of Load Deflection Characteristics of Steel and Textile Belted Radial and Cross Ply Tires	118
5.9	Contact Patch Pressure Distribution of Different Tire Constructions	119

5.10	Contact Pressure Distribution of a 195/70R14 Tire in Static Case and in Low Speed Rolling by Pottinger Experimentally ...	120
5.11	Load Deflection Characteristics of Treaded 155 R 13 Tire	120
5.12	Comparison of Smooth and Treaded Tire Models with Experimental Data at 180 kPa Inflation Pressure	121
5.13	Profile of Fine Finite Element Mesh Used	122
5.14	Finer Finite Element Mesh of Static Tire Model	123
5.15	Load-Deflection Characteristics of 155R13 Tire with Finer Mesh	124
5.16	Simplified Tread Pattern Geometry Introduced to Contact Patch	125
5.17	Load Deflection Characteristics of Treaded 155R13 Tire	125
5.18	Comparison of Load Deflection Characteristics of Smooth and Treaded 155R13 with Experimental Data	126
5.19	Axisymmetric Tire Model	127
5.20	Location of Rubber Material in Tire	128
5.21	Location of Reinforcing Materials	129
5.22	155R13 Tire Mounted on 4, 4.5, 5 and 5.5 inch Rims	130
5.23	155R13 with 0° Textile Breaker Ply Added on 4.5 and 5 inch Rims	130
5.24	155R13 with 4 Textile Breaker Plies on 4.5 and 5 inch Rims ...	131
5.25	Tire Sector for Ground Contact Analysis	132
5.26	Quarter Tire Model for Ground Contact Analysis	132
5.27	Simplified Tread Pattern	133
5.28	Force-Deflection Characteristics on the Drum of the Test Machine	133

6.1 Tire Model For Rezoning	136
6.2 Variation of Cornering Force With Distance Rolled	138
6.3 Tire Model Sector on the Drum	139
6.4 Rendered Picture of Tire Model on Drum	139
6.5 Tire Mesh	140
6.6 Kinematic Inversion to Keep Tire Completely Fixed and Drum Rotating around the Tire	141
6.7 Loci of Two Nodes Defining Drum Center	142
6.8 Deformations on a Cornering Tire	144
6.9 Cornering Force Characteristics of 155R13 from Computer Model	144
7.1 Deformed Photograph of 155R13	148
A.1 Radial Tire Reinforcement	154
A.2 Body Ply Reinforcement Direction in Axisymmetric Model ...	160
A.3 Tread Ply Reinforcement Direction in Axisymmetric Model ...	161
A.4 Body Ply Reinforcement Direction in Three-Dimensional Model	163
A.5 Tread Ply Reinforcement Direction in Three-Dimensional Model	164
A.6 Triads Determined by Closest Edge	168

LIST OF SYMBOLS

Material Formulation

UPPER CASE LETTERS	Refer the quantity in initial (undeformed) configuration
lower case letters	Refer the quantity in present (current, deformed) configuration
Bold	Vector or tensor quantities
Light	Scalar quantities
$\delta(.)$	Variation (virtual quantity)
ε	Engineering strain
λ	Stretch (ratio)
μ	Coefficient of friction in Coulomb friction model
$\Pi(.)$	Functional
σ, σ_{ij}	True (Cauchy) stress tensor, tensor components
$(.)_{\theta}$	Angular component in axisymmetric models
$(.)_j$	Partial derivative of $(.)$ in j direction, $\frac{\partial(.)}{\partial x_j}$
$(.)_A$	Axial quantity
$(.)_R$	Radial component in axisymmetric models

$\sigma_1, \sigma_2, \sigma_3$	Principal stresses (in descending order)
δ_{ij}	Kronecker delta function (1 if $i = j$, 0 otherwise)
ε_{ijk}	Permutation symbol (1 if i, j, k any cyclic combination of 1, 2, 3; -1 if i, j, k any cyclic combination of 3, 2, 1; 0 otherwise)
β_{ijk}^0	Constant symmetric shape function gradient
β_{ijk}^u	Displacement dependent symmetric shape function gradient
σ_n	Normal contact stress
α_n	Material coefficients in Ogden model
μ_n	Material coefficients in Ogden model
A_r	Cross sectional area of reinforcement
$C, C_{10}, C_{01}, \text{etc.}$	Material constants for different types of Mooney-Rivlin models
C, C_{ij}	Right Cauchy-Green deformation tensor, tensor components
D_{ijmn}	Material tangent coefficients
E	Young's (elastic) modulus of linear elastic material
E, E_{ij}	Green-Lagrange strain tensor, tensor components.
F	Force magnitude
F, F_{ij}	Deformation gradient tensor, tensor components
G	Shear modulus of linear elastic material
g, h	Surface parametric coordinates
I_1, I_2, I_3	Strain invariants

J	Jackobian of deformation
K	Bulk modulus in Ogden model
L	Current length of the test specimen
L_0	Initial length of the test specimen
L_{ijkl}	The most general linear elastic material coefficients
n	Surface normal (outward unit normal unless stated otherwise)
p	Pressure
\mathbf{Q}, Q_i	Force vector, vector components per unit volume in undeformed configuration
\mathbf{q}, q_i	Force vector, vector components per unit volume in deformed configuration
R	Radius, yarn radius for twisted cords
r_1, r_2	Surface parametric coordinates of reinforcement
S	Material boundary in undeformed configuration
s	Material boundary in deformed configuration
\mathbf{S}, S_{ij}	Second Piola-Kirchoff stress tensor, tensor components
S_r	Spacing between reinforcing elements
T	Twist per unit length of twisted cords
\mathbf{T}, T_i	Surface traction vector, vector components per unit area of undeformed configuration
\mathbf{t}, t_i	Surface traction vector, vector components per unit area of deformed configuration

\mathbf{u}, u_i	Displacement vector, vector components (from undeformed to deformed position)
V	Material volume in undeformed configuration
v	Material volume in deformed configuration
W	Elastic strain energy (Helmholtz free energy at constant temperature)
W_N	Gauss weighing factor
\mathbf{x}, x_i	Current (deformed) position vector, vector components
\mathbf{X}, X_i	Initial (undeformed) position vector, vector components

Finite Element Formulation

ν	Poisson's ratio
τ	Frictional shear stress
$(.)^e$ (superscript)	Elemental quantity
$(.)^{el}$	Elastic part of the quantity
$(.)^L$	Linear part of the quantity
$(.)^{nel}$	Non-elastic part of the quantity
$(.)^{NL}$	Nonlinear part of the quantity
<u> </u> (underlined)	Quantity referred to the nodes of a particular element
\mathbf{a}, a_i	Unit tangent vector, vector components of reinforcement
\mathbf{B}, B_{ij}	Beta matrix, elements of beta matrix in finite element formulation

\underline{B}_{ij}^e	Partial derivative of interpolation (shape) function
H	Herrmann mean pressure variable
I	Dilatation restraint force
\underline{K}^e	Elastic stiffness matrix
\underline{K}^g	Geometric stiffness matrix
\underline{K}^s	Initial stress stiffness matrix
\underline{K}^t	Tangent stiffness matrix
$\underline{N}_i^e(\mathbf{X}_k)$	Interpolation (shape) function matrix (degree-of-freedom per node rows and degree-of-freedom per element columns)
\underline{P}	Nodal load vector to account for external body forces and surface tractions
Q	Internal load vector
\underline{u}^e	Nodal displacement vector of the element (degree-of-freedom per element rows)

Tire Mechanics

α	Slip angle
θ	Equivalent slip angle
γ	Camber angle
μ	Coefficient of friction
λ	Nondimensional equivalent slip parameter
μ_0	Coefficient of friction between tire and road at zero speed

μ_y	Lateral coefficient of friction
θ_y	Equivalent slip angle of magic tire formula
$\sigma_y^{(a)}$	Surface shear traction at the contact patch in adhesion region
$\sigma_y^{(s)}$	Surface shear traction at the contact patch in sliding region
A_0, A_1, A_2	Three constants of tire model by Segel
A_{ij}	Vertical force dependent constants of C_i of polynomial tire model
a_p	Contact patch length in operating conditions
a_{p0}	Contact patch length in design conditions
A_y, B_y, C_y, E_y	Constants of magic tire formula
C_α	Cornering Stiffness
C_0, C_1, C_2, C_3	Constants of polynomial tire model
c_1, c_2, c_3, c_4	Four constants of saturation function of tire model by Allen
C_s	Cornering stiffness
$f(\sigma), \sigma$	Saturation function of composite slip and composite slip in Allen tire model
F_c	Cornering force
F_x	Tractive/braking force
F_y	Lateral force
F_z	Normal force
F_{ZT}	Tire design load at operating pressure

$g(\bar{s}_i)$	Saturation function in Segel tire model
k	Stiffness
K	Nondimensional cornering stiffness
K_c	Longitudinal stiffness coefficient in Allen tire model
K_s	Lateral stiffness coefficient
k_y	Lateral stiffness
L	Length, length of contact patch
M_x	Overturning moment
M_y	Rolling resistance moment
M_z	(Self) Aligning torque
s	Longitudinal slip ratio
\bar{s}_i	Slip parameter in Segel tire model
S_α	Diagonal slip in Gim and Nikravesh tire model
S_h, S_v	Horizontal and vertical shift factors of magic tire formula
SN	Tire skid number
S_n	Normalizes slip in Gim and Nikravesh tire model
S_T	Total slip
S_x	Longitudinal slip
T_p	Tire inflation pressure in Allen tire model
T_w	Tread width

W	Tire vertical load
w	Average width of the contact patch in tire models
x	Direction of wheel heading
x_s	Longitudinal position of a tread point in contact patch
y	Lateral tire direction parallel to axle
z	Vertical tire direction

Tire Testing Setup

F_x, F_y, F_z	Three orthogonal forces measured by the force transducer
h	Horizontal distance of contact patch center to the transducer top plate center
M_x, M_y, M_z	Three orthogonal moments measured by the force transducer
S_i	Voltages coming from the six-axis force transducer
v	Vertical distance of contact patch center to the transducer top plate center

CHAPTER 1

INTRODUCTION

1.1 Introduction

In this Chapter, functions of tires in nonguided ground vehicles, brief development history of pneumatic tires, modern tire types and tire nomenclature, handling behavior of pneumatic tires, and the need for a tire model are briefly explained.

1.2 Functions of Tire in a Nonguided Ground Motor Vehicle

Tire, being the common component of nearly all nonguided ground motor vehicles, serves mainly for four distinct functions. A tire being the only connection between the vehicle and the ground, supports the weight of the vehicle, develops tractive forces to propel and braking forces to stop the vehicle, and develops lateral forces to steer the vehicle. A tire takes part in isolating the vehicle body against the transmission of vibrations due to the irregular road surface. The functions of a modern tire are summarized in Figure 1.1.

1.3 Brief Development History of Pneumatic Tires

The history of pneumatic tires is very recent compared to that of wheels which were invented more than 5000 years ago in Asia by the Sumerians. The

history of wheels may be found in İpek (1969). The first rubber tires were solid. The first pneumatic tire was patented in 1845 by a Scottish engineer, Robert Thomson. He intended to reduce the tractive effort to pull the horse carriages and to reduce the noise when they are in motion. This tire had a tube of rubberized canvas covered by a leather case which was bolted to the wooden rim. The same need led John Boyd Dunlop, a Scottish veterinary surgeon, to re-invent the pneumatic tire in 1888 for his son's tricycle.

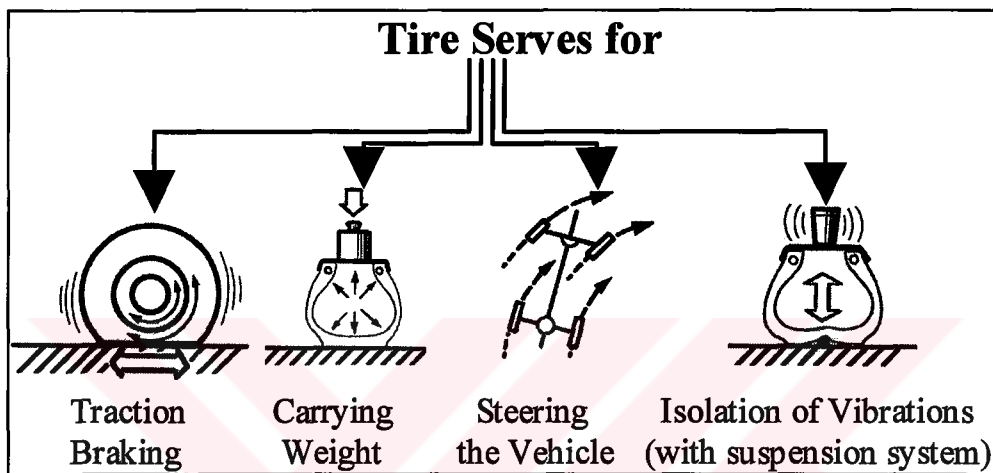


Figure 1.1 Basic Functions of Modern Tire

The obvious advantages of pneumatic tire enjoyed the popularity in cycle industry but the pneumatic tire had to wait the invention of detachable tires patented by C. K. Welsh, an Englishman and W. Bratt, an American in 1890. In 1895 a Frenchman, Edouard Michelin, produced the first practical pneumatic tire for use on motor vehicles (Michelin, 1997).

1.4 Modern Tire Types, Materials, and Nomenclature

Modern tires, although of distinct types, have many common properties. The three common primary components are the following. The carcass, composed of several layers of plies which are coated by a rubber compound to

maintain the internal air pressure. Bead wires (bundle), to which all the body plies are tied to and which fits the tire on the rim. The tread, which grips the road and is most wearing surface of the tire. The common nomenclature used for pneumatic tires is shown in Figure 1.2. In a tube type tire, the inflation pressure is contained within a tube placed inside the tire. In a tubeless tire, the inflation pressure is maintained by the tire itself having a sealing layer of rubber material and the rim. The advantages of tubeless tires are; they are lighter in weight compared to tube type tires, they have less heat generation and lower operating temperatures hence have longer lives and improved safety. In case of nail or similar objects penetrating the tire, in most cases the inflation pressure is not lost immediately, if the object separates from the tire during operation, inflation pressure decreases slowly. The tire installation is simple (Limpert, 1982).

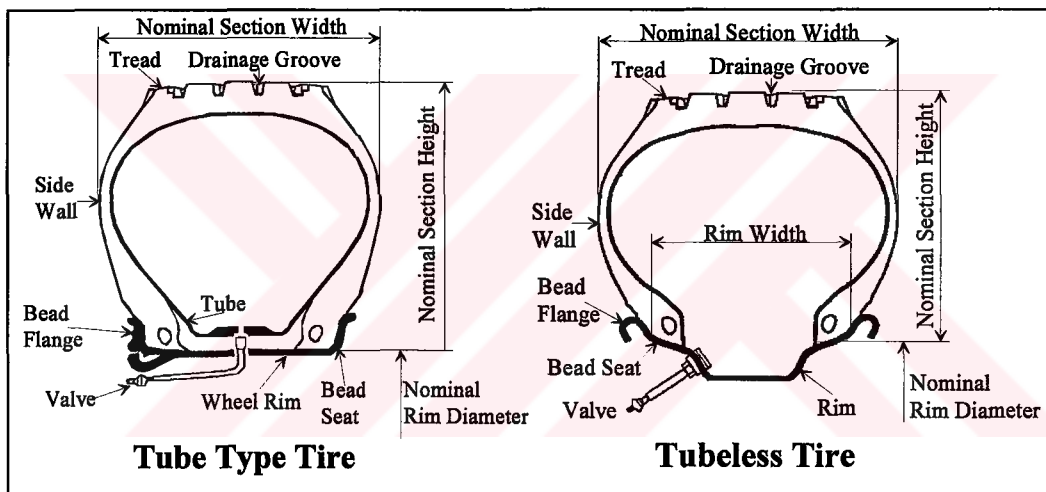


Figure 1.2 The Common Nomenclature used for Pneumatic Tires

Pneumatic tires may be classified as road vehicle tires and off-road vehicle tires. The off-road tires are designed to move a vehicle on deformable surfaces and the mechanics of such tires on soft soil (mostly termed as unprepared terrain) is known as terra mechanics (Wong, 1978). Off-road operation is out of the scope of this work.

The distinguishing factor among different types of road vehicle tires is the type of carcass construction. The two basic types of carcass construction are the cross (bias or diagonal in the USA) ply and the radial ply. These basic tire types are presented in Figure 1.3.

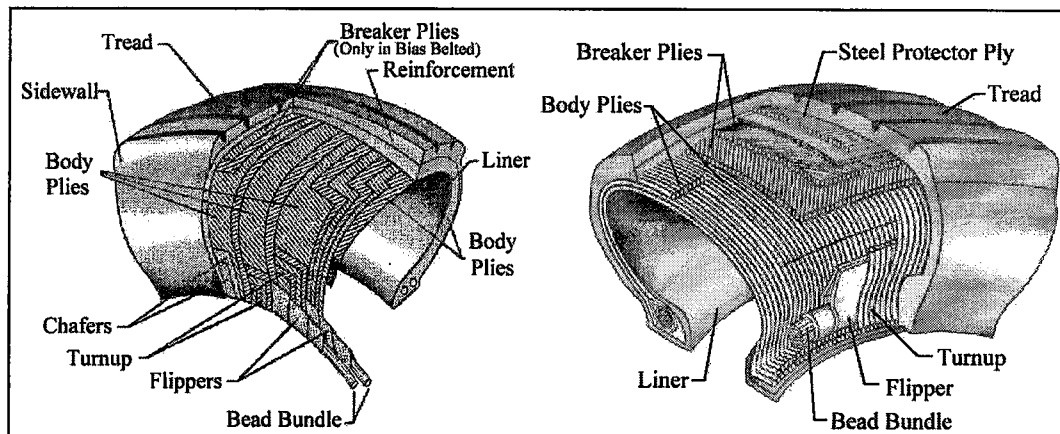


Figure 1.3 Two Basic Types of Tire Carcass Constructions, Cross Ply and Bias Belted (left) and Radial (right) Tires

In the very first pneumatic tires the carcass was made of rubberized cotton canvas. These tires had a life of 3000 to 4000 km. To eliminate this problem, unwoven fabric consisting of cords (treads) kept apart from each other by rubber was used. Soon after, it was discovered that the tire characteristics related to ride comfort and directional stability were contradicting and were dependent on the direction of cords. If the cords were in circumferential direction, the directional stability was good but ride was harsh. With the cords being perpendicular to circumferential direction, ride was soft but directional stability was almost lost. These facts resulted in the design of cross ply tires in 1920's. To obtain a compromise, the layers are placed at an angle of 45 degrees with the circumferential line of the tire with the adjacent layers in opposite bias. Requirements of softer ride and better directional control and stability led the development of radial ply tire. In this construction, the cords run from bead to bead across the circumferential line. Directional stability is assured by a number of belts called breakers beneath the tread. The crown works more independently

of the sidewalls when compared to cross ply tires. The first radial tire is Michelin X, patented on June 4, 1946 and produced in 1948 (Michelin, 1997). Radial tires besides the stated advantages, have longer lives and introduce lower rolling resistance to give improved fuel conservation. In the USA, the adoption of radial tires required a considerable expense to switch the production, so as a transition product, the bias belted tires were produced. Cross ply tires have greater interply friction than its radial counterpart which leads to significant structural stresses during tire flexing. This causes more heat build-up while working. Sometimes reinforcing plies are added to reduce the heat generation. Radial tires are about 20 % lighter in weight when compared to cross ply ones but they require higher inflation pressures. In radial tires, scrubbing (lateral sliding of tire on pavement) is less than cross ply ones (Davis, 1997).

Natural rubber, without any treatment, is not an adequate material for tire production, In 1839, Charles Goodyear accidentally mixed the heated rubber with sulfur, which he gave the name vulcanization after Vulcan, the Roman god of fire. Goodyear then set about refining the technique by applying different levels of heat for various lengths of time, and eventually found that steam applied under pressure for between four and six hours at about 132 degrees Celsius gave the best results. His discovery was patented in 1844 (Goodyear, 1996a). Tire tread material must provide a high coefficient of friction and must grip all kinds of road surfaces at any temperature possible, must be resistant to tearing and cutting, must bond with carcass material. To satisfy these requirements a compound of various synthetic rubbers together with additives is used. Carcass is made of rayon, polyester, nylon, glass fiber. The breaker cord material is rayon or fine steel wire. Steel belted radial tires offer better directional control and lower rolling resistance compared to textile belted radials but are about ten percent expensive.

Tread pattern is introduced to improve gripping particularly on surfaces covered with water, snow, mud or ice. A tire without tread would have a longer life but a small amount of water, snow, or mud would make a lubricating film thus causing no grip at all. The nomenclature of the tread is shown in Figure 1.4. Void ratio of the tire shows the ratio of grooves and sipes to the blocks. A high void ratio tire has more grooves to drain water and a low void ratio tire has more rubber in contact with the road. Grooves are used to drain foreign particles and fluids like dust and mud from contact patch. Sipes are small slit-like grooves which help drainage and allow the blocks to move more, to grip the road by additional biting edges. Blocks provide traction, braking and cornering forces. Dimples, the small indentations improve the cooling of the tread. Shoulder provides continuous contact with the road in maneuvers. Ribs create a circumferential contact band during rolling (Goodyear, 1996b). Some tread patterns for different road conditions are presented in Figure 1.5.

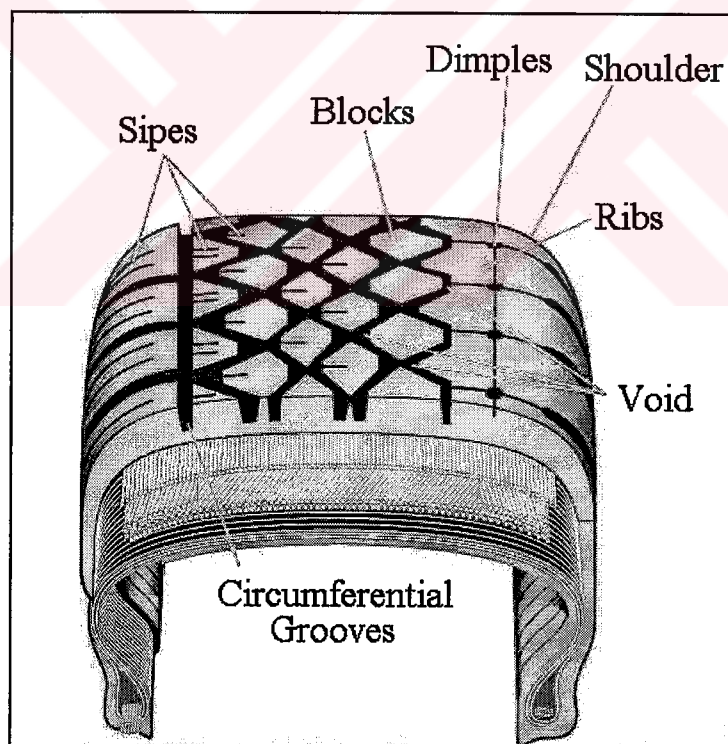


Figure 1.4 Tread Nomenclature

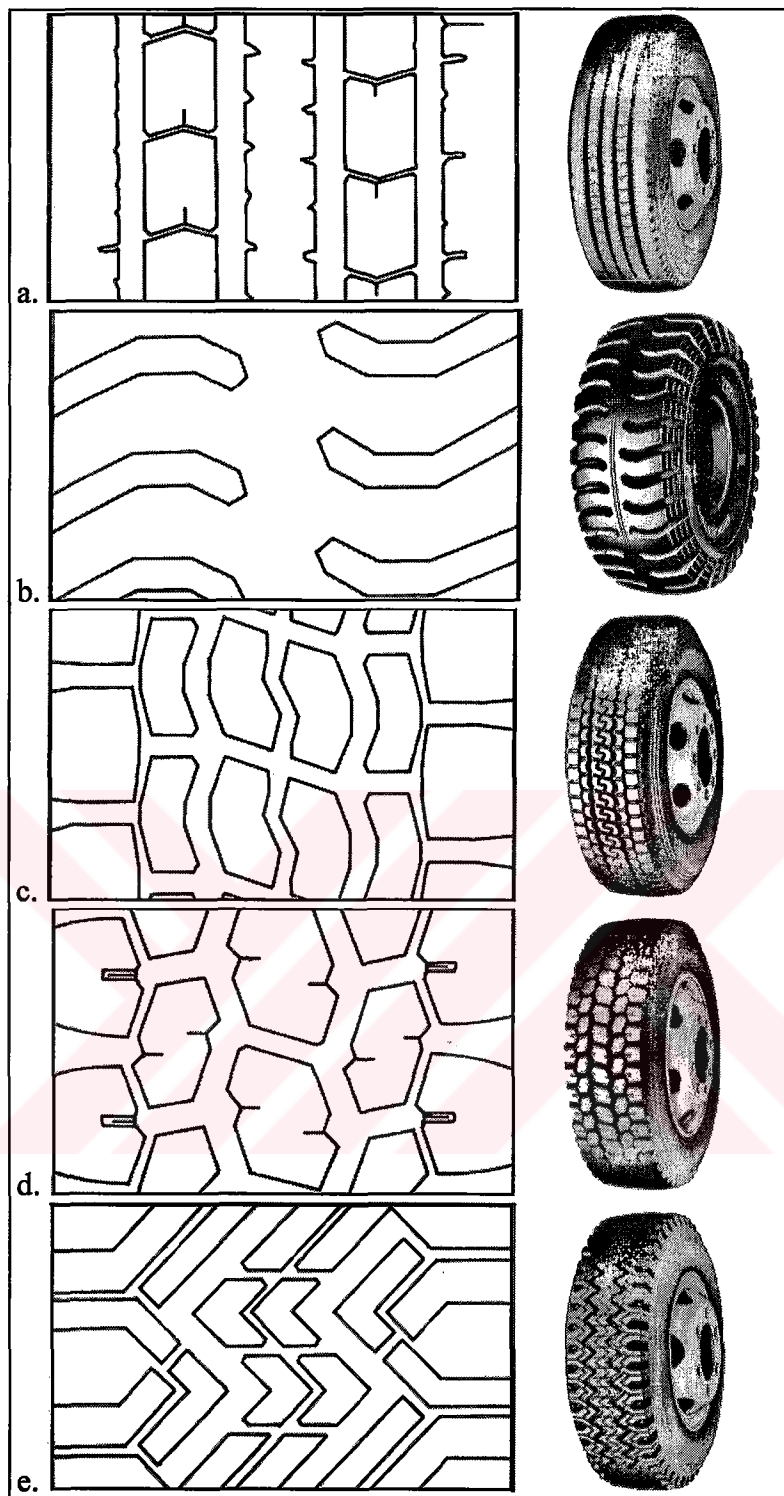


Figure 1.5 Some Different Tread Patterns

- a. Circumferential grooves for silent operation and better handling,
- b. Tread for high traction and braking performance especially in off-road operation,
- c. Circumferential grooves with teeth for handling and high traction performance,
- d. Block tread for better grip especially on mud and snow,
- e. Snow and mud tire

There are many tire designations, most of which are becoming obsolete. The two accepted designations are for automobiles and for commercial vehicles are shown on Figure 1.6 and on Figure 1.7 respectively. The load and speed ratings are tabulated in manufacturer's catalogs and are standardized.

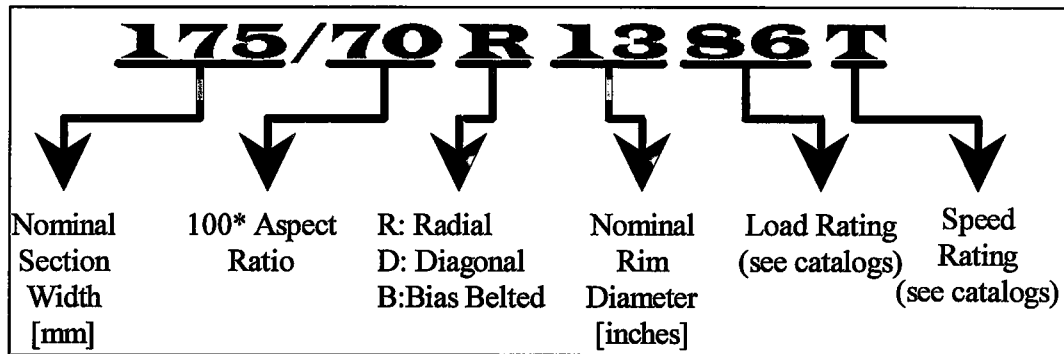


Figure 1.6 Automobile Tire Designation

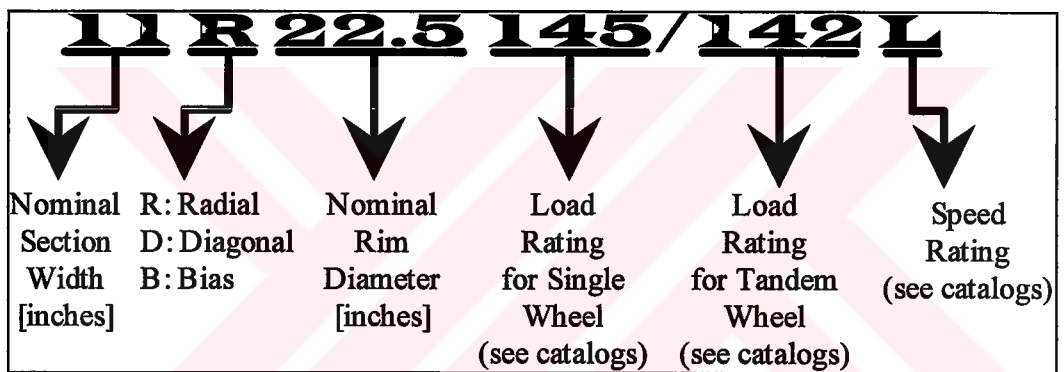


Figure 1.7 Commercial Vehicle Tire Designation

In the past, a tire's load carrying capacity was indicated by the number of plies it had. With the discovery of stronger materials, today, the ply rating is still an indication of load carrying capacity but it may not reflect the real number of plies in the tire.

1.5 Handling Behavior of Tires

In Section 1.2 it was stated that a tire had four functions, to support the vertical load of the vehicle, to develop tractive forces to propel and stop the

vehicle, to steer the vehicle, and to damp out the road irregularities. These former three duties are closely related to tire-road interaction problem which involves elastic deformation of the tire structure under a distributed load, frictional coupling between the tread and the road in the contact region. The deformation and contact problems are mutually interactive and frictional forces generated depend on the contact conditions. Tire structure being composite, anisotropic, having large deformations and rubber not being linear elastic, the problem is rather complex .

The three orthogonal forces; the vertical force, the tractive force and the cornering (lateral) force, are closely related. Variations in the vertical force is the prime concern of ride quality. Variations in the tractive force is closely related to vehicle performance (maximum acceleration and braking without skidding). Lateral (cornering) force, on the other hand, is related to directional control and stability of a vehicle, termed as handling.

Estimation of handling properties of tires is important since tires are the only media through which forces are applied to the vehicle to balance the forces of inertia and wind, dictating the handling behavior of a vehicle (Dugoff et al., 1970). Tire properties are also required in vehicle dynamics studies and simulations (Allen et al., 1990). The complexity of tire structure and behavior prevents the development of a complete and reasonable theory which may govern tire characteristics and performance. This complexity arises from symmetrical and anti-symmetrical aspects of the tire as well as its quasi-steady state behavior and vibratory state behavior (Maalej, et al., 1989).

The lateral force generated by a tire depends on the slip angle at which the tire is operating, among many other factors like inflation pressure, tire and road properties and the vertical tire load. Slip angle is the angle between the wheel heading direction and resultant direction of motion of the tire. In Figure 1.8, SAE

(Society of Automotive Engineers) tire coordinate axes and related terminology is shown. Nonzero slip angle occurs when a moving vehicle is steered away from the straight-ahead position. Due to inertia forces, the vehicle will tend to go straight on. In such a case, the tread in the contact patch will deflect laterally and this deflection will gradually increase from front of the contact patch to a point where elastic forces are equal to frictional forces, then the tread will slide back to its original position since frictional forces are not sufficient to deflect it any more. Figure 1.9 shows an exaggerated view of the contact patch to illustrate the so-called lateral wheel slip phenomena while Figure 1.10 shows the cornering (lateral) force characteristics of a typical passenger car tire at various vertical loads and slip angles while other operating conditions are kept fixed, in the form of a carpet plot (Krivetsky, 1958).

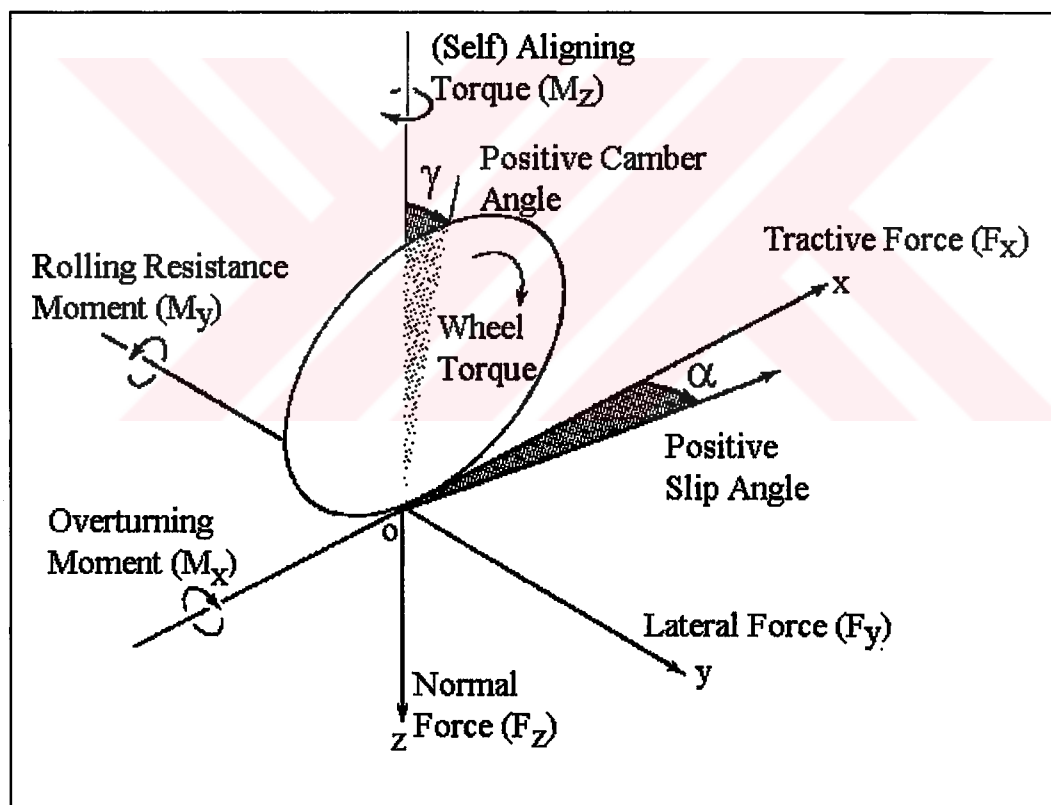


Figure 1.8 SAE Tire Coordinate Axes

Because of the increasing severity in the driving conditions, it has been necessary to improve, continually, the quality of pneumatic tires. During the growth of tire technology some understanding of the physics of tire behavior has also been developed. The origin of tire forces have been recognized but no general theory is available to explain, in a unified fashion, the response of tires to various combinations of circumstances.

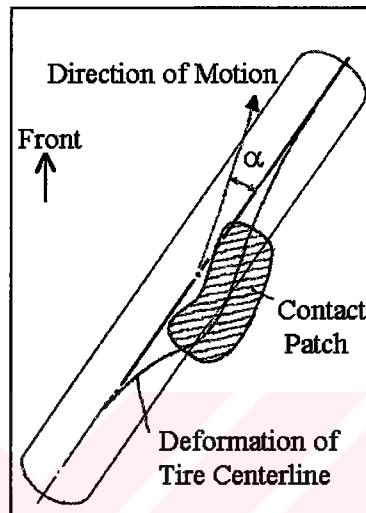


Figure 1.9 Lateral Wheel Slip Phenomena

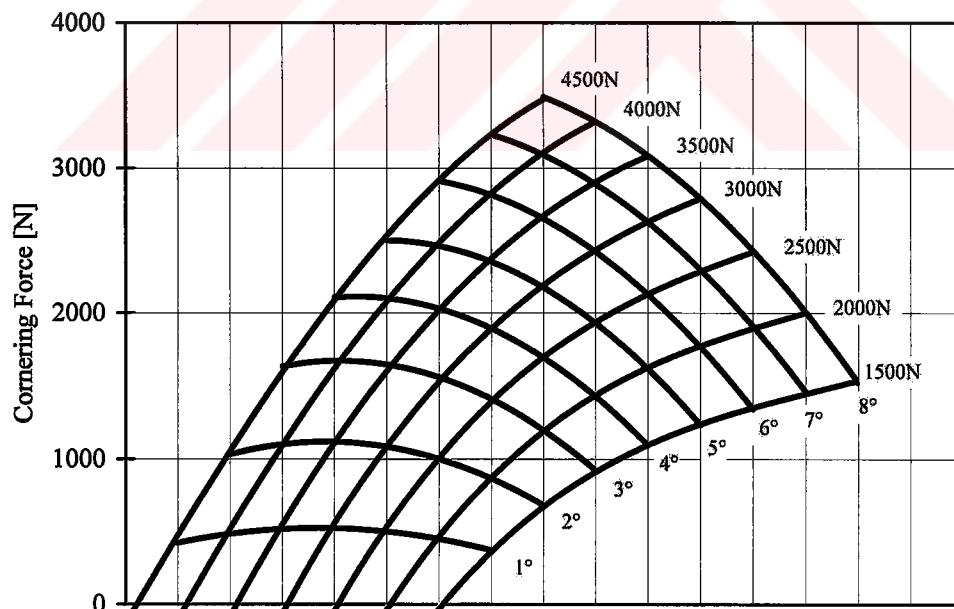


Figure 1.10 Cornering Force Characteristics of a Typical Passenger Car Tire

The designers, as well as the vehicle dynamics people, in order to see the dynamic behavior of pneumatic tires under different circumstances took two different paths. One path is examining the behavior of the tire under various operating conditions and recording the data, which is commonly referred as the experimental approach. To obtain accurate results, various test apparatus configurations have been devised which is discussed in detail in Chapter 2. The other path is modeling the tire mathematically. These models range from empirical formulae to evaluate various properties of tires under different operating conditions, to physical models which require extensive calculations or numerical solution methods like the finite element method. Mathematical models whether simple or complex requires experimental verifications for the range of validity. Mathematical models in literature are analyzed in detail in Chapter 2.

1.6 Need for a Tire Model

Pneumatic tire, being the only interface between a vehicle and ground, is one of the important components of a nonguided ground vehicle. A tire is designed, prototyped, tested, and finally presented for sale in the market. This whole procedure, especially producing prototype and testing, takes a long time, effort, and money. A model to predict the dynamic behavior of the pneumatic tire is invaluable as the time and the money spent on prototyping can be greatly reduced. Moreover, such tire models provide detailed stress distributions in critical sections of the tire where reliable measurements cannot be performed. The recent state of art in this subject is such that an experimental process on the prototypes to get the dynamic behavior of the tire is certainly necessary. However, test setups for this purpose are very complicated and costly. A realistic analysis on computer would be a great asset in the design and production of a new tire. Such an analysis would guide the tire designers or some expert system programs to observe the trends, thus develop better tires.

A detailed tire model considering many physical aspects of tire-road interaction is capable of simulating the cornering behavior of real tires in many different operating conditions precisely. Such a model is invaluable in both vehicle dynamic studies and in design and development of new pneumatic tires.



CHAPTER 2

LITERATURE SURVEY

2.1 Introduction

The tire models that have been used till today and found in literature may be divided into three broad classes as analytical, empirical, and physical tire models. Analytical tire models, in general, contain an oversimplified model of the physical phenomena. These models are mostly in the form of analytical equations of low order having closed form solutions, contain few parameters to be adjusted which have rather evident physical meanings. Analytical models yield results fastly, they are easy to use, and require no measurements once they are put into use for one type of tire; but due to their simplicity they cannot provide insight to the details of the essential effects of tire behavior. Empirical tire models are based on fitting a curve to the measured tire data. Some researchers attached physical meanings to the parameters of the curves, which are sometimes referred as semi-empirical tire models in literature. In some other cases, the meaning of the parameters are not so obvious. These models require a large amount of data to determine the parameters, analytical corrections and/or extrapolations are sometimes necessary. Although empirical models represent the tire response precisely and yields results in short times, to determine the parameters of the model even for a single type of tire, a large amount of experimental data is required. Therefore they are used to interpolate the behavior of a tire in between the data points obtained by experiments. Empirical models do not supply an insight to the details of tire dynamics either. In physical models, the physical

structure of the tire is considered with appropriate governing material laws, and boundary conditions so highly nonlinear system of equations are obtained. Depending on the purpose of the model, some simplifying assumptions may be used to shorten the solution procedure, which is nearly always numeric (especially advanced discretization techniques like finite element analysis are utilized). Physical models, although may include virtually any detail required, they are limited by computation time and computer resources. The more the included details are, the longer is the computation time. The analytical and empirical tire models find application in real time applications like driving simulators or in vehicle dynamics studies where tire is a component of a larger system, since they do not require long computation time and large computer resources. Physical and to a limited extend empirical models are used for scientific studies on tire dynamics and optimizing the dynamic behavior of tires (Nakajima, 1998).

In any modeling process, the response quantities obtained from the model have to be verified by known, reliable results before accepting the model output as representative of the physical system. In case of tire modeling, experimental verification is the only way to check the response since there is no universally accepted tire model that generates the universally accepted tire response.

In this Chapter, analytical, empirical, and physical models for predicting the cornering behavior of tires, found in literature, are examined. The results obtained by analytical and empirical tire models are benchmarked by experimental results. Tire cornering test machine types, their specific properties related to their construction geometries, and test machines found in literature are presented in the last section.

2.2 Analytical and Empirical Tire Models for Cornering Analysis and Their Verification by Experimental Data

Analytical tire models found in literature, together with the comments about these tire models are presented. The nomenclature in the equations in this section are identical with the original publications and therefore they may not be consistent with the notation used throughout this work.

2.2.1 Experimental Data Used

Although there exists many experimental tire cornering force data in literature, extreme care should be taken to select the data among them for benchmarking the tire models. Pottinger et al. (1976) examined the effect of test speed and testing surface curvature on cornering properties of tires and concluded that drum type tire testing machines, due to road surface curvature, yielded quite different results than road tests. They also concluded that too low road speeds affect test results as well but not as dominant as roadway curvature. Besides that, in order to supply some physical properties of the tire to the tire models, the geometric and material details of the test tire should be known. The test data fulfilling most of these requirements is the one taken from the Calspan Flat Surface Tire Testing Machine (Bird and Martin, 1973). Even if the tire is a cross ply tire (Goodyear, G78-15 with a design load of 1380 lbs at 24 psi inflation pressure) experimentally obtained cornering stiffnesses at various loads and inflation pressures, and cornering force characteristics are presented in great detail. The test speed is 10 mph (16 km/h) and tire is freely rolling (i.e. no tractive or braking torque).

Properties of the tire is presented in Table 2.1, cornering stiffness at various loads at 28 psi is presented in Table 2.2 and cornering force

characteristics at 28 psi inflation pressure (which is the most detailed cornering force data in Bird and Martin, 1973) is presented in Figure 2.1.

Table 2.1 Properties of the Experimental Tire

Tire	G78-15
Experiment Speed	10 mph (16 km/h)
Inflation Pressure	28 psi (193 kPa)
Section Width	7 inch (203 mm)
Inflated Diameter	27 1/8 inch (689 mm)

Table 2.2 Cornering Stiffness at 28 psi Inflation Pressure

Tire Load		Cornering Stiffness	
lbs	kN	lbs/deg	kN/rad
400	1.78	100	25.49
800	3.56	190	48.42
1200	5.34	215	54.80
1600	7.12	205	52.25
2000	8.90	185	47.15

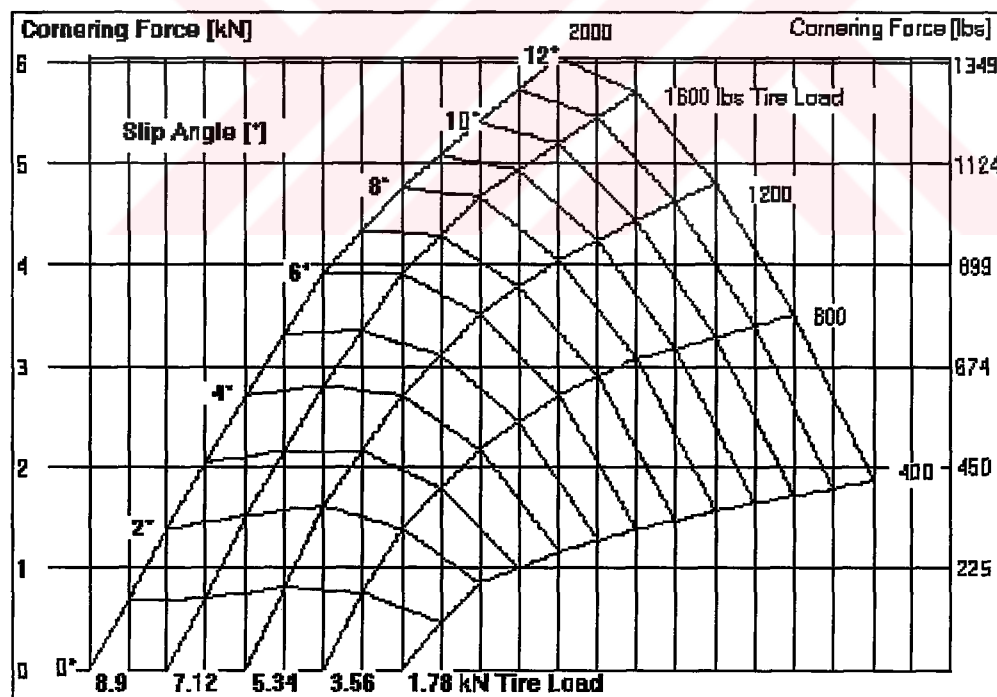


Figure 2.1 Experimental Cornering Force Characteristics of G78-15 Tire

To obtain the cornering force characteristics using the tire models presented here, a computer program using MicroSoft VisualBASIC 3.0 Professional is written. The carpet plots in this Chapter are obtained from the code mentioned.

2.2.2 Linear Spring Analogy

For small slip angles (up to 2° for light and up to 4° for moderate and heavy tire loads), cornering force may be approximated by a linear function of slip angle. The constant of proportionality being the cornering stiffness as

$$F_y = C_s \alpha \quad (2.1)$$

where C_s , termed as the cornering stiffness of the tire, is an indicator of cornering force generating capability of a tire. In general, cross ply tires have lower cornering stiffnesses than that of a radial tire of the similar type, therefore, operating at the same slip angle, a cross ply tire may generate lower cornering force than a radial tire, or on the same vehicle, performing the same maneuver a cross ply tire has larger slip angle to generate the same cornering force than a radial tire.

The cornering stiffness is formally defined as the derivative of the cornering force with respect to slip angle, evaluated at zero slip angle as

$$C_s = \left. \frac{\partial F_y}{\partial \alpha} \right|_{\alpha=0} \quad (2.2)$$

which appears nearly in all tire models presented. The deficiency of such linear model is that, when slip angle exceeds the indicated values, the cornering force generated by tire is less than predicted by the model. This phenomena is mostly termed as “saturation of cornering force at high slip angles”. At relatively higher slip angles, sliding dominates and cornering force becomes the product of coefficient of friction and vertical tire load which is the horizontal asymptote of the cornering force.

2.2.3 Model by Gim and Nikraves

The model by Gim and Nikraves (1990, 1991a, 1991b) starts with uncoupled tire behavior (i.e. cornering or longitudinal slip alone), extends to coupled behavior (i.e. longitudinal slip and cornering together) and has verification of the model proposed. The contact patch is assumed to be rectangular with contact pressure being constant along the tire width and having a parabolic distribution along the circumferential direction. The tread is assumed to deflect (i.e. adhere to the road) in the line of tire travel until the shear stress between a material point on the tire and ground is equal to elastic stress on the tread. After that point sliding starts. The assumed behavior of contact patch mid-line, which may be taken as the representative of the whole contact patch width, since constant pressure distribution along width is assumed, is shown on Figure 2.2 where P is the normal contact pressure at the contact patch. This model can use different friction models. The authors recommend either quadratic or linearly decreasing coefficient of friction with relative sliding velocity, adding that the linear model is fair enough for most of the regular terrains.

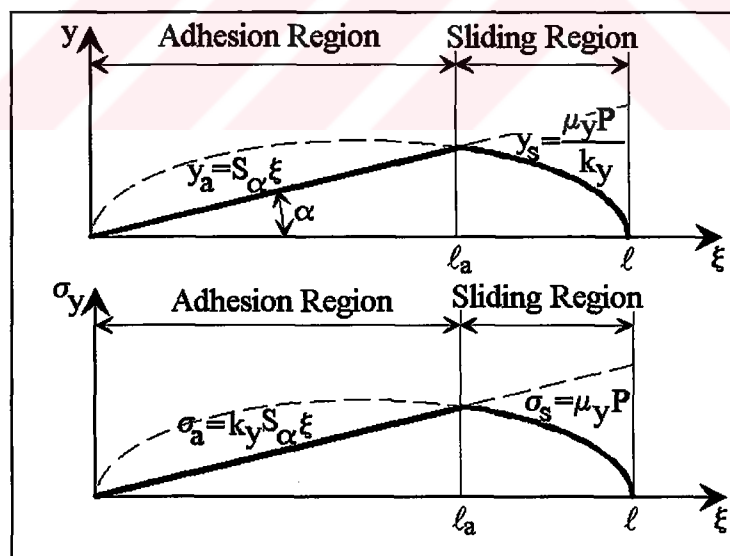


Figure 2.2 Lateral Deformation of Contact Patch and Lateral Stress due to Pure Slip Angle

For adhesion region, using linear elastic material approach, the shear stress at any point ξ away from the start of the contact patch is

$$\sigma_y^{(a)} = \frac{2C_\alpha S_\alpha}{w\ell^2} \xi \quad \text{for } 0 \leq \xi \leq \ell_a \quad (2.3)$$

$$k_y = \frac{2C_\alpha}{w\ell^2}$$

and for sliding region, the shear stress at any point ξ away from the start of the contact patch is

$$\sigma_y^{(s)} = \frac{6\mu_y F_z}{w\ell^2} \xi \left(1 - \frac{\xi}{\ell}\right) \quad \text{for } \ell_a \leq \xi \leq \ell \quad (2.4)$$

Cornering force is evaluated by integrating the above shear stresses in between the appropriate limits as

$$F_y = C_\alpha S_\alpha \left(1 - S_n + \frac{S_n^2}{3}\right) \quad (2.5)$$

or

$$F_y = 3\mu_y F_z S_n \left(1 - S_n + \frac{S_n^2}{3}\right) \quad (2.6)$$

where

$$S_\alpha = \begin{cases} |\tan(\alpha)| & \text{during braking} \\ |(1 - S_s)\tan(\alpha)| & \text{during traction} \end{cases} \quad (2.7)$$

and

$$S_n = \frac{C_\alpha S_\alpha}{3\mu_y F_z} \quad (2.8)$$

For sliding velocity dependent coefficient of friction

$$\mu = \mu_0 (1 - A_s S_\alpha - B_s S_\alpha^2) \quad (2.9)$$

or for regular terrains

$$\mu = \mu_0 (1 - A_s S_\alpha) \quad (2.10)$$

are used. The coefficients A_s and B_s in quadratic friction reduction model or A_s in linear friction reduction factor are obtained by curve fitting to experimental data.

The cornering force characteristics of G78-15 tire estimated by Gim and Nikravesh model is presented in Figure 2.3. When compared to experimental data, Gim and Nikravesh model yields slightly larger cornering forces for all vertical loads and slip angles.

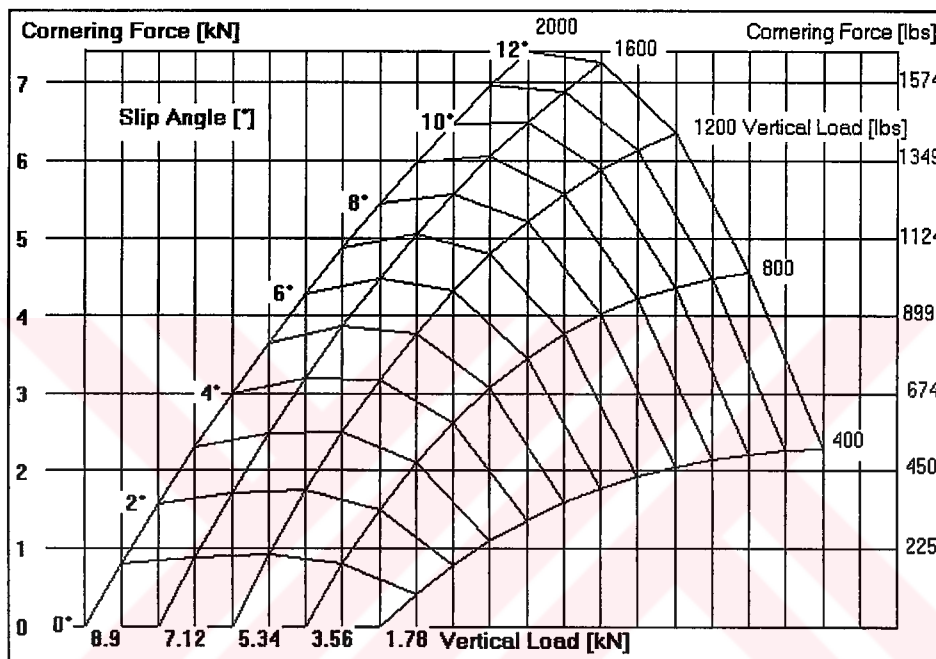


Figure 2.3 Cornering Force Characteristics of G78-15 Tire by Gim and Nikravesh Model

In this model the most important tire parameters are the load dependent cornering stiffness of the tire and coefficient of friction between the tire and the road. Cornering stiffness values presented in Table 2.2 are used and coefficient of friction is taken to be 0.85 (sliding coefficient of friction between tire and road) which is assumed to be independent from rolling velocity. Tire speed is taken to be 16 km/h without traction or braking.

Gim and Nikravesh model requires load dependent cornering stiffness values and coefficient of friction between the tire and the road precisely. This model is also capable of simulating the effect of traction and braking by supplying the longitudinal slip.

2.2.4 Model by Stribersky and Fancher

Stribersky and Fancher (1989), to model the nonlinear cornering behavior of heavy duty truck tires, used a simple, yet nonlinear tire model. Their model resembles the model by Gim and Nikravesh (1990, 1991a, 1991b) but the longitudinal pressure distribution at the contact patch is assumed to be elliptic. The coefficient of friction is assumed to be a function of radial load, and tire and road property, not a function of relative sliding velocity. Following the same procedure as in the model by Gim and Nikravesh, the lateral (cornering) force is

$$F_y = \frac{\mu F_z}{\pi} \left(\frac{2K \tan(\alpha)}{1 + K^2 \tan^2(\alpha)} + \arcsin \frac{2K \tan(\alpha)}{1 + K^2 \tan^2(\alpha)} \right) \quad (2.11)$$

where

$$K = \frac{\pi C_\alpha}{4\mu F_z} \quad (2.12)$$

and if lateral stiffness parameter k is known,

$$C_\alpha = \frac{w\ell^2 k}{2} \quad (2.13)$$

may be used to determine the cornering stiffness. Here w is width of the contact patch and ℓ is the length of the contact patch.

The model by Stribersky and Fancher requires only load dependent cornering stiffness and coefficient of friction between the tire and the road to model the tire. The cornering characteristics of G78-15 tire predicted by this model is presented in Figure 2.4.

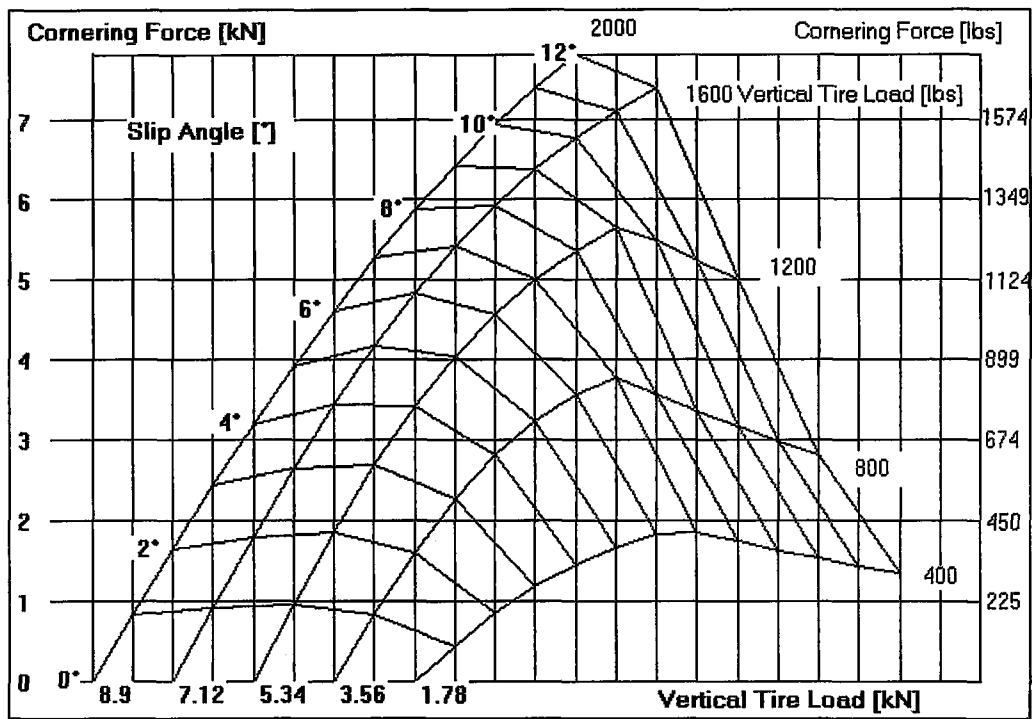


Figure 2.4 Cornering Force Characteristics of G78-15 Tire by Stribersky and Fancher Model

The load dependent cornering stiffness values of Table 2.2 and coefficient of adhesion, 1.3 is used in this model. For low slip angles the predicted cornering forces are higher than experimental for all loads whereas for high slip angles predicted cornering force is below the experimental value and for high loads it is above. The discrepancy implies that either the elliptic pressure distribution between this specific tire and road is imprecise or the tire data supplied to the model is inadequate to model the situation.

2.2.5 Model by Fancher and Bareket

Fancher and Bareket (1993) model uses the same physical facts as Gim and Nikraves (1990, 1991a, 1991b), and Stribersky and Fancher (1989) models. Constant pressure distribution along tire width and constant or trapezoidal pressure variation in circumferential direction of the contact patch assumption is the main difference. This assumption is mostly adequate for truck tires. Figure 2.5

shows the assumed pressure distribution with the nomenclature used by the authors where p_{\max} is evaluated such that the vertical force is balanced with the assumed pressure distribution. For heavy vehicle tires, p_{\max} is mostly very close to inflation pressure and for automobile tires, p_{\max} may be higher than inflation pressure.

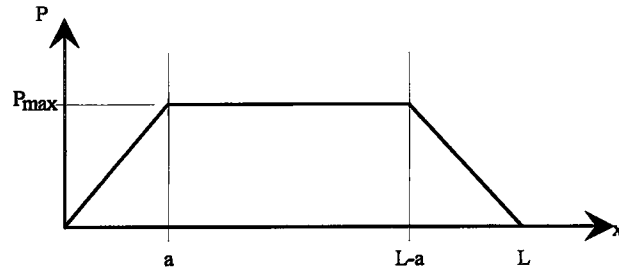


Figure 2.5 Pressure Distribution along the Contact Patch

Besides the general common points, coefficient of friction is modeled by a quadratic decreasing function with increasing total slip S_T as

$$\mu = \mu_0(1 - BS_T - CS_T^2) \quad (2.14)$$

where the coefficients B and C are found by curve fitting to experimental data.

The total slip S_T on the other hand, is defined as

$$S_T = \sqrt{S_x^2 + \tan^2(\alpha)} \quad (2.15)$$

In the calculations, the effect of traction and braking is introduced by θ which is the angle between the sliding direction and undeformed center line of the contact patch, defined as

$$\theta = \tan^{-1} \left[\frac{\tan(\alpha)}{S_x} \right] \quad (2.16)$$

defining λ as

$$\lambda = \sqrt{S_x^2 + \left(\frac{C_\alpha}{C_s} \tan(\alpha) \right)^2} \quad (2.17)$$

the generated cornering forces of the three zones will be as follows:

For $0 < x_s < a$ sliding occurs at all points with lateral force

$$F_{y1} = \mu|F_z|\sin(\theta) \quad (2.18)$$

For $a < x_s < L-a$ sliding occurs at

$$\frac{x_s}{L} = \frac{\mu F_z(1-S_x)}{2C_s\lambda \frac{a}{L}\left(1-\frac{a}{L}\right)} \quad (2.19)$$

with lateral force

$$F_{y2} = \frac{C_\alpha \tan(\alpha)}{1-S_x} \left(\frac{x_s}{L}\right)^2 + \frac{\mu|F_z|\sin(\theta)}{2\frac{a}{L}\left(1-\frac{a}{L}\right)} \left(1-\frac{x_s}{L}-\frac{a}{2L}\right) \quad (2.20)$$

For $L-a < x_s < L$ sliding occurs at

$$\frac{x_s}{L} = \frac{\mu F_z(1-S_x)}{\mu F_z(1-S_x) + 2C_s\lambda \frac{a}{L}\left(1-\frac{a}{L}\right)} \quad (2.21)$$

with lateral force

$$F_{y3} = \frac{C_\alpha \tan(\alpha)}{1-S_x} \left(\frac{x_s}{L}\right)^2 + \frac{\mu|F_z|\sin(\theta)}{2\frac{a}{L}\left(1-\frac{a}{L}\right)} \left(1-\frac{x_s}{L}\right)^2 \quad (2.22)$$

The cornering force generated by the tire is therefore

$$F_y = F_{y1} + F_{y2} + F_{y3} \quad (2.23)$$

The model presented by Fancher and Bareket is intended for modeling the heavy vehicle tire cornering behavior. As stated in some works (see Jenkins, 1982 for a detailed discussion on contact patch pressure distribution differences in heavy vehicle and automobile tires as well as new and worn out tires), the contact patch pressure distribution of heavy vehicle tires are much different than that of light vehicles such as automobiles. In heavy vehicles, pressure distribution is more uniform when compared to that of automobile tires. In order to simulate the non uniform behavior of automobile tires, a/L ratio is taken to be 0.45, which yields a rather triangular pressure distribution. For cornering stiffness, the load dependent values presented in Table 2.2 are used. For longitudinal stiffness, since no data is available a typical value of 30 kN/m, for coefficient of friction 0.85 is

used. The cornering characteristics predicted by the Fancher and Bareket model is presented in Figure 2.6.

When compared to experimental data in Figure 2.1, the model may predict precise results up to a slip angle of 6 degrees. In slip angles exceeding 6 degrees, the cornering forces predicted by the model exceed the actual values. It should be emphasized once more that this model is for modeling heavy vehicle tires and G78-15 being a passenger car tire, one cannot expect precise results with this model.

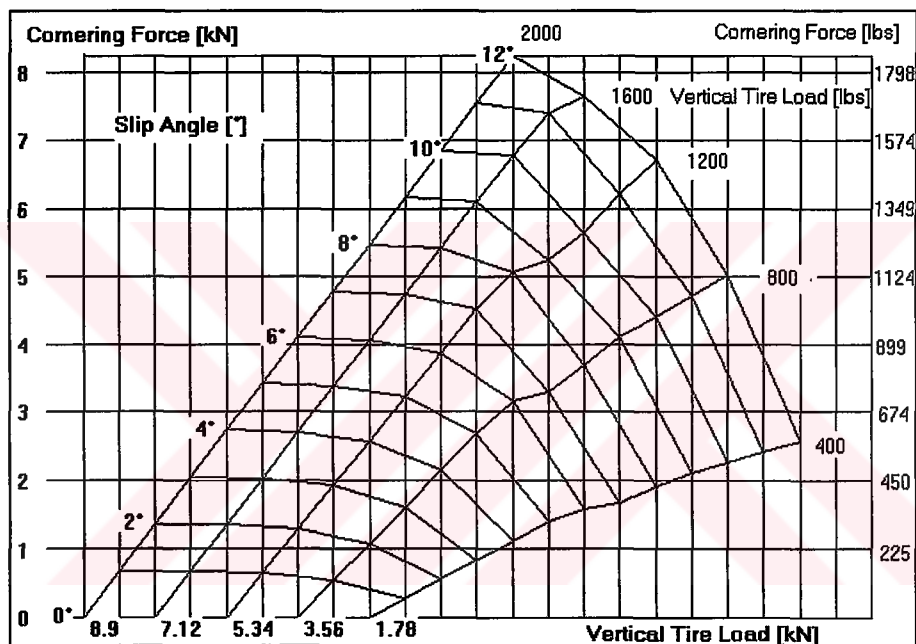


Figure 2.6 Cornering Force Characteristics of G78-15 Tire by Fancher and Bareket Model

2.2.6 Model by Dugoff

The model by Dugoff (Maalej, Guenther and Ellis, 1989) is one of the most common tire models used for vehicle dynamic simulations because of its simplicity and precise representation of tire cornering behavior even with traction or braking.

The cornering force generated is

$$F_y = \frac{C_y \tan(\alpha) f(\lambda)}{s-1} \quad (2.24)$$

where

$$f(\lambda) = \begin{cases} \lambda(2-\lambda) & \text{for } \lambda < 1 \\ 1 & \text{for } \lambda \geq 1 \end{cases} \quad (2.25)$$

and

$$\lambda = \frac{\mu F_z (1-s)}{\sqrt{(C_x s)^2 + (C_y \tan(\alpha))^2}} \quad (2.26)$$

Coefficient of friction is reduced with increasing rolling velocity as well as increasing longitudinal slip and slip angle as

$$\mu = \mu_0 \left(1 - eV \sqrt{s^2 + \tan^2(\alpha)}\right) \quad (2.27)$$

where, e is an empirical friction reduction factor.

For the G78-15 tire, the cornering force characteristics predicted by Dugoff model is presented in Figure 2.7

As can be seen by comparing Figure 2.7 by the experimental cornering force characteristics (Figure 2.1), only using a constant coefficient of friction as 0.85 and load dependent cornering stiffness values, Dugoff model predicted the cornering behavior quite accurately. Since the experimental tire rolls freely, longitudinal slip, s , is zero therefore longitudinal stiffness, the coefficient of longitudinal slip is of no importance. If the tire were braked or had traction, these effects could have been included in the model.

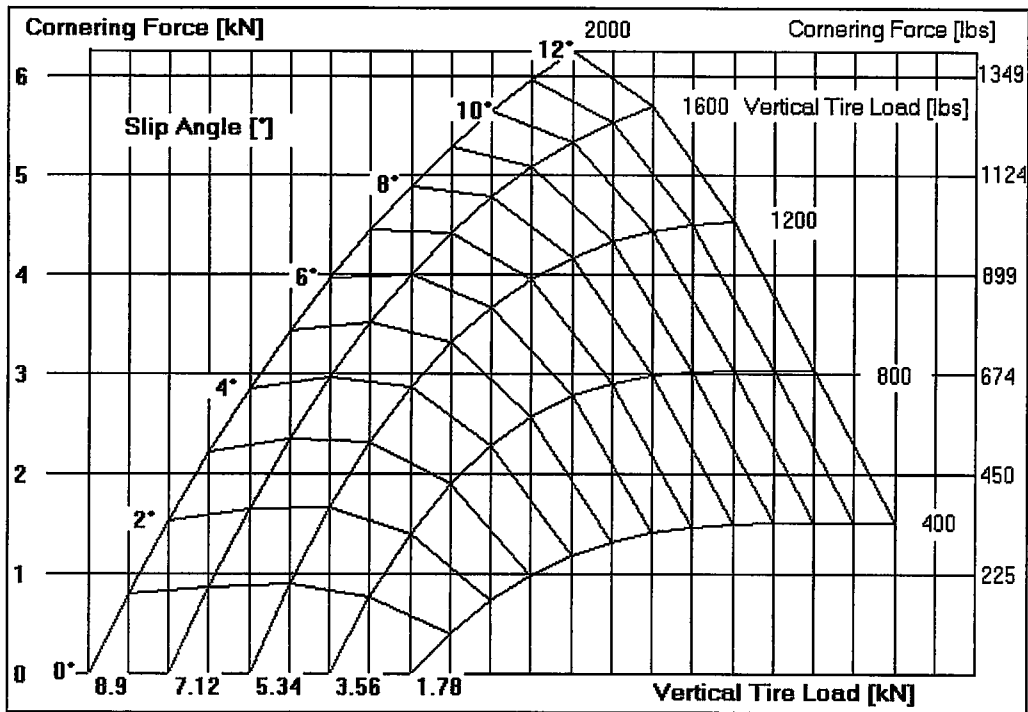


Figure 2.7 Cornering Force Characteristics of G78-15 Tire by Dugoff Model

2.2.7 Polynomial Tire Model

Polynomial tire model (Maalej, Guenther and Ellis, 1989) is one of the simplest curve fit procedures to the experimentally obtained tire cornering force data. The cubic fit is capable of producing the saturation behavior of cornering force at high slip angles. The model is in the following form:

$$F_y = C_0 + C_1\alpha + C_2\alpha|\alpha| + C_3\alpha^3 \quad (2.28)$$

The constants C_0 , C_1 , C_2 , C_3 are functional parameters of the vertical force defined as

$$C_i = A_{i0} + A_{i1}F_z + A_{i2}F_z^2 \quad i = 0, 1, 2, 3 \quad (2.29)$$

The coefficients may be determined by two curve fit procedures using least squares method. In this model, the coefficients have to be obtained for various camber angles, traction cases, inflation pressures and even velocities since the obtained coefficients consider only the effect of slip angle and vertical force variations.

For G78-15 tire, the four vertical load dependent coefficients are found using least squares method as presented in Table 2.3.

Using these coefficients, the cornering force characteristics of G78-15 tire is predicted as presented in Figure 2.8

Table 2.3 Polynomial Model Coefficients of G78-15 Tire

Load [kN]	C_0 [kN]	C_1 [kN/deg]	C_2 [kN/deg ²]	C_3 [kN/deg ³]
1.78	0.0293619	0.478081	-0.0555614	0.0023781
3.56	0.0181909	0.7987405	-0.0731533	0.0025747
5.34	-0.0167787	0.9253293	-0.0689396	0.0021084
7.12	-0.0319590	0.8265491	-0.029552	3.3278×10^{-5}
8.90	-0.0308690	0.7438598	-0.0123983	-0.0006178

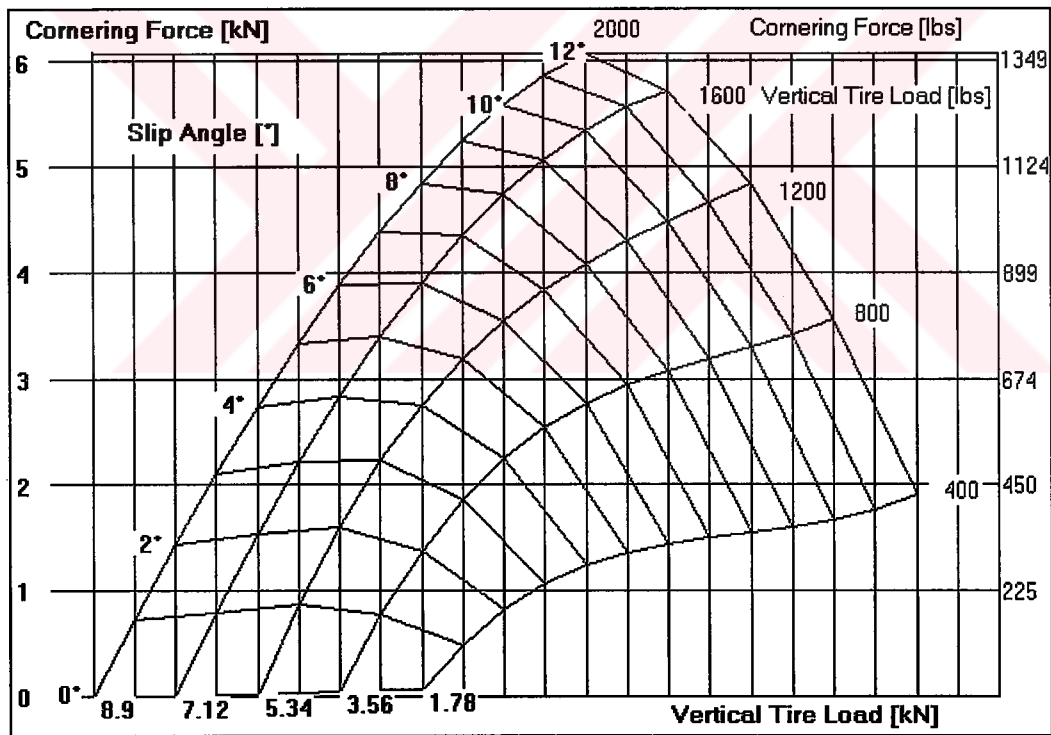


Figure 2.8 Cornering Force Characteristics of G78-15 Tire by Polynomial Model

A comparison of Figure 2.15 with the experimental data (Figure 2.1) reveals that polynomial tire model yields very precise results. Also for any load in between 1.78 and 8.90 kN, the coefficients may be interpolated as follows:

$$C_i = A_{i0} + A_{i1}F_z + A_{i2}F_z^2 \quad i = 0, 1, 2, 3 \quad (2.30)$$

The main drawback of polynomial tire model is that one requires excessive amount of experimental data to fit a curve.

2.2.8 Magic Formula Tire Model by Pacejka

Pacejka (Maalej, Guenther and Ellis, 1989, Pacejka, 1993) in various works, presented various versions of magic tire formula. The lateral force as well as longitudinal force and self aligning torque are approximated by sine functions which are in effect infinite series of polynomial approximations (Maalej et al., 1989). The lateral force as a function of slip angle is as follows

$$F_y = A_y \sin\left[B_y \arctan(C_y \theta_y)\right] + S_v \quad (2.31)$$

where

$$\theta_y = (1 - E_y)(\alpha - S_h) + \frac{E_y}{C_y} \arctan\left[C_y(\alpha - S_h)\right] \quad (2.32)$$

In the above equations A_y , B_y , C_y , E_y are the four coefficients depending on tire properties whereas S_h and S_v are the horizontal and vertical shift parameters. Pacejka attached some meanings to the four coefficients as; A_y representing the peak value of the side force, the product $A_y B_y C_y$ representing the cornering stiffness at zero slip and E_y influencing the curvature of the curve.

It is obvious that obtaining these coefficients for a particular tire is quite difficult since the equations involved are highly nonlinear. Convergence of the solution is another problem. Maalej et al. (1989) obtained the coefficients presented on Table 2.4 for a Firestone P195/70R14 tire with 26 psi inflation

pressure by using a commercial nonlinear regression analysis program with considerable CPU time. Figure 2.6 presents the cornering force characteristics of the same tire model.

Table 2.4 Coefficients of Pacejka Model for Firestone P195/70R14 Tire with 26 psi Inflation Pressure

F_z [lbs]	A_y [lbs]	B_y	C_y	E_y	S_h	S_v
462	-1009.72	0.36	0.31	-1.51	0	0
995	-2946	0.22	0.33	-0.5	0	0
1455	-3348	0.27	0.25	-1.23	0	0

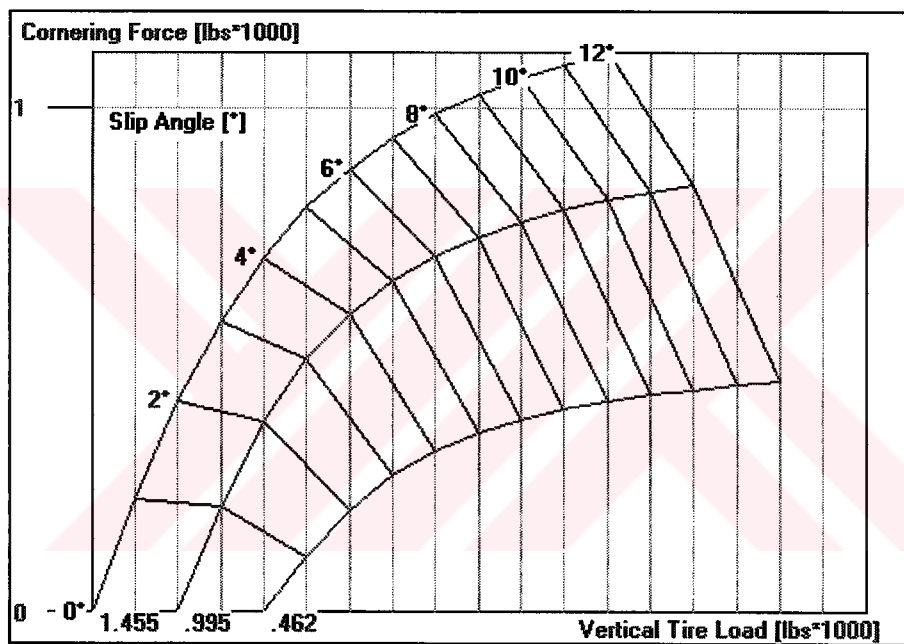


Figure 2.9 Cornering Force Characteristics of a Firestone P195/70R14 Tire by Pacejka Model

2.2.9 Model by Segel

The model proposed by Segel (Maalej, Guenther and Ellis, 1989) in 1972 was used for some vehicle dynamic simulations. The range of validity of the model is not verified experimentally. The cornering force is

$$F_y = g(\bar{s}_i) F_{y_{\max}} \quad (2.33)$$

where

$$g(\bar{s}_i) = \begin{cases} \bar{s}_i - \frac{1}{3}\bar{s}_i|\bar{s}_i| + \frac{1}{27}\bar{s}_i^3 & \text{for } \bar{s}_i < 3 \\ \frac{|\bar{s}_i|}{\bar{s}_i} & \text{for } \bar{s}_i \geq 3 \end{cases} \quad (2.34)$$

and

$$\bar{s}_i = \frac{[A_1 F_z (F_z - A_2) - A_0 A_2] \alpha}{A_2 \mu_y F_z} \quad (2.35)$$

$F_{y \max}$ is the upper bound of the cornering force, the three empirical constants A_0 , A_1 and A_2 are the coefficients of the quadratic curve, approximating the cornering stiffness given by

$$C_y = A_0 + A_1 F_z - \frac{A_1}{A_2} F_z^2 \quad (2.36)$$

In Segel model, the coefficients in the following equation

$$C_\alpha = A_0 + A_1 F_z - \frac{A_1}{A_2} F_z^2 \quad (2.37)$$

are found by least squares method. Using pound as the unit of force and degrees as the unit of angles, the coefficients are as presented in Table 2.5

Table 2.5 Segel Model Coefficients

A_0	-4.0
A_1	0.3195
A_2	2806

Using the coefficients presented in Table 2.5, the cornering force characteristics are obtained as shown in Figure 2.10.

As can be seen from Figure 2.10, Segel model yields good results. In order to use Segel model, the variation of cornering stiffness with respect to tire load is sufficient.

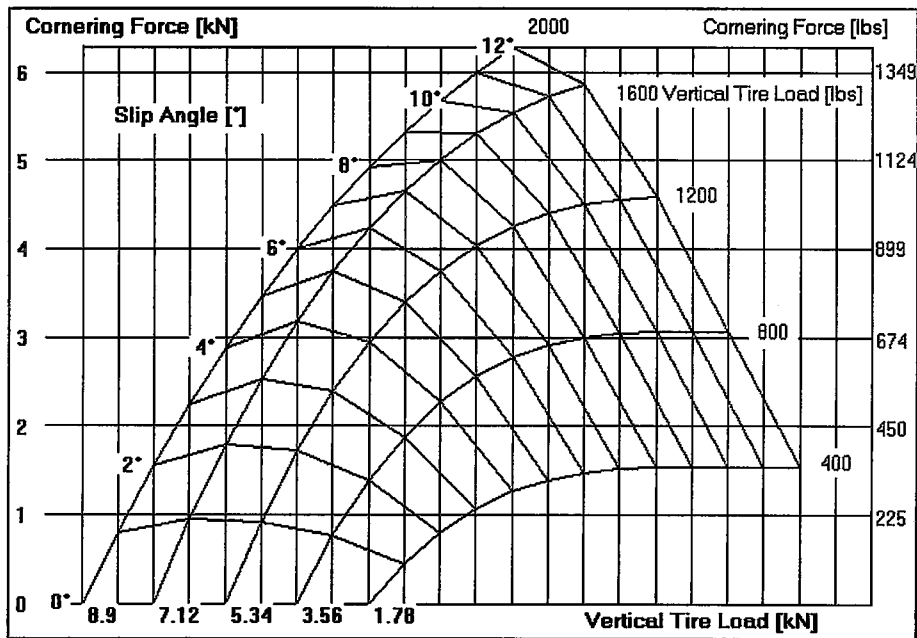


Figure 2.10 Cornering Force Characteristics of G78-15 Tire by Segel Model

2.2.10 Model by Allen

The model presented by Allen et al. (1987) is based on a saturation function in the form of ratio of two polynomials as

$$f(\sigma) = \frac{c_1\sigma^3 + c_2\sigma^2 + \frac{4}{\pi}\sigma}{c_1\sigma^3 + c_3\sigma^2 + c_4\sigma + 1} \quad (2.38)$$

The coefficients c_i are experimentally determined and only two groups of coefficients are proposed by the authors, one for bias ply tire and one for radial tires as presented in Table 2.6.

Table 2.6 Saturation Function Coefficients of Allen Model

Tire Type	c_1	c_2	c_3	c_4
Bias Ply	0.535	1.05	1.15	0.80
Radial	1.0	0.34	0.57	0.32

σ is the composite tire slip and is determined by the expression

$$\sigma = \frac{\pi a_p^2}{8\mu_0 F_z} \sqrt{K_s^2 \tan^2(\alpha) + K_c^2 \left(\frac{s}{1-s}\right)^2} \quad (2.39)$$

The cornering force is therefore

$$F_y = \mu F_z \frac{f(\sigma) K_s \tan(\alpha)}{\sqrt{K_s^2 \tan^2(\alpha) + K_c^2 s^2}} \quad (2.40)$$

Lateral stiffness coefficient is defined as

$$K_s = \frac{2}{a_{po}^2} \left(A_0 + A_1 F_z - \frac{A_1}{A_2} F_z^2 \right) \quad (2.41)$$

where the coefficients A_i for three different tires are experimentally obtained as presented in Table 2.4. The longitudinal stiffness coefficient is

$$K_c = \frac{2}{a_{po}} F_z (CS / FZ) \quad (2.42)$$

the ratio of cornering stiffness to lateral load (CS/FZ) is presented in Table 2.4.

Tire contact patch length is defined as

$$a_{po} = \frac{0.0768 \sqrt{F_z \cdot F_{zT}}}{T_w (T_p + 5)} \quad (2.43)$$

where F_{zT} is the tire design load at operating pressure (lbs), T_w is the tread width (in) and T_p is the tire inflation pressure (psi).

If required, peak (static) tire road coefficient of friction may be evaluated by

$$\mu_0 = \left(B_1 F_z + B_3 + B_4 F_z^2 \right) \frac{SN_0}{SN_T} \quad (2.44)$$

The coefficients B_i are presented in Table 2.7 and SN_T is the test skid number, having the value 85.

Table 2.7 Tire Parameters for Allen Model

Parameter	Standard Cross Section Radial	Bias Ply	Wide Section Low Profile Radial
Tire Designation	155 SR 13	P155/80 D13	P185/70 R13
Tire Width [in]	6	6	6
Tire Pressure [psi]	24	24	24
Tire Design Load [lbs]	810	900	980
A_0	914.02	817	1068
A_1	12.09	7.48	11.3
A_2	2028.24	2455	2442.73
A_3	1.19	1.857	0.31
A_4	-1019.2	3643	-1877
B_1	0.0003396	-0.000257	-0.000169
B_3	1.19	1.19	1.04
B_4	4.98×10^{-8}	2.64×10^{-8}	1.69×10^{-8}
CS/FZ	18.7	15.22	17.91

The saturation function coefficients of Allen model are supplied by the authors (Table 2.6). The A coefficients are the same as Segel Model, except this model uses radians as angle unit so A_0 and A_1 are multiplied by $180/\pi$. Using Allen model, the cornering force characteristics of G78-15 tire is found as presented in Figure 2.11.

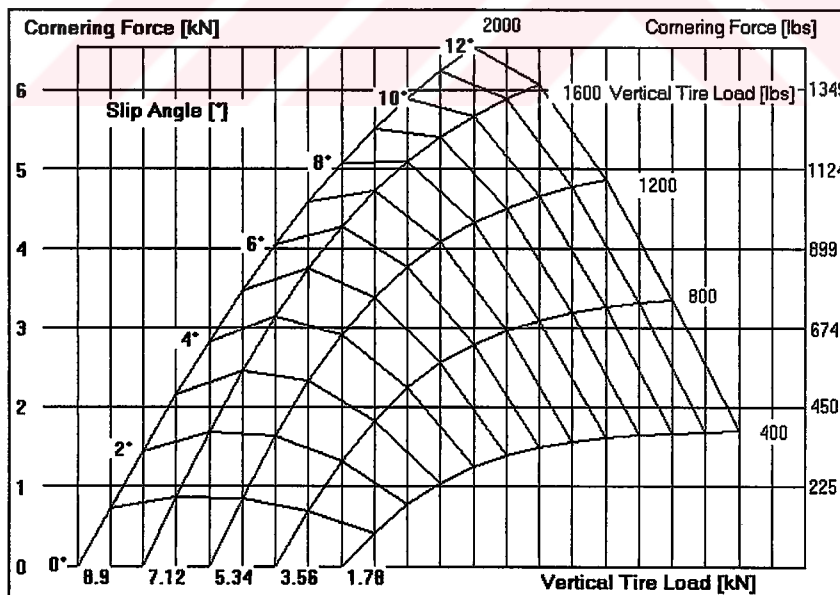


Figure 2.11 Cornering Force Characteristics of G78-15 Tire by Allen Model

Allen model, by using load dependent cornering stiffness, can model the cornering characteristics of the tire very precisely provided that adequate experimental data is supplied.

2.3 Physical Tire Models in Literature

Physical tire models obtained from the physical nature of the tire materials, using the governing laws. Physical models are the most comprehensive type of all tire models and are the hardest models to obtain solution due to the following facts.

The stress-strain relation of rubber deviates substantially from linear behavior, and shows a hardening behavior with increasing strain, which is harder to solve than softening behavior materials (Tekkaya, 1994) and viscoelastic behavior is dominant in time dependent problems.

Tire is not made of a single material but of many materials of different properties. Even composite material solutions are simpler than a tire composite solution due to:

- the differences in moduli between the reinforcing cords and the matrix is in the order of 1000 to 1 000 000 in tires whereas in a laminated fibrous composite it is often 10 to 20
- the cord used in tire is usually a collection of a large number of extremely small filaments which are twisted into a single reinforcing filament which has significantly different load deflection curves in tension and compression whereas most laminated fibrous composites have straight fibers
- distribution of cords in tires is not uniform in general, so smearing or averaging of properties has a limited utility.

Except inflation pressure, loads are not symmetric. Ground contact (contact patch) has dry friction in addition to contact. A rolling tire has centrifugal

force and impact loading as well. Thermal loads arise from manufacturing and operating conditions like unequal expansion and contraction of rubber and cord, nonuniform temperature due to working etc. (Noor and Tanner, 1985).

Although there are many difficulties concerned with physical tire models, the necessary tools to tackle with them at least one by one are available. What makes the problem difficult is that, the tire has all the above stated complications together. Still many researchers, having the necessary tools, made some simplifications depending on their purpose, on the model and obtained certain solutions. Although some models have oversimplifications, they form a base for a starting point to tackle the problem.

Kennedy and coworkers (1981) using triangular elements and rule of mixtures, linear elastic material model, including geometric nonlinearities, obtained axisymmetric tire model for inflation analysis. They validated their model by displacement and strain measurements on various positions on an experimental tire.

Huncler et al. (1983) developed a geometrically nonlinear shell finite element for tire vibration analysis. The element is axisymmetric, orthotropic, prestressed, doubly curved (curvature is introduced by an internal node not by radii of curvatures) and has cubic displacement functions.

Ridha et al. (1985) modeled the tire to be a homogeneous solid and with smooth tread. Authors aimed to model the contact between tire and road therefore they tried to omit the aspects of the tire which they believe to be of secondary importance. They model the nonlinear behavior by tangential stiffness matrix. Young's modulus for rubber was taken to be 26.2 MPa from a tensile test and Poisson's ratio was assumed to be 0.48 (i.e. nearly incompressible material behavior). The tire is first inflated to 24 psi (165 kPa) in four increments then the

rim is displaced by 1 inch (25.4 mm) in ten increments to obtain the desired loading. To determine the failure due to strain energy, strain energy densities are evaluated as well.

Rothert et al. (1985) loaded a homogeneous and grooveless tire axially, included contact and friction algorithms. They modeled the nonlinear material behavior by the following relation

$$(2.45)$$

where ϵ_{\max} is the maximum principal strain. Initial Young's modulus (E_0) is taken to be 5.78 MPa, α_E is 3.364, Poisson's ratio is 0.324, the static coefficient of friction 1.0 and dynamic coefficient of friction 0.8 between tire and road.

Padovan and Paramadilok (1985), recognizing the total Lagrangian formulation being cumbersome, proposed a modified Hughes type contact strategy using moving total Lagrangian coordinates which has the observer on the non-rotating axle. They modeled the tire as a ring on elastic foundation since they found a full three dimensional analysis computationally very expensive.

Richards et al. (1986) examined the effect of boundary conditions on tire rim and contact patch on the vibratory modes of the tire. They use 234 nodes, 1404 degrees of freedom (6 degrees of freedom per node) and 216 shell elements with equivalent structural properties to the composite shell behavior. They included the mass and inertia, lumped at the wheel center. They imposed various boundary conditions to the axle and contact patch, obtained the natural modes of the tire, verified by experiments.

Faria et al. (1992) included the viscoelastic material behavior by an internal state variable tensor. The friction between tire and road is modeled by regularized Coulomb law. An algorithm is proposed to specify the hub load instead of hub deflection, to formulate the problem in a more natural way. A

constitutive perfect gas equation is introduced to account for changes in inflation pressure (it was seen that pressure change due to deformation is negligibly small but in further models, the authors plan to include thermal effects as well, which, they suppose would cause considerable changes in inflation pressure). They used three types of isoparametric finite elements, 20-node brick, 8-node multilayer shell and 16-node multilayer thick shell elements. They introduced a formulation for steady solution.

Du et al. (1998) modeled rolling loss and temperature field due to rolling loss of steady rolling tires by nonlinear finite elements. Seifert et. al. (1998) modeled the global wear using finite element method, Turner and coworkers (1998) and Snyman (1998) modeled steady state rolling behavior of tires by finite element technique.

Noor and Tanner (1985) in their extensive work about tire models, classify the physical tire models into six categories. The six models and their properties are briefly explained below.

i) Early Tire Models: The tread is considered to be a prestressed string or ring with bending stiffness, and sidewalls as elastic or viscoelastic foundations. This type of models require excessive experimental data to determine the equivalent properties. Accuracy and range of validity of these models are not known in advance.

ii) Cord Network Models (Netting Analysis): The inflation pressure is assumed to be carried by cords. These models neglect bending of tire and stiffening effect of rubber matrix surrounding cords.

iii) Membrane Models: They use linear or nonlinear momentless theory of shells. Bending on shell deformations are neglected. Although these models are

useful in evaluating the tire inner tube behavior, they cannot handle discontinuities in loading, geometry, or material properties.

iv) Two Dimensional Axisymmetric Models: These models, as the name implies, are limited to axisymmetric loading, used to study tire response to cord shrink forces and inflation pressure.

v) Three Dimensional Continuum Models: There exists two approaches:

1. Semi-analytic Techniques: They are used to reduce the dimensionality of the problem.

2. Three Dimensional Isoparametric Elements: They are used to model various properties of tires.

vi) Two Dimensional Thin and Thick Shell Elements: Thin shell models reduce the dimensionality of the problem therefore are simpler, but since these models use Kirchoff-Love shell theories which neglect transverse shear deformations, their use is questionable. Thick shell models may be used with care. Also including anisotropy due to reinforcement enlarges the model.

There exist some other models which are included neither in the classification of this thesis nor by the six types examined by Noor and Tanner, in literature. One of these models is the traction and handling behavior of tires on deformable surfaces. Crolla and El-Razaz (1987) presented such tire models found in literature and proposed their own model. Due to complexity of the deformable surface and due to simplicity requirements for vehicle dynamics simulations, the models contain empirical constants and are explicit except that of Crolla and El-Razaz's. Karafiath (1986) extended the model of straight traveling tire on deformable surface to steered tires. Balkin et al. (1997) in his extensive work about tire modeling efforts in various countries with a special focus on

Soviet research, mentions more elaborate cord network models solved by finite difference method by Soviet researchers.

2.4 Specifications of a *Perfect* Tire Model

There exists many tire models in open literature, each is for a specific purpose, having its own advantages and disadvantages. Analytic tire models are oversimplified models of actual tire. Under standard operating conditions, depending on the precision of experimental properties supplied, may yield precise results with little effort. Empirical tire models require more experimental data, and again depending on precision of experimental data they can yield precise results as well. Empirical tire models may even model nonstandard operating conditions, if data about such conditions exist. Physical models on the other hand have a quite different nature. These models are intended to understand the tire-road interaction, the detailed dynamic behavior of tires like wear, temperature build-up when running, noise generation, local surface tractions at the contact patch and the like. In performing such a detailed analysis cornering force characteristics is mostly obtained as either one of the outputs or as a byproduct. Physical models mostly require the geometric and material data with operating conditions only. Since they do not require experimental data, they are also widely used in design process of a tire. The problem with the physical tire models is that they require rather long time to prepare the model and long computational time on computer.

With the above discussion, a *perfect* tire model, if it exists, should bear the following properties:

The input data to the model should contain only the physical properties of the tire such as its geometry, material constants etc., and the running conditions of the tire. It should not contain any experimental data about the tire itself.

The model should precisely describe the dynamic behavior of the tire. It should not contain oversimplifications or global approximations.

The computational effort to solve the problem should be not be excessive.

Unfortunately such a perfect tire model is not available yet, so depending on the needs, one should either use analytic or empirical tire models, containing oversimplifications and requiring experimental data about tire or physical tire model requiring long computation time on computer. In this thesis, although analytic and empirical tire models are examined, the aim is to determine the cornering behavior of tires with as few experimental data as possible and to make as little oversimplifications as possible unless none is possible. Therefore a physical tire model will be constructed and the cornering behavior of the tire will be obtained from this model.

2.5 Need for Model Verification

As in any modeling effort, the behavior of tire model under various operating conditions must be verified using an experimental scheme. Besides verification, experiments provide tuning a complex model to its physical counterpart, if the phenomena is not modeled completely.

Tire, having a rather complex geometry with thread, reinforcements, viscoelastic material behavior, large deformations, inflation pressure, contact with ground, cannot be expected to be modeled completely. Even material constants of rubber are very different in various references and it is believed to be different depending on the properties of a specific rubber, its age, storage conditions (time history) and ambient temperature. To determine the uncertainties in such cases

and their effect on dynamic properties of tires, one cannot avoid experimental verification.

2.6 Tire Testing Devices Found in Literature

In tire testing some parameters are controlled and the handling properties are measured at these known parameters, namely the operating conditions. Depending on the specific test procedure, the controlled parameters are the tire (radial) load, slip angle (or steering angle), camber (inclination) angle, tire inflation pressure, driving/braking torque, speed of the test tire and roadway, variation in the roadway characteristics including different road surfaces, hydroplaning, snow and ice.

The most important handling properties are the lateral force, which determines the directional stability of the vehicle and the self-aligning torque, which is a function of the lateral force and pneumatic trail of the tire. There are some derived properties which are used as benchmarks of tire handling performance such as cornering stiffness, cornering coefficient, camber stiffness, lateral coefficient of friction. In tests with powered tire it may be necessary to determine the percent wheel slip as well. For vehicle dynamic simulations, the above stated static response quantities may not suffice and it may be necessary to determine the dynamic response of cornering force to some predetermined dynamic slip angle (Weber and Persch, 1976) or the relaxation length (Loeb et al., 1990).

In a test, mostly the three mutually orthogonal forces and moments on tire axle are measured using various types of transducers. In some tests it may be important to monitor the instantaneous tire inflation pressure, effective tire rolling radius, roadway, and rolling speeds.

Laboratory tire testing devices for force and moment characteristics of tires simulate the operating conditions of the tires in the laboratory. The main advantage of laboratory testing devices is that, they have more controlled testing conditions when compared to the devices performing the tests on road. The main disadvantage is that they cannot simulate the actual driving conditions precisely due to the facts explained in detail below.

In nearly all types of tire testing machines there exists a large amount of common features. These are the test tire which may be loaded to a desired test value, with desired inflation pressure and may be powered or free rolling. Some transducers measure the forces and moments generated on the test tire. The main distinguishing factor in laboratory tire testing devices is the shape of the roadway. In some instances, there exist accessories to emulate different roadway conditions such as water sprays for hydroplaning and different coatings on the roadway surface to emulate different construction materials.

2.6.1 Flat Bed Tire Testing Machines

The test surface in a flat bed testing machine is a traveling table. Due to limited stroke of the table, the test speed is kept low compared to actual operating speed of a tire, and steady state operating conditions may not be reached. This type of machine is very useful in determining the elastic properties of tires. Figure 2.12 shows the schematic representation of a flat bed tire testing machine.

General Motors Research Tire Test Machine (Nordeen, 1964) is a flat bed tire test machine which supports the tire within an assembly of three frames. The outer frame performs slip angle adjustment, the middle frame performs camber angle adjustment and the inner one performs tire loading (by vertical movement). The machine is constructed such that the center of tire contact remains fixed independent of tire deflection, camber or slip angle. Force measurements are

performed by strain gages. The table which emulates the roadway is 10 ft (3.05 m) long and may be propelled at a speed of 1 mph (1.6 km/h) in any of the fore or aft direction. The table has a temperature control between 0 and 130°F (-17.8 and 54.5°C) and it may be wetted, flooded or frozen for different road conditions as well as different surface material may be stuck on it.

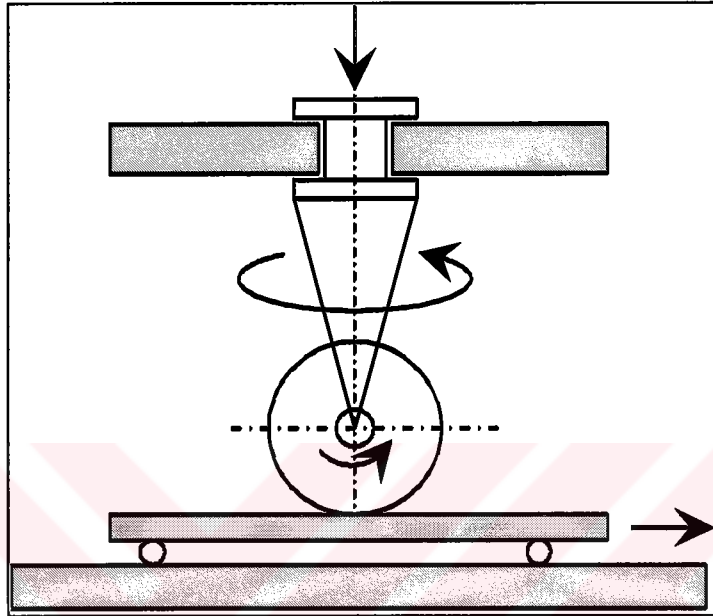


Figure 2.12 Flat Bed Tire Testing Machine

B. F. Goodrich flat-bed tire testing equipment (Pottinger, 1976) is derived from General Motors device and "Flat-Plank" tester designed and constructed by Dunlop. It is capable of measuring each of the six force and moment components under precisely controlled conditions. This machine is identical to Highway Safety Research Institute testing machine except B. F. Goodrich machine is structurally stronger.

2.6.2 Flat Surface Tire Testing Machines

In flat surface testing machines the limited table stroke problem in flat bed testing device is eliminated. Flat surface testing machines, like the flat bed testing

machines can simulate the roadway conditions precisely when compared to curved surface tire testing machines which will be explained in the following sections. The contact patch and the pressure distribution in the contact patch are more realistic when compared to curved surface tire testing machines. In return, these machines have very complex roadway constructions. Figure 2.13 shows the schematic representation of a flat surface testing machine.

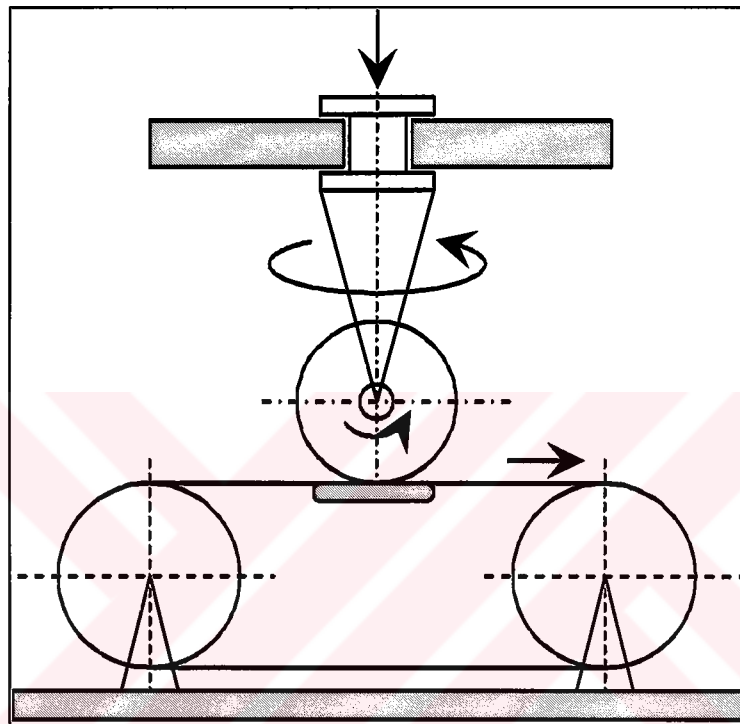


Figure 2.13 Flat Surface Tire Testing Machine

The two different types of flat surface tire testing machines found in the literature are The Tire Research Facility (TIRF) by Calspan (Bird, 1973) and The Flat-Trac machines model I (Langer, 1980) and model II (Stocker, 1991) by MTS Systems Corporation.

The TIRF machine has an upper frame in the form of a bridge housing the tire positioning system and the roadway watering system. The tire and the roadway are powered by hydraulic motors. Roadway is a stainless steel belt

covered with desired road construction material and is supported by air bearings against tire load. The test tire is positioned to desired slip and inclination (camber) angle and normal load is applied by a closed loop servo hydraulic system. The forces and moments are measured by strain gages which have small deflections (i.e. deflections do not spoil positioning) yet producing sensible signals. Temperature compensation of strain gages are performed by standard methods. Measured forces and moments are transformed into SAE coordinates. The machine has a watering system for wet surface tests and hydroplaning. The raw data is stored in magnetic disks, reduced and corrected if needed by a computer, presented as carpet plots. At some instances, equations are solved by the computer.

Flat-Trac test machines have very stiff machine frame to deflections as well as rotations in all axes. The frame is different from other constructions and is A-shaped. The radial position, slip angle and camber angle axes are not coupled so adjusting one does not affect the adjustment of other. The belt tracking system is constructed such that belt deflections are kept very small not to affect the measurements. One of the belt drums is powered in radial direction in order to adjust belt tension to minimize belt deflections. The belt is supported against radial loading of the tire by a bearing made of plastic material, hydrodynamically lubricated and cooled by water. In model I the control system of the machine has three parts, the analog control system, the operator's control system and the data reduction and acquisition system. The machine measures test data in machine coordinate system, then converts it into SAE tire coordinate system. The data is averaged for each tire revolution then displayed. The output may be obtained as in the form of a carpet plot or tabulated depending on the request. The load transducers are serially connected, each measuring one component of the force vector. Each sensor operates as a flexural four-bar linkage sensitive only in one direction.

The Flat-Trac Model II test machine is developed because the requirements for tire testing exceeded the capabilities of Model I stated above. Model II, although resembles Model I, has extended features. The major improvement over Model I is that Model II is capable of performing tire tests under dynamically changing conditions. The force transducers used in Model I are replaced by a one piece very stiff force and moment transducer with no measurable hysteresis under extreme loading conditions. Due to the stated properties of the transducer, tire uniformity measurement at high speeds is possible.

The major tire tests performed on Flat-Trac Model II are the residual pull test which determines the residual aligning torque and lateral force on a free rolling tire at various slip angles, tire loads, inflation pressures in both forward and reverse directions. In tire traction tests, tire traction properties as the tire is ramped to a specified positive or negative slip ratio with inflation pressure, load, belt speed, inclination (camber) angle and slip angle held constant during each ramp. The slip angle frequency response test is a dynamic free rolling test for measuring the force and moment response of a tire to a cycling slip angle at various frequencies. The slip angle sweep test is a free rolling test for collecting transient data for dynamic simulation of severe vehicle handling behaviors.

2.6.3 Drum Type Tire Testing Machines

a) External Drum Tire Testing Machines

The complexity of roadway construction in flat surface tire testing machine is eliminated by using an external drum but due to convex curvature in the roadway, the contact patch of the test tire is smaller than that of a tire operating on a straight road and the contact patch pressure distribution is different

than that of a tire on a straight road. This requires correction on the obtained data for obtaining straight road characteristics. The correction may be a complex function of many testing parameters. Some authors (Pottinger, 1976) even claim that a point by point correlation is required to obtain the flat surface cornering characteristics from a curved test machine results which is practically not possible. The common practice is either comparing different tires with a test tire or estimating flat surface cornering properties of the test tire by using simple corrections. Figure 2.14 shows schematic representation of an external drum tire testing machine. Delft University (Zegelaar and Pacejka, 1996) and Mercedes Benz A. G. (Liester, 1997) have external drum tire testing machines whose specifications are not known in detail.

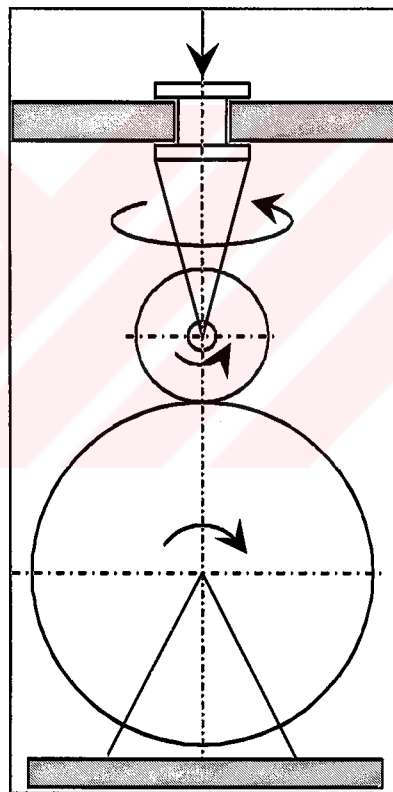


Figure 2.14 External Drum Tire Testing Machine

b) Internal Drum Tire Testing Machines

Internal drum test machines are similar to the external drum tire testing machines, except the roadway surface is concave and the tire runs on internal surface of a drum. In literature there exists a comparative measurement with internal drum test machine and roadway tests (Bergman et al, 1971). The authors claim that they could not obtain similar conditions on test machine and on road so they use some kind of data normalization to compare the test results. The authors claim that excellent correlation exists between normalized road test results and normalized laboratory test results so it is necessary to use normalization techniques in data processing. Figure 2.15 shows a schematic representation of an internal drum tire testing machine.

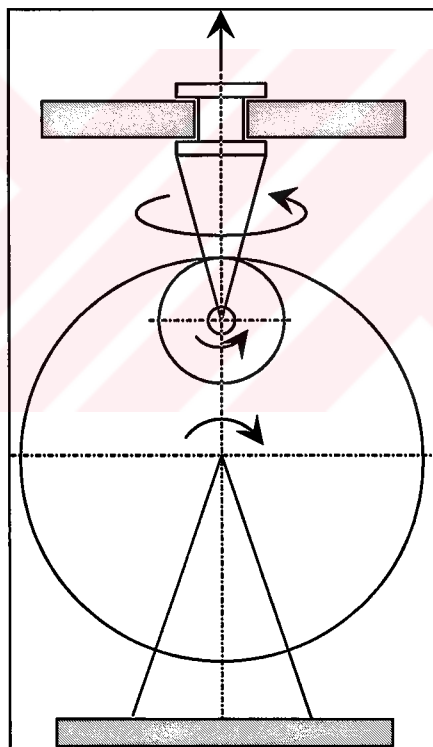


Figure 2.15 Internal Drum Tire Testing Machine

2.6.4 On Road (Mobile) Tire Testing Devices

Although mobile testers perform tire testing in a realistic environment, it is mostly hard to maintain uniform road conditions. The combined dynamics of the vehicle and tire makes interpretation of results harder than that of laboratory devices for the sole characteristics of tires whereas for combined test results of a tire on a specific vehicle, this type of device is desired.

There are different types of mobile testers, some of which are cornering trailers and cornering vehicles. Other types of test vehicles are mostly used for determining traction and braking characteristics of tires (Dugoff and Brown, 1970).

Cornering trailers are mostly three wheeled trailers, one wheel is for stabilizing the vehicle and the remaining two may be steered oppositely and/or camber angles may be adjusted for simulating different operating conditions. By using a three directional force transducer, the response quantities may be determined as the parameters being the trailer speed, tire load, steering and camber angles, tire inflation pressure and the like (Dugoff and Brown, 1970). Figure 2.16 shows the sketch of a typical cornering trailer.

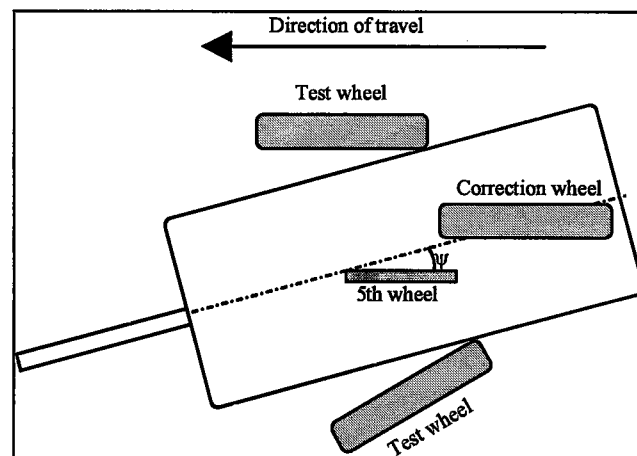


Figure 2.16 Cornering Trailer

One of the existing models of cornering trailers is General Motors Proving Ground Tire Cornering Test Vehicle (Cortese and Rockafellow, 1971). The trailer tires may be swept through a selected angular range of steering while various parameters are recorded. The wheels may be braked at any instant required, the camber angles are adjusted manually before the test starts and remains constant throughout a test run. The control is performed by combined electronic, pneumatic, hydraulic system. Electronic system is used for the control of hydraulic and pneumatic systems as well as for data recording and processing. Pneumatic system has the supply driven by electric motor and, the filtered, dried and regulated air is used in the braking system as well as in the jacks to lift the trailer for changing tires and/or adjusting the camber of tires. Hydraulic power is supplied by a pump driven by the truck engine is used to actuate the slip angle of the wheels and the tracking stabilizer wheel. The following data are measured; tire vertical, lateral, fore-aft forces, angular position of the tire with respect to trailer, camber angle, test wheel angular velocity, trailer angle with respect to direction of travel, vehicle speed (determined by an independent fifth wheel). To obtain these data, four types of transducers are used. Force transducers are used to measure three orthonormal force components generated at the tire. Precision DC tachometers are used to measure the angular velocities of test wheels and the independent fifth wheel (these two data yield wheel slip of the test tire). Cornering angle, camber angle and the angular position of the test wheel with respect to the trailer are measured by angle transducers.

Another test equipment found in literature, which may be classified as a cornering trailer (although it is not exactly) is the Mobile Tire Testing Machine (MTTM) (Holloway et al, 1991). MTTM is connected to a vehicle to test tires. For the first operation trials the vertical load, camber angle, and steering angle are adjusted manually and the authors state that they work on servo control mechanisms to control the above stated quantities. The tests are performed without power application to the tire and it is understood from the paper that two

forces (rolling resistance and side force) and one moment (self-aligning torque) are measured. Variations of these quantities versus controlled variables are plotted. The authors also plan to see the variation of above stated quantities when the test wheel runs on the side of the road or when it goes out of the road.

Cornering vehicles, test tire performance is related to actual tire-vehicle system. Tests may be performed using computerized force transducers or just by measuring the skid threshold on different roads, speeds, radii of curvature and so on (Dugoff and Brown, 1970).

There exists two types of vehicles for combined traction and cornering tests. In non tethered cornering tests, the vehicle is driven on a circle painted on the road, the driver increases the speed of the vehicle half or one mile per hour (0.8 or 1.6 km/h) per lap until the vehicle control is lost or rear breakaway occurs. In tethered cornering tests the test procedure is exactly the same with non tethered cornering test except front axle of the test vehicle is attached to a post at the center of the circular path by a steel cable. In tethered cornering tests, the testing conditions are more uniform in two ways, the test vehicle is positioned on the test circle precisely and the effect of driver skill and style is reduced (Davisson, 1968). Both tethered and non tethered cornering tests include the effect of dynamic behavior of the specific vehicle by which the tests are being performed so the results may not be interpreted as tire characteristics alone but should be interpreted as performance of a specific tire on a specific vehicle.

Table 2.8 summarizes some specific laboratory tire testing devices with their general technical specifications and Table 2.9 summarizes the on-road (mobile) tire testing devices. In both tables only test devices for determining the handling properties are included, other tire testing devices are excluded.

Tire-road contact system as well as friction, tire surface distortion, tread pattern are complex phenomena. In order to estimate handling properties of tires, either oversimplified models are used for rough estimates or tests are performed, which yields variation of handling characteristics versus controlled parameters. Tests are very useful for controlling the accuracy and validity of newly proposed mathematical tire models as well. The main disadvantage of tire tests is that, they do not reveal much about the details of tire road interaction phenomena and needs a test tire prototype in the design stage of a new tire. Nevertheless, tire testing and tire testing devices are still one of the most important components of handling behavior studies.

Table 2.8 Laboratory Tire Testing Devices to Determine Handling Properties of Tires.

Machine	Type	Test Speed	Tire Size	Max. Load	Steer	Camber	Test Conditions	Test Type
General Motors	Flat-Bed	1 mph	17.5 to 40"	2000 lb.	-30 to 30°	-30 to 30°	Dry, Wet, Ice	Steady State
B.F. Goodrich	Flat-Bed	2 fps	24 to 44"	10,000 lb.	-35 to 35° and 90°	-20 to 20°	Dry	Steady State
TIRF	Flat Surface	0 to 200 mph	max. 46"	13,000 lb.	-30 to 30°	-30 to 30°	Dry, Wet, Flooded	Steady State
Flat Trac I	Flat Surface	3.5 and 7 km/h	170 to 450 mm	24,000 N	-15 to 15°	-10 to 10°	Dry	Steady State
Flat Trac II	Flat Surface	-250 to 250 km/h	?	25,000 N	-30 to 30°	-12 to 45°	Dry	Dynamic

Table 2.9 On Road Tire Testing Devices to Determine Handling Properties

Device	Type	Max. Test Speed	Tire Size	Max. Tire Load	Steer	Camber
GM Proving Ground	Trailer	?	?	?	-20 to 20° with 8°/s	-10 to 10°
MTTM	Vehicle Mounted	100 km/h	max. 810 mm	12,000 N	-10 to 45°	-6 to 45°

CHAPTER 3

TIRE TESTING SETUP AND EXPERIMENTS

3.1 Introduction

In order to test the results of the tire model proposed, a simple yet useful tire force and moment characteristics measuring setup is designed and produced in the Automotive Engineering Laboratory of Mechanical Engineering Department, Middle East Technical University. The test setup resembles the external rotating drum types found in the literature as mentioned in Section 2.9. In this Chapter, the design and construction stages of the tire testing setup, its features and usage as well as experiments done on the setup and on other equipment are explained.

3.2 Properties of the Tire Testing Setup

Although there are many types of laboratory and outdoor tire testing machines and setups for obtaining cornering characteristics of tires, as discussed in Section 2.9, the outdoor testing machines, having the disadvantage of uncontrolled road surface conditions, requiring powerful and expensive traction devices, and even some requiring special test tracks, were out of question. There exists many types of laboratory tire testing devices for obtaining the cornering characteristics of tires. The advantages and disadvantages of those machines are discussed in Section 2.9 extensively, with example test machines found in literature. From that discussion, it is evident that in order to obtain the cornering

characteristics of a tire on the road, it is essential to keep the testing conditions as close to real working conditions of a tire as possible. One of the major conditions is the curvature of the road. Under road conditions, tire runs on a straight or very slightly curved roads (in this context, curvature refers not the road curves to the left or to the right but the radius of curvature as at the top of a hill or at the lowest point of a valley). The drum type testing machines have considerably small radius of road curvatures, in the order of a few meters at most. Therefore the drum type test machines, due to having a different pressure distribution at the contact patch than road conditions, are not adequate for obtaining the on-road cornering characteristics. The flat surface tire testing machines do not have this deficiency. On the traveling table type tire testing machines, due to the limited stroke of the table, steady working conditions are not reached. Traveling table test machines are, therefore, adequate for obtaining static properties of tires like longitudinal and lateral stiffnesses. The flat surface tire testing machines, on the other hand, do not possess the so far stated deficiencies. They have flat surfaces similar to road conditions, they may run at high speeds identical or close to real speeds, one may let the tire run long enough to reach the steady state conditions even thermally. The only disadvantage of such devices is that, they are extremely complex and costly. That is why only a few, large research centers have such flat surface tire testing machines and others use drum or traveling table type test machines.

In this thesis, the aim is to test the results of the finite element tire model proposed, not to obtain the cornering characteristics of tires on road. Therefore by supplying the appropriate boundary and contact conditions, the model may yield the cornering force characteristics of a tire rolling on a drum of specified radius. This fact simply states that, the tire may be tested under any controlled condition, and the model may be tuned for the same condition. The key point is that, the cornering characteristics obtained from the computer model must be in agreement with that of the tests. With this fact in hand, if road conditions are supplied to the tire model that yields results in agreement with curved surface tests, one may

expect to get the road behavior of the tire if road conditions are supplied. Now, the constraint of testing the tire under road conditions is removed (but still, the test conditions should not be too far from road conditions), and the only remaining constraint is the simplicity of the test setup. Drum type test machine is the simplest one that can perform tire tests under steady state conditions, so a drum type test machine is selected.

3.3 Design of the Test Setup

Drum, being the heart of the test machine, is supplied by the governmental railways. It is made of specially machined two scrap locomotive wheels, including the axle. The drum has a diameter of 0.979 m and a width of 0.258 m and is driven by a squirrel cage AC electric motor of power 30 kW integral with a gearbox having a reduction ratio of 1:3.8. The electric motor speed is controlled by an electronic frequency controller. The remaining parts are designed according to the drum dimensions. The drum rests on a concrete block which also supports the driving motor and gearbox, and the frame that supports and keeps the tire in desired position. The motor can rotate the drum from 0.26 to 780 rpm corresponding to approximately 0.05 to 148 km/h road speed. The vertical load on the tire is maintained by a pneumatic suspension (air spring) and the tire is connected to the frame by parallelogram linkages which keep the camber angle fixed under different loading conditions. Slip angle and camber angle of the tire are adjusted by the T-slots on the fixed frame and the slots connected to the force transducer. All the six components of tire forces and moments are measured by a six axis compact force transducer having four pylons equipped with strain gages and a preamplifier. The raw data obtained is fed to the computer through a data acquisition card having 12-bit resolution, for storage. Figure 3.1 shows the general view of the setup. In this figure, 1 is the drum, 2 is the gearbox, 3 is the 30 kW driving motor, 4 is the cooling motor and fan of the driving motor, 5 is the parallelogram linkage, 6 is the six-axes force transducer, 7 is the air spring, 8 are

the lower and upper T-slots, 9 is the test tire. Figure 3.2 illustrates the vertical motion of the tire when loaded using two superimposed photographs.

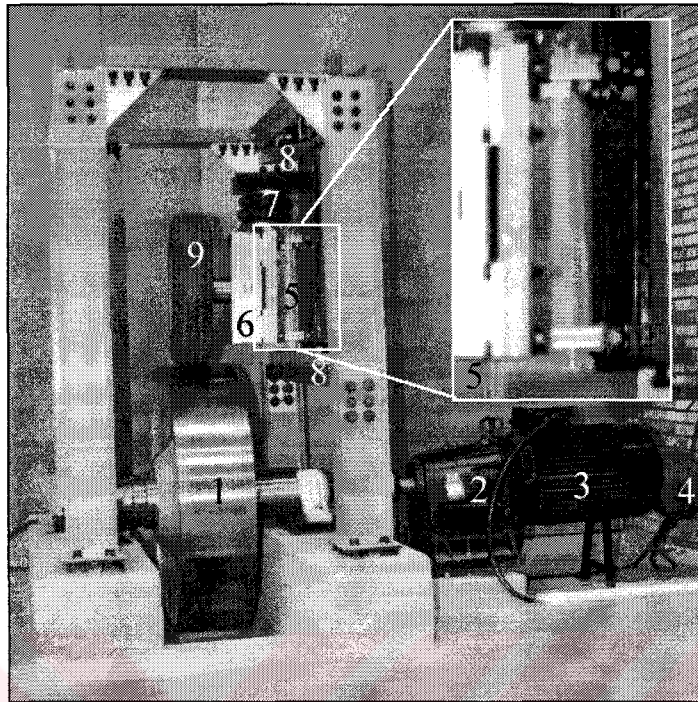


Figure 3.1 General View of Tire Testing Setup



Figure 3.2 The Vertical Tire Motion under Load

3.4 Running Procedure of the Test Setup

3.4.1 Mechanical Preparations

The tire to be tested is mounted on the test setup, the bolts are tightened carefully. To adjust the slip angle to required value, the laser pointer device is used (Figure 3.3). The laser pointer is slid so that plumb line is set to the edge of the drum. For precise measurements, the portion of the drum that is free of paint must be preferred (Figure 3.3 enclosed by white rectangle). The laser pointer must be used with extreme care and all parts of human body and especially eyes must be protected from the laser beam and its reflections. The nuts of the all four T-slots are slightly loosened (Figure 3.4). The nuts must not be over-loosened since doing so may leave the all tire supporting structure including the force transducer free, causing personal injury and damage to the test setup. The lower nuts are tightened to fix the slip angle of the tire and the position of the plumb line is checked once more since the assembly may move back and forth on the slots. If necessary, the screws are slightly loosened and with the aid of a rubber hammer, fine tuning of the tire slip angle is done. By using the hydraulic jack (Figure 3.5) and the bubble (Figure 3.3) on the laser pointer slideway, the camber angle adjustment is done, then the upper nuts are tightened. The hydraulic jack is lowered slowly by the release valve and the jack is taken away. The T-slot nuts and rim bolts must be checked for tightness once more, without overloading them. The laser pointer has to be taken away before the experiment starts. Extreme care should be taken not to leave any tools on the test setup, before the test starts, to avoid personal injury.

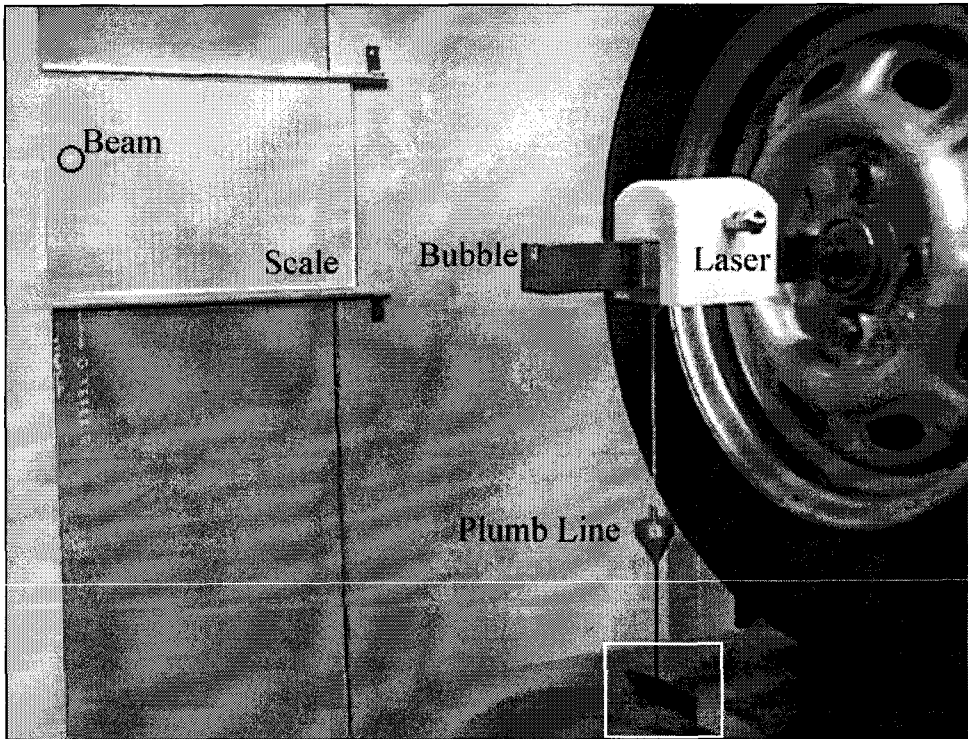


Figure 3.3 Laser Pointer for Slip Angle Adjustment



Figure 3.4 The Lower Two T-Slots for Slip and Camber Angle Adjustments

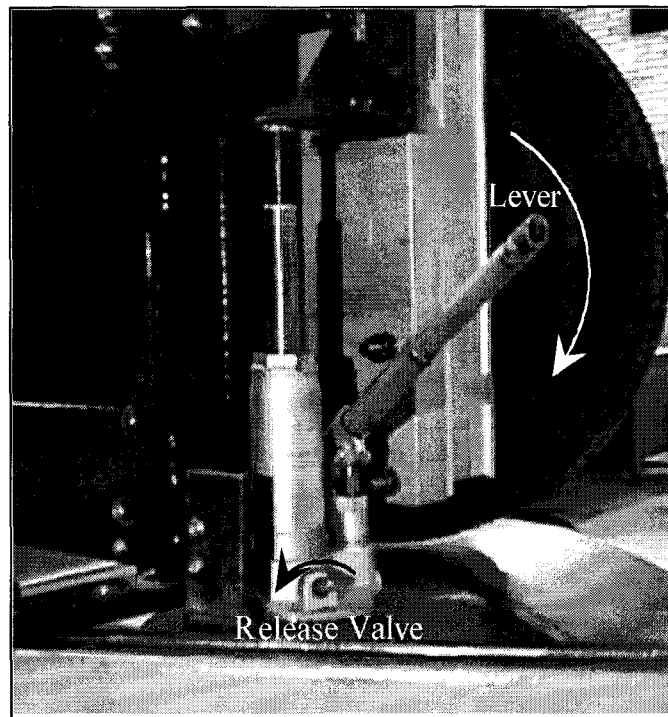


Figure 3.5 Hydraulic Jack for Lifting the Tire

3.4.2. Electronic Preparations

At least 1 hour before the experiment, the six-axis force transducer and the data acquisition computer must be powered up so that they reach to a thermal steady state before the experiment is done (BERTEC, 1996).

When the mains is switched on, the cooling fan of the drive motor as well as that of the electronic speed control unit starts running. The only necessary thing is to set the desired experimental speed. To do that, Pr 01 and/or Pr 02 has to be set to the desired motor shaft speed in rpm. The road and corresponding motor shaft speeds are shown in Table 3.1. Under normal circumstances, no other adjustment of the speed control unit should be necessary. For the detailed key sequence as well as other adjustments of the speed control unit, refer to Section 3.4.3, on speed control unit or the User's Guide of the unit (Control Techniques, 1993).

Table 3.1 Motor Shaft and Corresponding Road Speeds

Road Speed (km/h)	Shaft Speed (rpm)	Road Speed (km/h)	Shaft Speed (rpm)
5	101	70	1420
10	203	75	1521
15	304	80	1623
20	406	85	1724
25	507	90	1826
30	609	95	1927
35	710	100	2029
40	811	110	2232
45	913	120	2434
50	1014	130	2637
55	1116	140	2840
60	1217	147	2982
65	1319	147.89	3000

3.4.3 Programming of Speed Control Unit

The speed control unit can drive standard AC squirrel cage induction motors. The programming can be achieved by the control pod on the unit. The control pod is shown in Figure 3.6.

The upper three keys (MODE, UP and DOWN) are used to adjust the parameter values. The lower three keys (RUN, STOP/RESET and FWD/REV) control the motor operations.

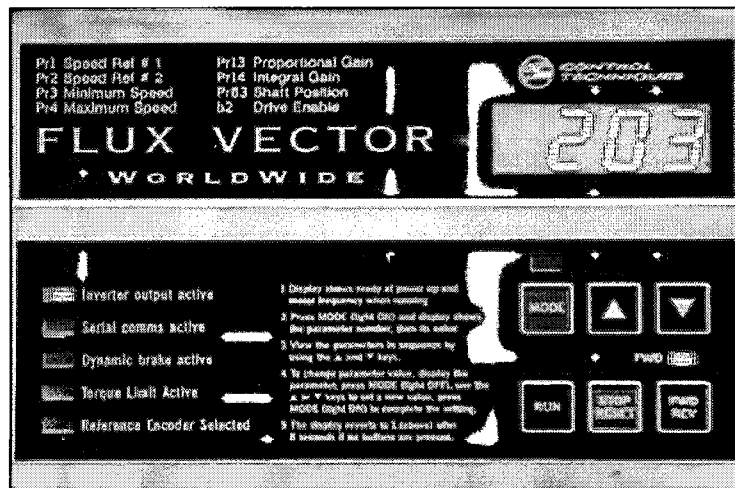


Figure 3.6 The Control Pod of Speed Controller

Programmed parameters may be seen or changed by pressing MODE key once. The parameter LED just above the MODE key illuminates and the parameter with its value are alternately shown. By pressing UP and DOWN keys, the parameter may be changed. With desired parameter selected, pressing MODE once more shows the current value of the parameter. By pressing UP or DOWN key, the desired value may be selected. Pressing MODE once more returns the display to normal mode where the current motor shaft speed is displayed. In parameter selection or setting mode, if no input is made, the display returns to normal mode in eight seconds. The necessary parameter numbers and their identification are summarized in Table 3.2. For a detailed explanation the User's Guide (Control Techniques, 1993) must be referred.

The five LED's on the left of the control pod are system status annunciators. Inverter output active LED indicates that the system is healthy, serial comms active LED indicates there is data transmission through serial link, dynamic brake active LED shows that the motor is in braking mode, torque limit active LED indicates drive is in torque limit and reference encoder selected LED indicates that the shaft encoder on motor controls the position and speed of the drive motor.

Table 3.2 The Necessary Parameters of the Speed Control Unit

Pr 01	Speed Reference 1 (rpm)
Pr 02	Speed Reference 2 (rpm)
Pr 03	Minimum Speed Limit (rpm)
Pr 04	Maximum Speed Limit (rpm)
Pr 06	Torque Limit: Motoring (% of full load torque)
Pr 07	Torque Limit: Regenerating (% of full load torque)
Pr 09	Forward acceleration rate (25 recommended)
Pr 11	Forward deceleration rate (35 recommended)
Pr 41-45	Motor characteristics
b 02	Drive enable
b 06	Speed reference selector (1 for S.R. 1 and 0 for S.R. 2)
b 17	Enable RUN, STOP/RESET, FWD/REW keys (0)
b 22	Open loop (0) or closed loop (1) speed control
b 26	Parameter store (save)

3.4.4 Technical Specifications of the Force Transducer

The force transducer has a unique calibration matrix, which is obtained by individual calibration of each force plate by the manufacturer. The calibration matrix, when multiplied by the signals in Volts coming from six channels, yields forces and moments in Newtons and Newton meters. The conversion from electrical potential to forces and moments are performed as:

$$\begin{Bmatrix} F_x \\ F_y \\ F_z \\ M_x \\ M_y \\ M_z \end{Bmatrix} = \begin{bmatrix} 18543 & -24.7 & 2.0 & 10.0 & -7.8 & -18.4 \\ 14.7 & 18949 & 7.9 & -36.1 & -20.2 & 10.8 \\ -17.0 & 5.1 & 3553.2 & -62.9 & 2.8 & -3.6 \\ -1.4 & -91.0 & -2.9 & 795.9 & 4.3 & 1.5 \\ 90.5 & -5.1 & -1.4 & 7.1 & 784.4 & -1.1 \\ 0.1 & -0.4 & 2.4 & -6.2 & -6.4 & 359.5 \end{bmatrix} \begin{Bmatrix} S_1 \\ S_2 \\ S_3 \\ S_4 \\ S_5 \\ S_6 \end{Bmatrix} \quad (3.1)$$

The coordinate axes of the force transducer is as shown in Figure 3.7, where the x-y plane coincides the top plate outer surface of the force transducer and the origin is at the center of the top plate. To obtain the tire data in SAE coordinate system, the origin of the coordinate system must be translated to the center of the tire contact patch whose horizontal distance is half of the tire section width added to the distance between tire sidewall and transducer top plate (h) and whose vertical distance is the effective rolling radius (ρ) as shown in Figure 3.8. The x-axis of SAE system is in y direction of the transducer axis, y-axis of SAE system is in z direction of transducer and z axis of SAE system is in x direction of the transducer. The measured moments at the transducer coordinate axes is transformed into SAE coordinates by the following relation where italics refer to the transducer coordinate axes:

$$\begin{aligned} M_x &= M_y - hF_x - \rho F_z \\ M_y &= M_z + \rho F_y \\ M_z &= M_x - hF_y \end{aligned} \quad (3.2)$$

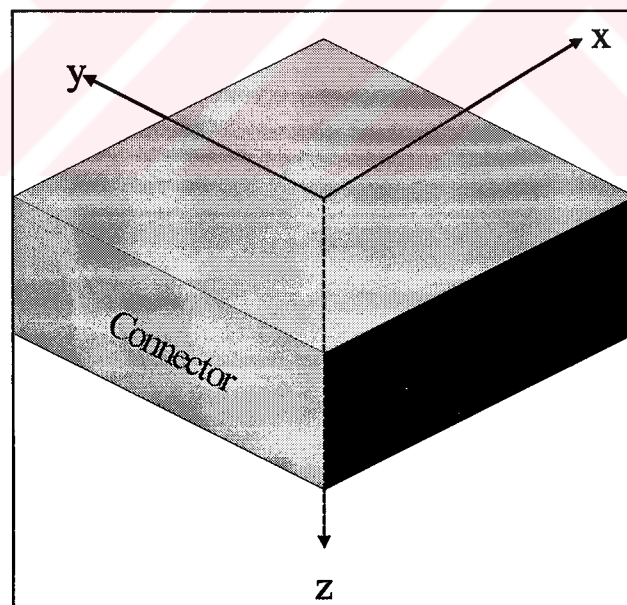


Figure 3.7 Force Transducer Coordinate Axes

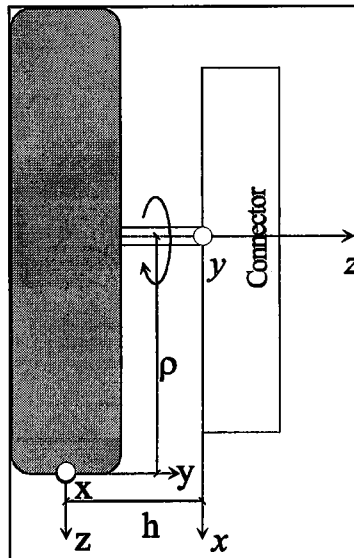


Figure 3.8 Transducer (*italic*) and SAE Coordinate Axes

3.4.5 Tire Testing

Before the test starts, the bolts of the rim and the position adjustment bolts must be checked without overloading them. The test tire must be jacked up for zero setting. Please refer to Figure 3.5 for jacking the tire. During zero setting it is essential to check that tire is not lowered due to leakage in the jack. The cold inflation pressure has to be checked during this period and the tire must have rested at least for 2 hours to be identified as cold. The tire may be lowered for the testing position after the message showing the zero calibration has ended is seen. The jack must be taken away immediately after the tire is lowered and should never be left on the test setup while the tire test is being performed. Before the driving motor is energized, it must be checked that no tools are left on the test setup nor on the tire, to avoid personal injury. The driving motor must be started, before the tire is loaded by the pneumatic suspension. While the driving motor is running, nobody should be in front of the test machine where there exists no protective cage. The tire vertical loading must be started after the drum speed has reached to its steady state value, which is understood by the steady motor speed seen at the speed control unit display. The loading and unloading must be done

incrementally until the desired vertical tire load is reached. The pressure in the air spring should not exceed 250 kPa (2.5 bars or 36 psi on gage), not to overload the force transducer. Before the experiment is started, the tire must be conditioned for at least 15 minutes by running it under medium vertical load and no slip angle. At higher slip angles where the tire makes excessive noise, the protective headphones are advised to be used. It should be kept in mind that due to high inertia of the test drum, it takes some time to stop the test setup. In case of mains failure or power loss, since dynamic braking is not available, it takes much longer for the test setup to come to a rest.

3.5 Static Tire Tests

3.5.1 Tests on Flat Surface

In order to verify the results of static tire models on computer, some experiments are performed to obtain the load-deflection characteristics and contact patch size and shape of an actual tire prior to the construction of the test setup. The tire used in experiments is a 155 R 13 78 S one textile body ply and two steel tread plies automobile tire. The tire is a used one with an average tread depth of 3 mm where the new tires have about 7.5 mm tread depth.

Before the experiment, the tire is inflated to one of 165, 180 or 200 kPa, then pressed towards ground by a known force and the resulting hub deflection is measured. In some instances, the contact patch shape is obtained by introducing a carbon and a paper between the tire and the ground. The load-deflection characteristics of the 155 R 13 tire is presented in Figure 3.9 and a contact patch shape is presented in Figures 3.10.

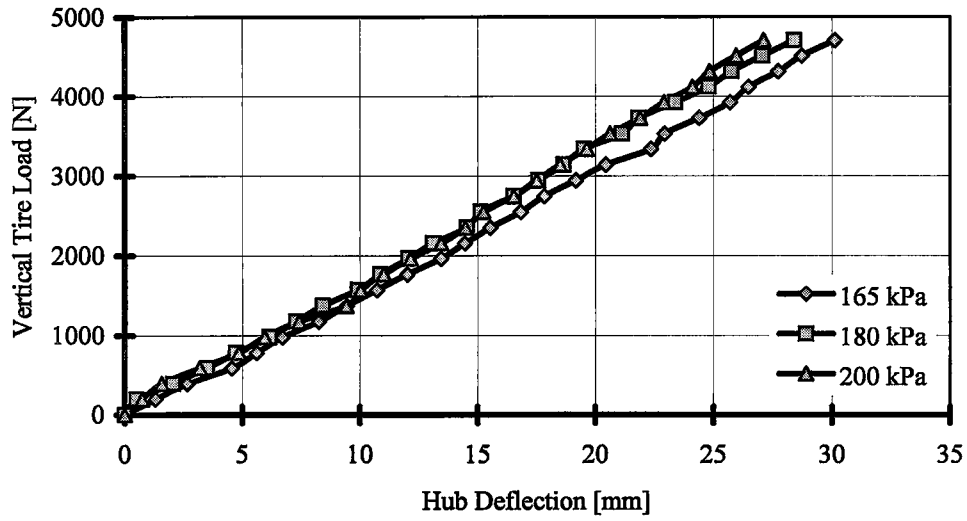


Figure 3.9 Experimental Load-Deflection Characteristics of 155 R 13



Figure 3.10 Contact Patch of 155R13 on Flat Surface with 180 kPa Inflation Pressure and 4160 N Vertical Load

3.5.2 Tests on Curved Surface

With the construction of the test setup, more precise static tests can be performed on the drum of the test machine. The old 155R13 and a new one are tested on the drum. The old tire has an average tread depth of 3 mm and the new one has 7.5 mm. Figure 3.11 shows the experimental load-deflection characteristics of both tires on the test drum. The old tire is slightly softer than the new tire at lower loads while it stiffens at higher loads due to low tread depth. The new 155R13 has nearly linear force-deflection characteristics on the drum.

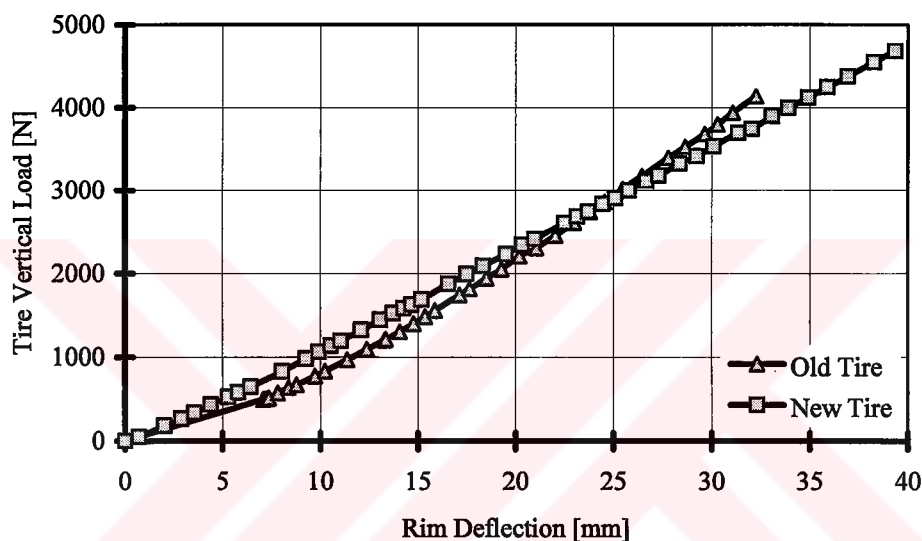


Figure 3.11 Load-Deflection Characteristics of Old and New 155R13 Tires on Test Drum

3.6 Initial Cornering Test Results of the Setup

The first cornering test on the test setup was performed on December 11, 1997. The test speeds were 7.4 and 24.6 km/h (corresponding to 150 and 500 rpm motor shaft speeds). The test tire was a used 175/70R13 having one textile body ply and two steel tread plies with 4 mm tread depth. The tire was inflated to 180 kPa (26 psi). The first test was performed with 7.4 km/h speed and at 2, 3 and 4 kN tire load. The slip angle was set to -2, 0, 2, 4, 6, 8 and 10 degrees with the aid of

a mechanical positioning device. The driving motor was not able to rotate the drum at 10 degrees with a load of 4 kN. The results of these two test runs are presented in Figure 3.12 and 3.13.

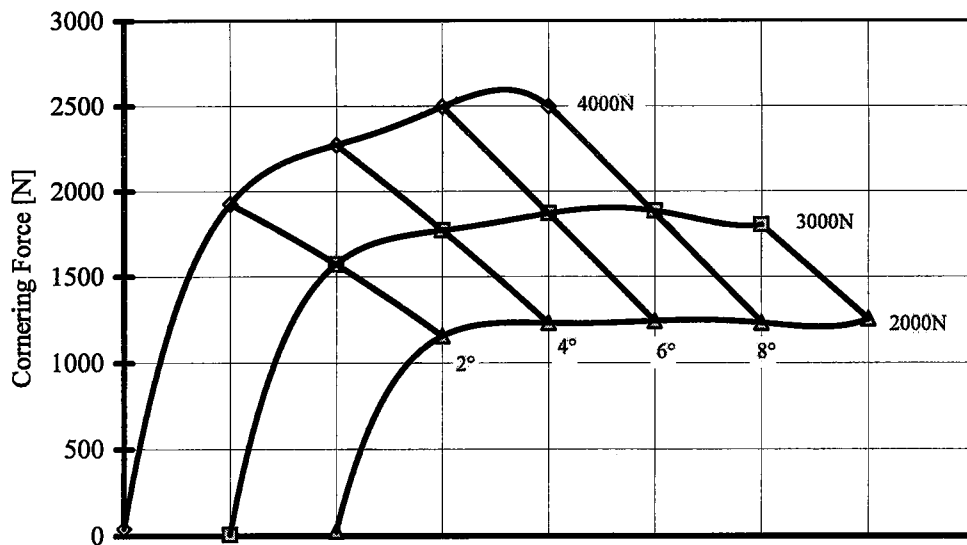


Figure 3.12 Cornering Force Characteristics of 175/70R13 at 7.4 km/h Speed with 2 Degree Slip Angle Incrementation

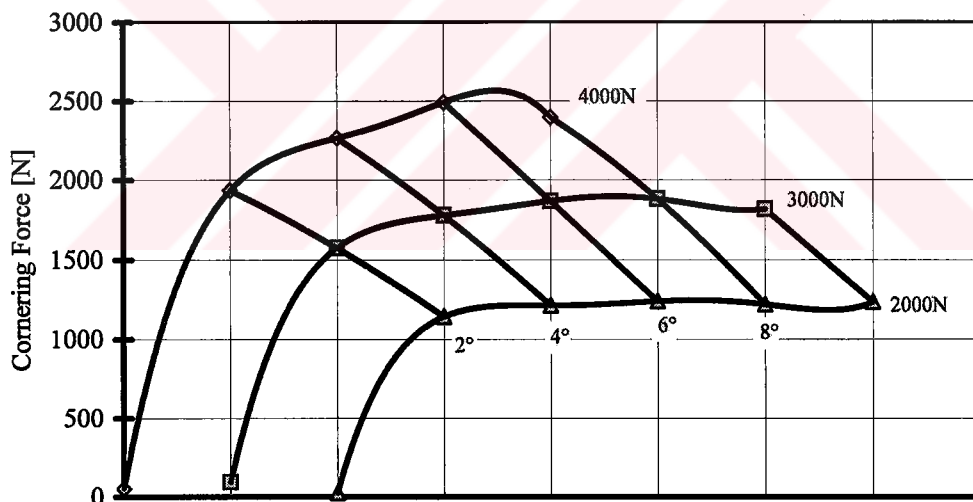


Figure 3.13 Cornering Force Characteristics of 175/70R13 at 24.6 km/h Speed with 2 Degree Slip Angle Incrementation

The two carpet plots are very similar except some experimental errors. For such low speeds, the effect of road speed cannot be extracted by the present

accuracy of the test setup. The plots reveal that more data has to be taken for low slip and the tire may be loaded with more number of increments to higher loads to generate smoother curves.

Figure 3.14 shows the results of the second test run of the tire testing machine. During this experiment more data points are obtained so that a carpet plot would be drawn. The tire tested is 175/70R13 with one textile body ply and two steel tread plies at 180 kPa (26 psi) inflation pressure again.

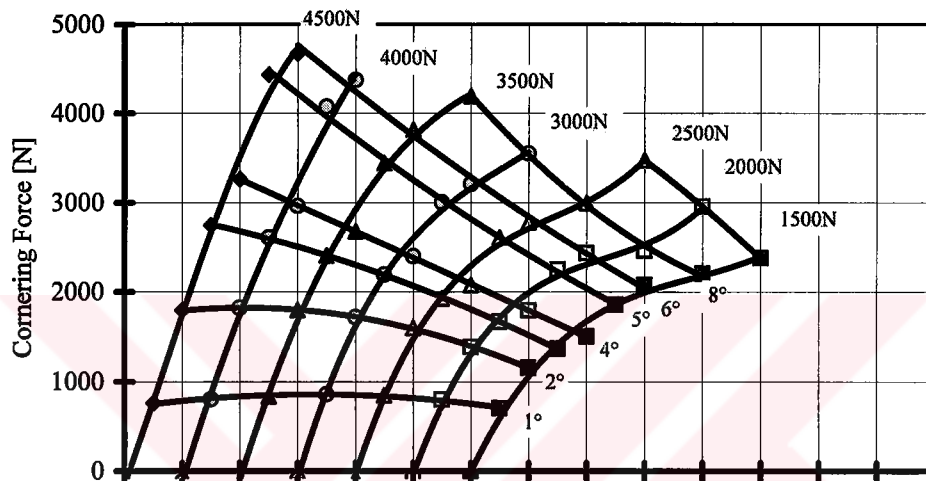


Figure 3.14 The First Detailed Tire Testing of 175/70R13

Figure 3.14 reveals serious experimental errors due to imprecise tire positioning. With a mechanical tire positioning device, the dominant error is at the slip and camber angles of the tire. A precise equipment to position the tire would be optical, therefore the positioning device schematically shown in Figure 3.15 is devised using a standard laser pointer used for presentation. The laser pointer slides on a ground slideway. With the aid of a plumb line, the pointer is positioned just at the edge of the drum. The slip angle of the tire is pointed on a screen which is 1320 mm away from the tire axle. With this configuration, the laser beam moves 23.0 mm for 1 degree change in the slip angle. Another advantage of using laser beam is, the slip angle can be monitored during the

experiment, provided that the vertical motion of the tire (i.e. the change is vertical load) is small. In case of large vertical movements, the position of the laser beam must be corrected using the plumb line since the parallelogram linkage causes back and forth motion of the laser. With the laser pointer mounted on the tire testing setup, the test result of the same tire, is shown in Figure 3.16. The change in curve trends in 2000 and 4000 N around 6 degree slip angle is due to some loose bolts in the frame of the test machine, which are tighten to torque after this experiment. The detailed usage of the laser beam positioning device is explained in Section 3.4.1.

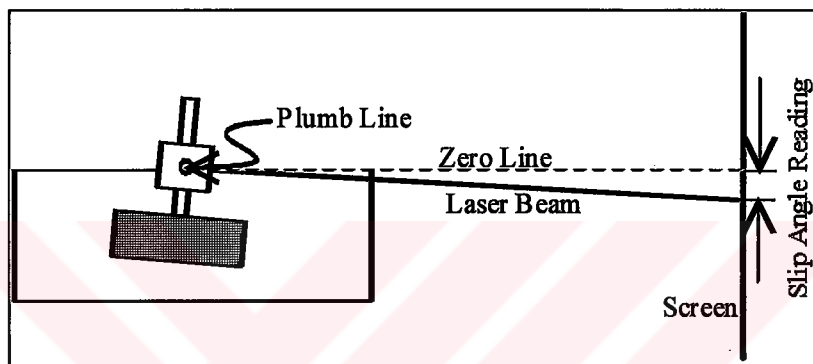


Figure 3.15 Schematic Representation of Optical Positioning Instrument

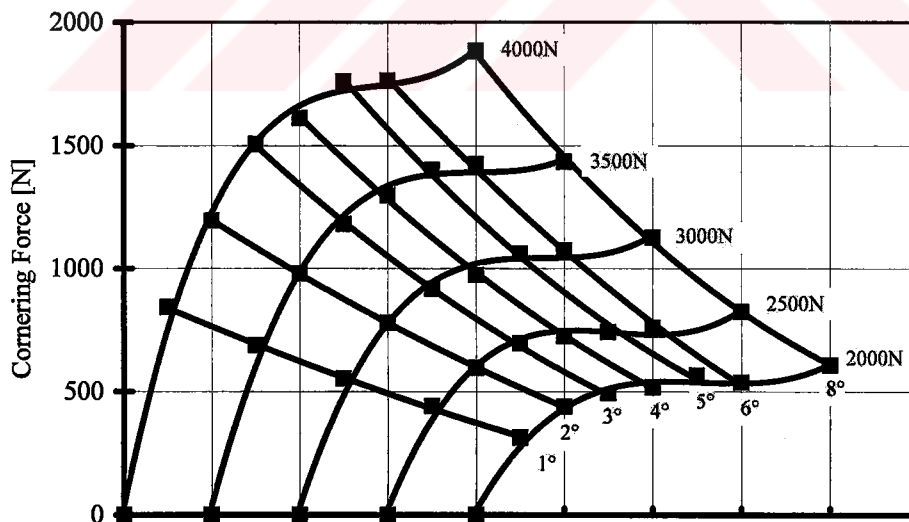


Figure 3.16 The First Test with Laser Beam Positioning Device

3.7 Error Analysis of Test Setup

The tire testing results have some experimental uncertainties. The main sources of these uncertainties and their detailed treatment are presented, and their combined effect is demonstrated on a carpet plot.

3.7.1 Tire Positioning Errors

The laser pointer can be positioned with ± 5 mm accuracy which makes an uncertainty of ± 0.22 degrees in slip angle.

3.7.2 Force Transducer Accuracy

The accuracy of force plate is typically ± 2 N for force measurements and ± 1 N m for moments (Berme, 1998).

3.7.3 Electrical Noise

The electrical noise, when the drive motor is not powered is less than ± 10 bits with standard deviation less than 4 bits whereas it increases to ± 80 bits with a standard deviation of 11 bits when the motor is running. Electrical noise is rather random and does not affect the mean value of the measurements significantly.

3.7.4 Analog-to-Digital Conversion Accuracy

The data acquisition card input range is set to ± 2.5 V, card having 12 bit ($2^{12} = 4096$ discrete steps) resolution, corresponding to bit has a resolution of 1.22 mV and a deviation of ± 0.61 mV. The data acquisition card manufacturer (PCL-718 User's Manual, 1990) states that the analog-to-digital conversion accuracy is $\pm 0.01\%$ of reading ± 1 bit which makes ± 0.5 mV ± 1.22 mV at full scale. The

overall accuracy of analog-to-digital conversion is better than ± 1.8 mV. In terms of force and moment, this makes ± 3.5 N for rolling and vertical forces, ± 6.5 N for cornering force, ± 1.5 N m for overturning moment and self-aligning torque and ± 0.7 N m for rolling resistance.

3.7.5 Accuracy of a Data Point on Carpet Plot

The combined accuracy of a data point on the carpet plot, on a conservative side may be estimated depending on the discussion in sections 3.7.1 to 3.7.4 as:

Tire Positioning Error: ± 0.22 degrees

Cornering Force Error: ± 10 N

The vertical load is adjusted by the air pressure in the pneumatic suspension and this adjustment is done while the tire is rolling at the test conditions. Due to circumferential nonuniformities of the tire, vibrations and wheel shimmy the average vertical tire load accuracy can only be set with an accuracy of $\pm 1\%$ of the present tire load.

The tire positioning error causes a horizontal uncertainty on the graph and cornering force error causes a vertical uncertainty. The error in vertical tire load on the other hand causes an uncertainty normal to the curve at the point of interest which varies along the curve. The dispersion of a point is therefore similar to the one shown in Figure 3.17. Another uncertainty, whose effect cannot be predicted directly is in cold inflation pressure. The electronic pressure gage has an accuracy of ± 1 psi (± 7 kPa) and inflation pressure is not monitored during the experiment.

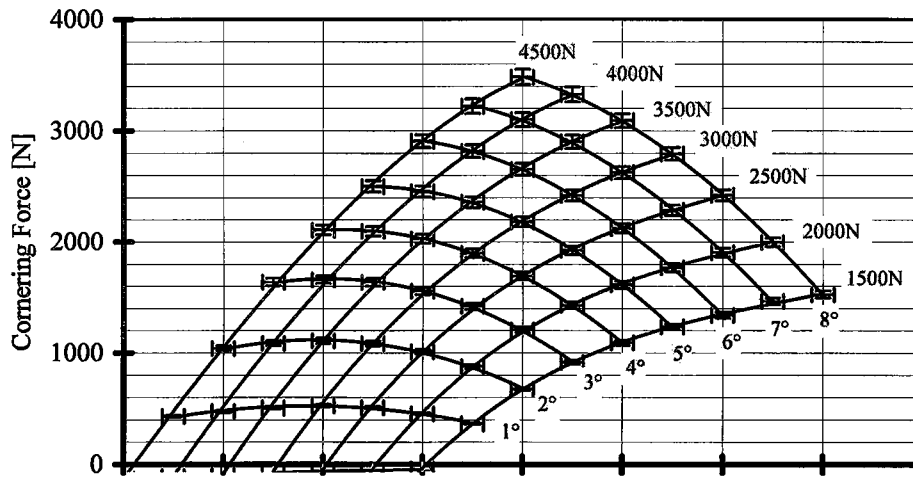


Figure 3.17 Data Points and Their Dispersion on Carpet Plot (155 R13, 180 kPa Inflation Pressure and 10km/h Test Speed)

3.8 Test Results

With the test runs, the problems about the tire testing setup are corrected. The tire tests with the 155R13 with one textile body ply and two steel tread plies are performed to validate the computer model.

3.8.1 Low Speed Cornering Test

The first test done on the tire that is modeled is at nominal inflation pressure of 180 kPa (26 psi) and 10 km/h road speed. The cornering force data is presented in Figure 3.18 The vertical load varies from 1500 N to 4500 N with 500 N increments and slip angle varies from 0 to 8 degrees with 1 degree increment.

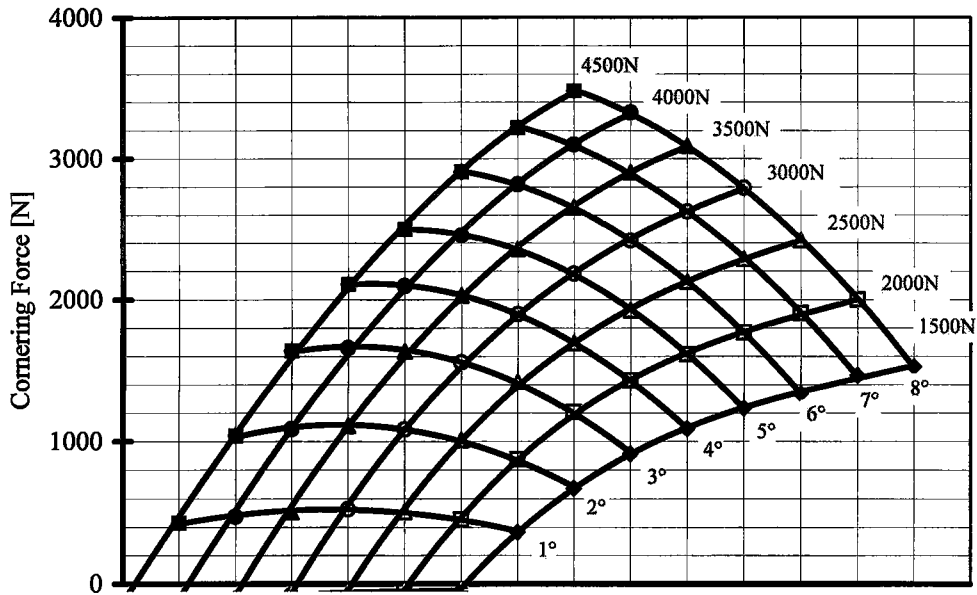


Figure 3.18 Cornering Force Characteristics of 155R13 at 180 kPa Cold Inflation Pressure and 10 km/h Road Speed

3.8.2 Effect of Inflation Pressure on Cornering Characteristics

As mentioned in many works (Bird, et al., 1973, Drach, et al., 1991) cornering characteristics of a tire depends on cold inflation pressure. With increasing inflation pressure around rated pressure the cornering force generated by the tire increases at the same vertical load and slip angle, and it decreases as the pressure decreases. The experiments done with 10 % less (165 kPa, 24 psi) and 10 % more (200 kPa 29 psi) show this tendency clearly. The effect of inflation pressure can be seen on Figure 3.19.

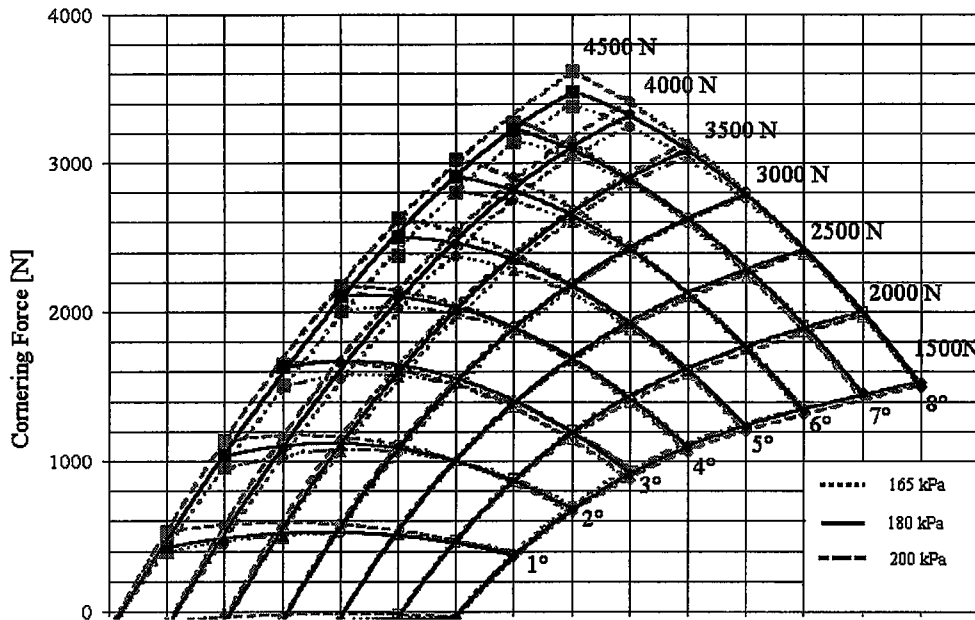


Figure 3.19 Effect of Cold Inflation Pressure on Cornering Characteristics

3.8.3 Effect of Test Speed on Cornering Force Characteristics

To see the effect of roadway speed on cornering force characteristics the tire test is repeated at 30 and 60 km/h road speeds as well. At high vertical load high slip angle combinations, the tire heated up very much and permanent damage occurred on the tread pattern as shown in Figure 3.20. Again due to very high tread and sidewall temperatures on tire, the slip angle was limited to 7 degrees. The cornering force characteristics of the tire at different road speeds are presented in Figure 3.21. Pottinger and coworkers (1976) in their extensive paper about the effect of test speed and surface curvature on cornering properties found out that for a speed increase from 6 mph (10 km/h) to 75 mph (120 km/h) cornering force shows significant increase (8 to 10 %) for all normal loads for slip angles up to 2 degrees, slight increase (about 5%) for 4 degrees and no significant change for slip angles in the range 8 to 20 degrees. The tire tested is a steel belted radial tire GR70-15. With these observations, which is the only available one in open literature, it is deduced that the decrease in cornering force at high speed is due to high temperature and permanent deformation and damage on the tire tread.



Figure 3.20 Tread Damage After High Speed High Slip Angle Test (Arrows Show Missing Blocks, Ellipses Show Stuck Rubber on Tire)

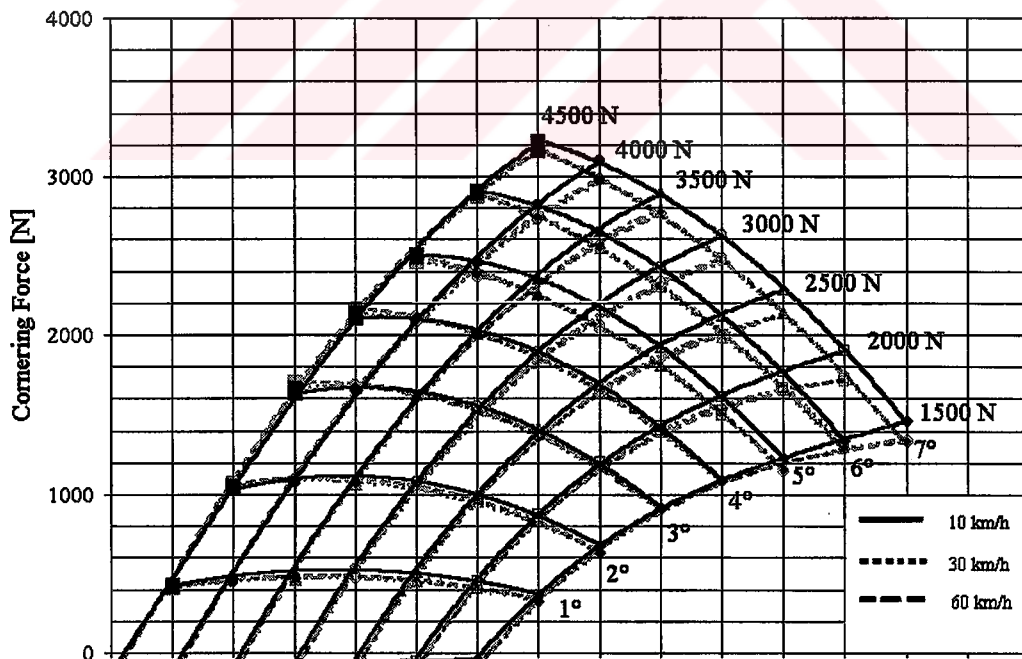


Figure 3.21 Effect of Roadway Speed on Cornering Properties

CHAPTER 4

MATERIAL REPRESENTATIONS AND ELEMENT FORMULATIONS IN FINITE ELEMENT MODELING

4.1 Introduction

Tire, made of vulcanized rubber and a reinforcing carcass, is a highly anisotropic, viscoelastic, and composite structure. Large strains, displacements and rotations encountered in normal service conditions of tire, considerable temperature dependent material properties of rubber and textile cords, together with the nonlinear stress-strain characteristics of rubber (for example Green and Zerna, 1960, Green and Adkins, 1960, Malvern, 1969), further complicates the model. Figure 4.1 shows the construction of a typical radial tire with reinforcement. The very high moduli of textile and steel cords when compared to that of rubber, micro-buckling of cords in compression still add more complications. Frictional contact problems are inherently nonlinear and path dependent. Nonlinearity in the analysis occurs partly because the contact patch and its pressure distribution are not known beforehand. Path dependency is a result of nonconservative (dissipative) character of frictional forces. In modeling the friction between tire and road, most researchers agree that the classical dry friction (Coulomb) theory is not sufficient to represent the rubber friction thoroughly, although they cannot propose a more general and widely accepted theory, modeling the actual physical situation (Sakai, 1981, Noor, 1985, Seifert, 1998).

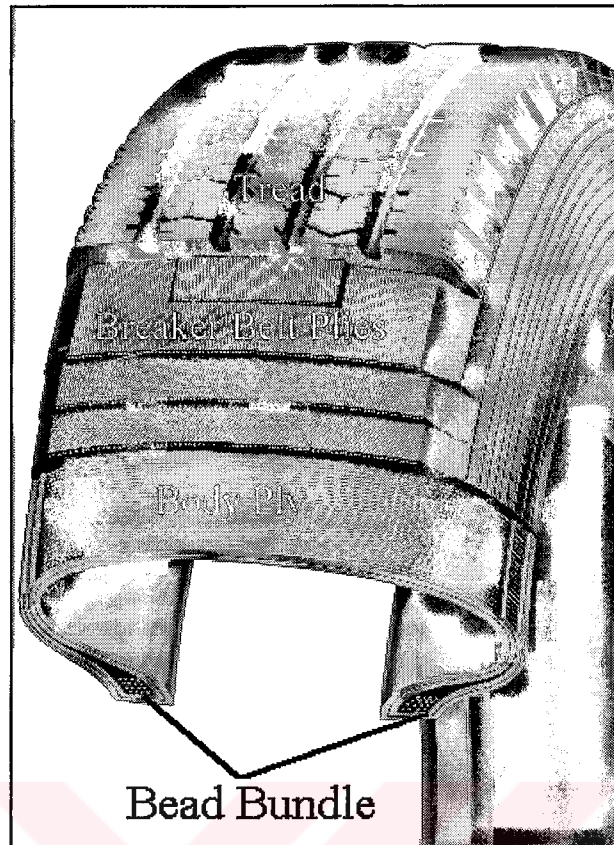


Figure 4.1 Construction of a Typical Radial Tire

4.2. Geometric Nonlinearities

4.2.1. Large Displacements and Large Strains

Under normal service conditions of tires, displacements due to footprint loading are quite large, and strains induced are moderately large. Furthermore, in cornering analysis, rigid body motion due to rolling cannot be avoided. These facts necessitate a geometrically nonlinear analysis. The very detailed mathematical treatment of geometric nonlinearities encountered in elasticity may be found in Green and Zerna (1960) and Green and Adkins (1960). Here only the theoretical foundations which are necessary for finite element formulations will be presented.

In small displacement-small strain theory, since displacements and strains are very small compared to overall dimensions of the structure, there is negligible distinction between deformed and undeformed configurations, whereas in case of large displacements, and/or finite rotations, and/or finite strain, the difference between the undeformed (initial and mostly the unstrained) configuration and deformed (final) configuration cannot be neglected. In the presence of geometric nonlinearities, the quantities like stress and strain are either referred to initial configuration or present configuration. In linear theory, stress is the force per unit area whereas in geometrically nonlinear case, it may be the force per unit deformed area which is called the Cauchy (or sometimes true) stress or it may refer to undeformed configuration (both force and configurationwise) as in the second Piola-Kirchhoff stress. The distinction between the material (Lagrangian) formulation, and spatial (Eulerian) formulation is evident too.

For the finite element analysis of pneumatic tires, material (Lagrangian) description is suitable for most of the cases since the undeformed configuration and second Piola-Kirchhoff stress as a function of strain (or strain rate) are known. On the other hand, for cornering analysis, it may be advantageous to model the rigid body rotation of the tire by spatial (Eulerian) description. It should be noted that, even for linear elastic material response, the large displacement, large strain formulation yields nonlinear set of equations.

Since displacement formulation (and sometimes mixed formulation for incompressible materials) is used in finite element applications, the quantities like stress and strain will be expressed in terms of displacements, although other forms exist too.

The equilibrium equations are

$$\frac{\partial \sigma_{ij}}{\partial x_j} + q_i = 0 \quad (4.1)$$

where σ is the true (Cauchy) stress tensor and q is the distributed load per unit volume in deformed configuration. This equilibrium equation is equivalent to the virtual work expression as in the case of linear theory, which is

$$\int_v \sigma_{ij} \frac{\partial \delta u_i}{\partial x_j} dv = \int_v q_i \delta u_i dv + \int_s t_i \delta u_i ds \quad (4.2)$$

here, t is the boundary traction and the integrations are carried over the current (deformed) configuration. An expression referring to the known undeformed configuration would be more useful than the expression referring to the deformed configuration, which is not yet determined. Using the Jacobian of deformation which is

$$J = \frac{dv}{dV} = \left| \frac{\partial x_i}{\partial X_j} \right| = |F_{ij}| \quad (4.3)$$

the virtual work expression may be referred to undeformed configuration as

$$\int_v J \sigma_{ij} \frac{\partial \delta u_i}{\partial x_j} dV = \int_v Q_i \delta u_i dV + \int_s T_i \delta u_i dS \quad (4.4)$$

where

$$\begin{aligned} Q_i &= J q_i \\ T_i &= \frac{ds}{dS} t_i \end{aligned} \quad (4.5)$$

The second Piola-Kirchoff stress tensor S is defined as

$$J \sigma_{ij} = F_{ik} S_{kl} F_{jl} \quad (4.6)$$

The nonlinear strain tensor, referred as Green-Lagrange strain tensor in terms of displacements is

$$E_{ij} = \frac{1}{2} \left(\frac{\partial u_i}{\partial X_j} + \frac{\partial u_j}{\partial X_i} + \frac{\partial u_k}{\partial X_i} \frac{\partial u_k}{\partial X_j} \right) \quad (4.7)$$

where, the second order term is negligible for infinitesimal strain and displacement analysis, therefore Green-Lagrange strain boils down to infinitesimal strain.

Taking the variation of Green-Lagrange strain tensor and manipulating the virtual work expression, each quantity is referred to undeformed configuration as

$$\int_V S_{ij} \delta E_{ij} dV = \int_V Q_i \delta u_i dV + \int_S T_i \delta u_i dS \quad (4.8)$$

using the material constitutive relation, the second Piola-Kichhoff stress tensor may be expressed in terms of Green-Lagrange strain tensor since both refer to the global axes in undeformed configuration. For linear elastic material for example, the constitutive equation is

$$S_{kl} = L_{kij} E_{ij} \quad (4.9)$$

and the virtual work expression becomes

$$\int_V E_{ij} L_{ijkl} \delta E_{kl} dV = \int_V Q_i \delta u_i dV + \int_S T_i \delta u_i dS \quad (4.10)$$

which is a nonlinear set of equations even for linear elastic materials.

4.2.2. Pressure Loading in Large Displacement and Rotation Analysis

In geometrically nonlinear analysis, pressure loads are applied on the deformed structure (present configuration), therefore the equivalent nodal loads are dependent on the nodal displacements. This dependency leads to additional contributions to the stiffness matrix in the solution procedure. The external virtual work is

$$\delta W^E = \int_A \delta u_i n_i p dA \quad (4.11)$$

where A is the surface on which the pressure load p is applied, n is the normal to this surface pointing into the material, δu is the virtual displacement field. In a three dimensional space, the expression $n_i dA$ may be rewritten as

$$n_i dA = \frac{\partial x_j}{\partial g} \frac{\partial x_k}{\partial h} \epsilon_{ijk} dg dh \quad (4.12)$$

where \mathbf{x} is the current position of a point on the surface and the surface parametric coordinates (g, h) are chosen to give the correct sign to \mathbf{n} through the cross product. The incremental external virtual work is then given by

$$d\delta W^E = \int_{g,h} p \delta u_k \cdot \left(\frac{\partial du_i}{\partial g} \frac{\partial x_j}{\partial h} \epsilon_{ijk} + \frac{\partial x_i}{\partial g} \frac{\partial du_j}{\partial h} \epsilon_{ijk} \right) dg dh \quad (4.13)$$

which is nonlinear.

4.2.3 Finite Element Formulation for Geometric Nonlinearities

For most of the problems, if not enforced by other reasons, displacement formulation is used for finite element formulation. The displacement at a point within a definite element is therefore

$$\underline{u}_i^e = \underline{N}_i^e(\underline{X}_k)\underline{u}^e \quad (4.14)$$

where the underlined quantities refer to the nodes of the element under consideration. \underline{u}^e is the nodal displacement vector of the element and $\underline{N}_i^e(\underline{X}_k)$ is the interpolation (shape) function components of the element evaluated at point \underline{X}_k . With the discretization of nodal displacements, the virtual work expression written in terms of displacements can be expressed as functions of nodal displacements and interpolation function of the elements. The Green-Lagrange strain tensor takes the form

$$\underline{E}_{ij}^e = \frac{1}{2}(\underline{B}_{ij}^e + \underline{B}_{ji}^e + \underline{B}_{ki}^e \underline{u}^e \underline{B}_{kj}^e)\underline{u}^e \quad (4.15)$$

where

$$\underline{B}_{ij}^e = \frac{\partial \underline{N}_i^e}{\partial \underline{X}_j} \quad (4.16)$$

The virtual work expression is therefore converted into the following discretized form

$$\left[\sum_e \int_{V^e} \frac{1}{2} \underline{S}_{ij}(\underline{B}_{ij} + \underline{B}_{ji} + \underline{B}_{ik} \underline{u} \underline{B}_{kj} + \underline{B}_{kj} \underline{u} \underline{B}_{ki}) dV^e \right] \delta \underline{u} = \underline{P} \delta \underline{u} \quad (4.17)$$

where \underline{P} is the consistent nodal load to account for external body forces and surface tractions. The equivalent nodal parameters for the second Piola-Kirchoff stress tensor can only be inserted if the material constitutive law is known and can be solved for nodal displacements. For linear elastic materials,

$$\underline{S}_{ij} = \frac{1}{2} L_{ijkl} (\underline{B}_{kl} + \underline{B}_{lk} + \underline{B}_{mk} \underline{u} \underline{B}_{ml}) \underline{u} \quad (4.18)$$

The system of equations is therefore expressed as

(4.19)

where the internal load vector Q is

(4.20)

The tangent stiffness matrix \underline{K}^t accounts for elastic stiffness of the material, initial stress stiffness and geometric stiffness, therefore it depends on nodal displacements. It can be decomposed as

(4.21)

where \underline{K}^e is the elastic stiffness matrix defined as

(4.22)

where β_{ijk}^0 is the constant symmetric shape function gradient, D_{mnpq} is the material tangent coefficients. \underline{K}^g is the initial displacement (geometric) stiffness matrix, defined as

(4.23)

where β_{ijk}^u is the displacement dependent symmetric shape function gradient. \underline{K}^s is the initial stress stiffness matrix, defined as

(4.24)

where $N_{i,k}$ is the shape function gradient matrix.

4.3 Modeling the Composite Material Properties and Anisotropic Material Behavior

4.3.1 Some Approaches in Literature to Model Unidirectional Long Fiber Composites

Research on determination of stress-strain relationships of composites is rather old. One of the earliest approaches is to assume the composite as an

orthotropic homogeneous material. Furthermore the deformations and strains are assumed to be small and Hooke's law is obeyed for all the constituents of the composite. The material elastic constants are either determined experimentally or by some calculations under rather strict assumptions. The method of estimating the elastic constants is very similar to determination of equivalent spring stiffness when springs are in parallel or in series (Aston et al., 1969, Parratt, 1972, Walter, 1978). This approach is a useful tool which yields quite precise results as long as the assumptions are not violated severely. The method is extended to Halpin-Tsai composite material models, which contain empirical factors to account for slight violations of strict assumptions. Halpin-Tsai composite material models include long and short fiber, long and short ribbon and particulate composites (ABAQUS/Pre Version 5.4-1 User's Manual). This approach is used in some recent works as well to model the tire composites and the analyses yielded results those are in good agreement with experiments (Tanner, 1996a, 1996b, Davis, 1997).

Tire composites, having rubber as the matrix, and textile and/or steel reinforcement violate the assumptions of the above stated averaging methods as:

1. The strains are assumed to be small (infinitesimal to be exact) and material remains linear elastic. Although nonlinear stress strain relationship of rubber may be approximated by a linear elastic constitutive law for small strains, microbuckling of reinforcing fibers in compression cannot be modeled by a linear elastic law.
2. Due to large difference between the matrix and reinforcement moduli, averaging has great impact on local properties like stresses on reinforcement.

Furthermore, averaging, by itself is an approximation which introduces considerable error if proper care is not taken on element size in finite element

modeling. Additional effort is required for averaging prior to analysis and to recover the stress distributions in the individual constituents.

The determination of elastic properties of twisted filaments from the extensive work of Walter (1978) is applicable to the models where averaging is not used. The effective Young's modulus of twisted filaments in tension is estimated as

$$E_c = \frac{E}{1 + 4\pi^2 R^2 T^2} \quad (4.25)$$

where E_c is the effective modulus of twisted cords in tension, E is the non-twisted elastic modulus, R is the yarn radius and T is the twist per unit length.

4.3.2 Initiation of Rebar Concept

The most common composite which violates the rule of mixtures is concrete reinforced by steel rods. Since concrete cannot be modeled by a simple linear elastic constitutive law, Ngo et al. (1967) proposed modeling steel reinforced concrete beam by superimposing one dimensional bar elements on elements modeling concrete. The bar and concrete elements satisfy the displacements at the common nodes and they are compatible elements. Watanabe, et al. (1983) applied the same approach to the finite element modeling of bias-ply motorcycle tires. Although the concept is simple and very useful, this method has a serious disadvantage. The location and orientation of reinforcing cords affect the finite element discretization of the model. This disadvantage becomes more serious when the number of the reinforcing cords are high as in the case of tires.

The obvious advantage of superimposing reinforcing bars on a matrix is that, the matrix and reinforcement have different constitutive equations (material laws) as well as may have different failure criteria (like cracking in concrete and yielding in steel reinforcement). This advantage led to the development of a new

concept which is named as *rebar* (*reinforcing bars*). In some finite element softwares rebar is implemented as an option to the element (like ABAQUS) which inserts different reinforcing material into the matrix, having its own material properties, fiber orientation and thickness, whereas others formulate the same concept with special elements called rebar (like ANSYS and MARC). In case of having separate rebar elements, the rebar element is *superimposed* to matrix element, which means, the nodal displacements of the rebar and matrix elements are the same. Originally, rebar concept was restricted to two dimensional cases and mostly small deformations, now the rebar elements are evolved to model three dimensional cases with large strain and/or with twist. Several layers of reinforcement having different fiber orientations and/or material properties can be modeled within a single element precisely, which reduces the effort of discretization and computation. The bending effects in the bars are neglected in most of the rebar formulations since reinforcement diameters are usually small when compared to structural dimensions.

4.3.3 Unidirectional Fibrous Composite Material Modeling in ABAQUS Standard: *REBAR Option

Rebar option is used to define the reinforcing in elements, such as steel reinforcing bars in concrete. It can be used for beam, shell and solid (continuum) elements. The material properties of reinforcing elements are distinct from the underlying elements and are defined separately. For three dimensional continuum elements, either a single reinforcement bar or a layer of reinforcements may be defined. Besides the material properties, the cross-sectional area of each reinforcing bar, spacing between them, orientation of the reinforcing bars within the element, isoparametric direction and distance of reinforcement from the relevant element edges are defined (ABAQUS/Standard, 1994b).

The formulation of reinforcing bars in continuum (three dimensional solid) elements is presented. The volume of integration at a Gauss point is (ABAQUS, Theory 1995):

$$\Delta V = \frac{A_r}{S_r} \left| \frac{\partial \mathbf{X}}{\partial r_1} \times \frac{\partial \mathbf{X}}{\partial r_2} \right| W_N \quad (4.25)$$

where r_i is the isoparametric coordinates of the surface of reinforcement, A_r is the cross sectional area of each reinforcing element, S_r is the spacing between them, W_N is the Gauss weighting associated with the integration point, \mathbf{X} is the position of the Gauss point and

$$\frac{\partial X_i}{\partial r_m} = \frac{\partial X_i}{\partial g_j} \frac{\partial g_j}{\partial r_m} \quad (4.26)$$

where g_j is the isoparametric coordinates of the basic finite element. In above expressions, all quantities are taken in reference configuration, therefore changes in the cross sectional area of the reinforcing elements or spacing between them are ignored in large strain analysis.

The strain in the reinforcing elements is

$$\epsilon = \frac{1}{2} \ln \left(\frac{g}{G} \right) \quad (4.27)$$

where

$$\begin{aligned} g &= dL^2 \\ G &= dL_0^2 \end{aligned} \quad (4.28)$$

s being a material coordinate that measures the distance along the rebar in current configuration and t being the isoparametric coordinate along the rebar,

$$ds = \sqrt{g} dt \quad (4.29)$$

The first variation of strain is

$$\delta \epsilon = \frac{\partial X_i}{\partial s} \frac{\partial \delta u_i}{\partial s} \quad (4.30)$$

and the second variation is

$$d\delta\varepsilon = \frac{\partial\delta u_i}{\partial s} \frac{\partial du_i}{\partial s} - 2 \frac{\partial\delta u_i}{\partial s} \frac{\partial x_i}{\partial s} \frac{\partial x_j}{\partial s} \frac{\partial du_j}{\partial s} \quad (4.31)$$

By using the material constitutive law, stresses may be expressed in terms of strains and the virtual work expression for a rebar element, similar to Equation 4.8 may be obtained, which in discretized form resembles Equation 4.17. Since the forms of these equations depend on constitutive law of the material in concern, they are not derived here.

4.3.4 Unidirectional Fibrous Composite Material Modeling in MARC: Rebar Elements

In MARC, rebar elements are isoparametric empty blocks which contain reinforcing bars (modeling the carcass in case of tires) running in certain pattern (MARC, 1994a and MARC, 1997b). The reinforcing bars have axial stiffness and are represented as layers with equivalent thickness(es) through the height of the element. The rebar elements are used in conjunction with a compatible element which models the matrix (rubber in case of tires) with the same connectivity. In MARC K6.2, the rebar elements are quadratic elements with midnodes whereas in versions K7.1 and K7.2, the linear ones are added as well.

\mathbf{X} being the position of a material point in reference configuration, and \mathbf{x} being the position vector of the same point in deformed configuration, \mathbf{u} being the displacement of material point from initial position to the final position, the Green-Lagrange strain tensor in terms of displacements is

$$E_{ij} = \frac{1}{2} \left(\frac{\partial u_i}{\partial X_j} + \frac{\partial u_j}{\partial X_i} + \frac{\partial u_m}{\partial X_i} \frac{\partial u_m}{\partial X_j} \right) \quad (4.33)$$

The right Cauchy-Green deformation tensor is

$$C_{ij} = \frac{\partial x_m}{\partial X_i} \frac{\partial x_m}{\partial X_j} \quad (4.34)$$

The orientation of reinforcing cords is denoted by the unit vector \mathbf{a} . The axial stretch of the cord λ_a is then

$$\lambda_a^2 = C_{ij} a_i a_j \quad (4.35)$$

The axial Green-Lagrange strain of the cord is then

$$E_a = \frac{1}{2} (\lambda_a^2 - 1) \quad (4.36)$$

The weak formulation of one dimensional reinforcing cord is therefore

$$\Pi(\mathbf{u}_i, \partial \mathbf{u}_i) = \int_V S_a \partial E_a dV - W_{\text{ext}} \quad (4.37)$$

where S_a is the axial second Piola-Kichoff stress on the cord, \mathbf{u} is the displacement vector, V is the volume of cords and W_{ext} is the virtual work of external forces. For the one dimensional reinforcing cord, the lateral stresses are zero and the lateral stretches depend only on the axial stretch λ_a as

$$\lambda = \sqrt{\frac{\det(\mathbf{F})}{\lambda_a}} \quad (4.38)$$

which implies that S_a is a function of λ_a only.

Incremental linearization of weak formulation yields

$$\Delta \Pi(\mathbf{u}_i, \partial \mathbf{u}_i) = \int_V \left(\frac{dS_a}{dE_a} \Delta E_a \partial E_a + S_a \Delta \partial E_a \right) dV \quad (4.39)$$

where dS_a/dE_a may be interpreted as the effective Young's modulus of the cord at that increment.

The planar and axisymmetric rebar elements have 2 Gauss integration points per reinforcement layer whereas three-dimensional ones have four points per layer. Typical axisymmetric rebar element configurations used in MARC are shown in Figure 4.2 and typical three-dimensional ones are presented in Figure 4.3.

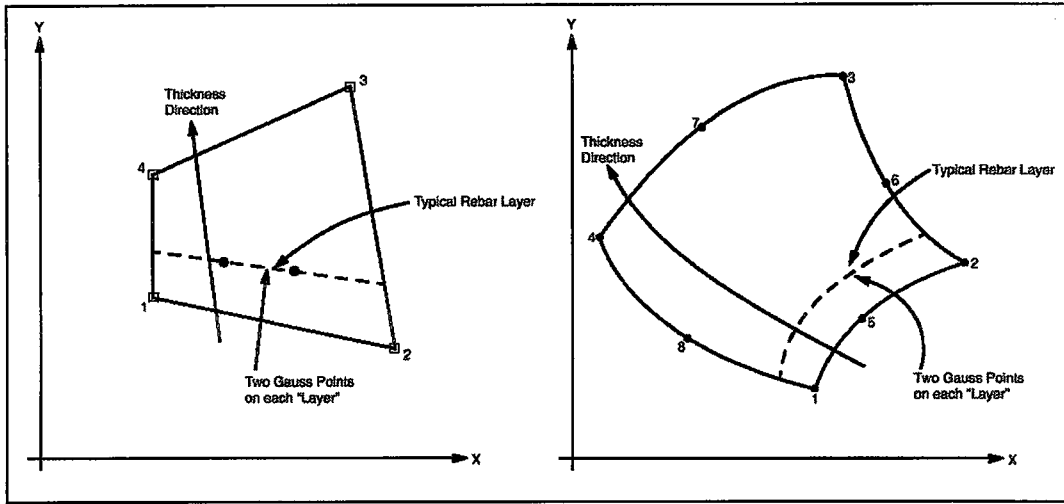


Figure 4.2 Axisymmetric, Linear and Quadratic Rebar Elements in MARC

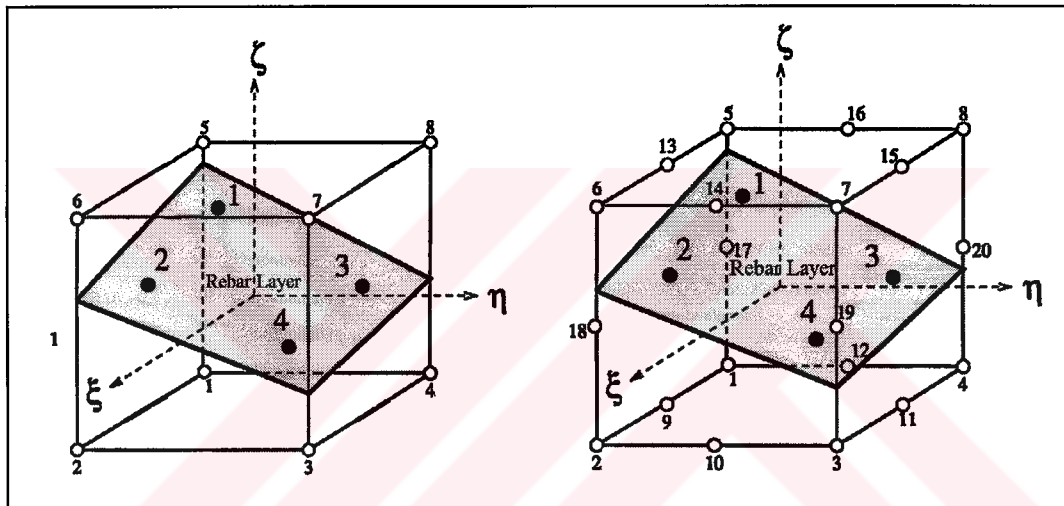


Figure 4.3 Three Dimensional, Linear and Quadratic Rebar Elements in MARC

The Green-Lagrange strain at a typical integration point is

$$E_{ij} = \frac{1}{2}(C_{ij} - \delta_{ij}) \quad (4.40)$$

and its variation

$$\delta E_{ij} = \frac{1}{2} \delta C_{ij} = B_{ijm} \delta \bar{u}_m \quad (4.41)$$

where \mathbf{B} is the standard beta matrix in finite element implementation of total Lagrangian formulation for large deformation and $\bar{\mathbf{u}}$ is the nodal displacement vector. \mathbf{B} can be decomposed as

$$\mathbf{B}_{ijm} = \mathbf{B}_{ijm}^L + \mathbf{B}_{ijm}^{NL} = \mathbf{B}_{ijm}^L + \bar{u}_n \mathbf{B}_{ikn}^{L1} \mathbf{B}_{jkm}^{L2} \quad (4.42)$$

where \mathbf{B}^L is the linear part and \mathbf{B}^{NL} is the nonlinear part of beta matrix. \mathbf{B}^{L1} and \mathbf{B}^{L2} are two linear operators similar to \mathbf{B}^L .

$$\delta E_a = \frac{1}{2} a_i a_j \delta C_{ij} = a_i a_j \delta E_{ij} = a_i a_j \mathbf{B}_{ijm} \delta \bar{u}_m \quad (4.43)$$

Linearization yields

$$\Delta \delta E_a = a_i a_j \mathbf{B}_{ikn}^{L1} \mathbf{B}_{jkm}^{L2} \Delta \bar{u}_n \delta \bar{u}_m \quad (4.44)$$

Therefore, the elemental stiffness matrix and internal force vector of a rebar element in MARC are

$$\mathbf{K}_{mn} = \int_{V^e} \left(\frac{dS_a}{dE_a} (\mathbf{B}_A)_m (\mathbf{B}_A)_n + S_a a_i a_j \mathbf{B}_{ikn}^{L1} \mathbf{B}_{jkm}^{L2} \right) dV^e \quad (4.45)$$

$$\mathbf{F}_m^{int} = \int_{V^e} S_a (\mathbf{B}_A)_m dV^e \quad (4.46)$$

where

$$(\mathbf{B}_A)_m = a_i a_j \mathbf{B}_{ijm} \quad (4.47)$$

The above formulation requires the components of the unit tangent vector of rebar element at each integration point, the equivalent thickness of reinforcement along the thickness direction (the ratio of total area of reinforcing members to element length, which may be interpreted as the uniform equivalent thickness), the hollow element thickness and position of reinforcing layer with respect to element thickness, which are supplied by the user subroutine *REBAR* of the MARC program. The material properties and number of rebar layers are supplied by the model input file.

The axisymmetric quadratic rebar element (element 48) is an eight-node quadrilateral in which user may place single strain members. It is normally used in conjunction with an eight-node axisymmetric continuum element. It is assumed that several layers of rebar are present and the number is determined by the user. Each layer is similar to 1-2 direction of the element although the direction of the

reinforcing cords are arbitrary. On each layer, two Gauss integration points are used. The axial strain along the rebar is defined as

$$\varepsilon = \frac{\partial u_i}{\partial x_j} a_i a_j + \frac{u_R}{R} a_\theta a_\theta + \frac{1}{2} \left(\frac{\partial u_i}{\partial x_j} a_j \frac{\partial u_i}{\partial x_k} a_k + \frac{u_R}{R} a_\theta \frac{u_R}{R} a_\theta \right) \quad (4.48)$$

where i, j, k are summed over the range 1 to 2 (corresponding to z and r) and a_i are the direction cosines of the reinforcing bars in the global coordinates. The linear version of this element is included in version K7, which is element number 144. Element number 145 is similar to 144 but it considers torsional strains in the axisymmetric structure as well.

The three dimensional quadratic rebar element (element 23) is an isoparametric three dimensional empty block which contains reinforcing bars running in certain patterns. This element is normally used in conjunction with 20-node brick element which represents the matrix (rubber in case of tires). A maximum of five layers may be used for each element and each layer contains four Gauss integration points. The first layer is the one closest to the 1-2-3-4 face of the element. The linear version of this element, element number 146 is included in version K7 of MARC.

In MARC, by the user subroutine REBAR, which is accessed during each incremental step for every integration point in an element, the current position of the reinforcing elements are controlled. For large strain analysis, the difference between initial and final cross sectional area of the reinforcing fibers may be considered by adding the appropriate coding to the user subroutine as well. Some rebar subroutines used in research are presented in Appendix A.

4.3.5. Further Enhancements to Rebar Concept, Record Elements

The local mechanics (birdcaging in compression, which is termed as microbuckling as well) including the effect of twist and number of strands are

modeled by new reinforcing cord (record) elements. The nonlinear coupling between the extensional and twist behavior is modeled too. This model is proposed for commercial finite element codes by Padovan and associates (1998).

4.4 Nonlinear Elasticity and Nearly Incompressible Behavior of Rubber

4.4.1 Introductory Definitions

Rubber, the matrix material of tire does not exhibit linear stress-strain relation like Hookean materials and its force-deflection behavior even in uniaxial tension deviates substantially from a straight line which characterizes rubber as a highly nonlinear material. Furthermore nonreinforced rubber can be strained up to 1000 %.

In uniaxial tension, the stretch ratio (or simply stretch) is defined as the ratio of current length of the specimen to the initial length of it as

$$\lambda = \frac{L}{L_0} \quad (4.49)$$

or substituting

$$L = L_0 + u \quad (4.50)$$

where u is displacement,

$$\lambda = 1 + \frac{u}{L_0} \quad (4.51)$$

In large deformation analysis, Green-Lagrange strain is used, which is for uniaxial case

$$E = \frac{1}{2}(\lambda^2 - 1) \quad (4.52)$$

with its work conjugate being second Piola-Kirchoff stress S for incompressible case is

$$S = \frac{F}{A} \left(\frac{L_0}{L} \right)^2 \quad (4.53)$$

For the general three-dimensional loading, the stress invariants which are functions of stretch ratios are

$$\begin{aligned} I_1 &= \lambda_1^2 + \lambda_2^2 + \lambda_3^2 \\ I_2 &= \lambda_1^2 \lambda_2^2 + \lambda_2^2 \lambda_3^2 + \lambda_3^2 \lambda_1^2 \\ I_3 &= \lambda_1^2 \lambda_2^2 \lambda_3^2 \end{aligned} \quad (4.54)$$

For perfectly incompressible materials, $I_3=1$.

4.4.2 Time-Independent Nonlinear Elasticity of Rubber

Rubber is a polymer and it consists of long chains of simple (monomeric) molecules with all elements of each chain linked tightly together. If there were no cross links between the various chains, they could slide over each other. This would permit permanent (plastic) deformations to occur which can be observed in rubber before vulcanization. Due to the existence of cross links, after a certain amount of sliding, the cross links will be stressed and the sliding motion is stopped. The molecular chains of a polymer are not static but they are in continuous thermal motion and have a tendency to get curled up. This tendency causes the two neighboring chains to come as close as possible which is the reason that causes the vulcanized rubber to have a preferred (definite) shape.

For gradually increasing deformation, the stress will increase gradually but as the molecules get farther apart, they can show less resistance to deformation and there is a decreasing tendency in stress, until the chains start approaching fully extended position where stress starts to increase very sharply which is followed by braking of the chains which leads to macroscopic fracture (MARC, 1984a, Osswald, 1996).

Further details of microscopic deformation mechanics of rubber is out of scope of this thesis and, macroscopic behavior of rubber deformation will be examined beyond this point by phenomenological considerations.

Using the arguments of statistical mechanics and thermodynamics, it is possible to approximate Helmholtz free energy roughly (which reduces to elastic strain energy under constant temperature) with the condition of incompressibility.

Definition of stress invariants and the third invariant being identically unity for incompressible isotropic (in initial configuration) materials results the strain energy function to be defined purely in terms of the two strain invariants as

$$W = W(I_1, I_2) \quad (4.55)$$

There exist a number of nonlinear constitutive models for rubber in the literature. Most of the proposed material models are characterized by different forms of their strain energy (density) functions. For a linear elastic material, the strain energy function takes the form

$$W = \frac{1}{2} L_{ijmn} E_{ij} E_{mn} \quad (4.56)$$

where L_{ijmn} are the 21 independent elastic constants for the most general linear anisotropic elastic medium and \mathbf{E} is the Green-Lagrange strain tensor. The components of Cauchy stress tensor and material elasticity tangent are obtained by

$$\begin{aligned} \sigma_{ij} &= \frac{\partial W}{\partial E_{ij}} = 2 \frac{\partial W}{\partial C_{ij}} \\ D_{ijkl} &= \frac{\partial^2 W}{\partial E_{ij} \partial E_{kl}} = 4 \frac{\partial^2 W}{\partial C_{ij} \partial C_{kl}} \end{aligned} \quad (4.57)$$

for the hyperelastic materials.

For rubber undergoing large deformations, Equation 4.56 cannot model the actual behavior. The simplest model for rubber elasticity is the Neo-Hookeian model represented as

$$W = C_{10}(I_1 - 3) \quad (4.58)$$

which exhibits a constant shear modulus and good correlation with the experimental data up to 40% strain in uniaxial tension and up to 90% strains in simple shear.

The earliest material model for the nonlinear elasticity of rubber, by Mooney is

$$W = C_{10}(I_1 - 3) + C_{01}(I_2 - 3) \quad (4.59)$$

which shows good agreement with tensile test data up to 250 % strains as well as stiffening behavior in compression. This model fails to account for stiffening of the material at large tensile strains (Osswald, 1996, MARC, 1996, MARC, 1997a). Comparison of theoretical and experimental stress-stretch curve for extension in Figure 4.4 (Osswald, 1996) reveals that Mooney-Rivlin material model approximates the elastic behavior of rubber up to a stretch of 3.5. This figure verifies that error introduced by assuming linear elastic behavior for rubber in stretches not exceeding 1.5 is rather small.

Some improvements on the model proposed by Mooney are all known as Mooney-Rivlin material models. To name some of them, the three term Mooney-Rivlin model is

$$W = C_{10}(I_1 - 3) + C_{01}(I_2 - 3) + C_{11}(I_1 - 3)(I_2 - 3) \quad (4.60)$$

Signiorini model,

$$W = C_{10}(I_1 - 3) + C_{01}(I_2 - 3) + C_{20}(I_1 - 3)^2 \quad (4.61)$$

Third order invariant

$$W = C_{10}(I_1 - 3) + C_{01}(I_2 - 3) + C_{11}(I_1 - 3)(I_2 - 3) + C_{20}(I_1 - 3)^2 \quad (4.62)$$

Third order deformation or also known as James-Green-Simpson

$$W = C_{10}(I_1 - 3) + C_{01}(I_2 - 3) + C_{11}(I_1 - 3)(I_2 - 3) + C_{20}(I_1 - 3)^2 + C_{30}(I_1 - 3)^3 \quad (4.63)$$

and the Yeoh model which depends only on first strain invariant

$$W = C_{10}(I_1 - 3) + C_{20}(I_1 - 3)^2 + C_{30}(I_1 - 3)^3 \quad (4.64)$$

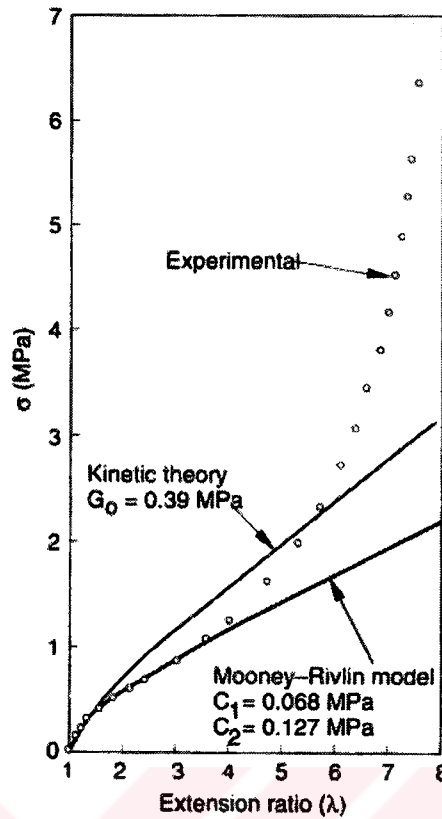


Figure 4.4 Theoretical and Experimental Stress Stretch Curve for Natural Rubber (Osswald, 1996)

The most general form of strain energy function proposed by Ogden in terms of principal stretches is

$$W = \sum_{n=1}^N \frac{\mu_n}{\alpha_n} J^{-\frac{\alpha_n}{3}} (\lambda_1^{\alpha_n} + \lambda_2^{\alpha_n} + \lambda_3^{\alpha_n} - 3) + 4.5K \left(J^{\frac{1}{3}} - 1 \right)^2 \quad (4.65)$$

from which Neo-Hookean and Mooney-Rivlin models can be recovered as special cases. In Ogden model, μ_n and α_n are the material constants determined by curve fitting to experimental data and K is the bulk modulus of the material. Ogden model yields good results up to 700% strain but requires careful and precise determination of the constants. Mooney-Rivlin models assume the material to be incompressible whereas Ogden model considers some compressibility by the inclusion of the bulk modulus of the material into the model.

Determination of stresses from the strain energy function and incompressibility constraint may be performed in two ways. In the first method, one (or two in case of axisymmetric problems) of the stretch ratios may be eliminated by using the incompressibility condition (and eventually symmetry) and the stresses in the remaining directions may be determined by the differentiation of the strain energy with respect to stretch ratios. The second method is adding the incompressibility constraint as a Lagrange multiplier and the value of the multiplier is determined later with the condition of prescribed stress on one or more surfaces. It should be mentioned that, for an incompressible material, the stresses cannot be determined if only stretch ratios are known, due to the fact commonly termed as “hydrostatic pressure” which causes no strain in the material.

Tire, having a reinforcing carcass in it, is exposed strains less than 40% under normal service conditions therefore in most tire models in literature, if not a linear elastic approximation is used, Mooney material model is preferred. The two coefficients of Mooney model may be obtained by simple tension test. The test specimen has 2 mm thickness and the shape and dimension of the specimen is shown in Figure 4.5. The measurement temperature is room temperature (20°C), crosshead speed is 5.08 mm/min and the coefficients of the two-term model can be obtained by

$$P = 2A_0 \left(1 - \frac{1}{\lambda_1^3} \right) (\lambda_1 C_{10} + C_{01}) \quad (4.66)$$

and deformation state is evaluated by

$$\lambda_1 = \frac{L}{L_0} \quad (4.67)$$

$$\lambda_2 = \lambda_3 = \left(\frac{J}{\lambda_1} \right)^{\frac{1}{2}} \quad \text{with } J \cong 1$$

therefore the plot of reduced stress $[P/2A_0(\lambda_1 - 1/\lambda_1^2)]$ versus $1/\lambda$ usually referred as a Mooney Plot yields a straight line with slope C_{01} and y-intercept C_{10} .

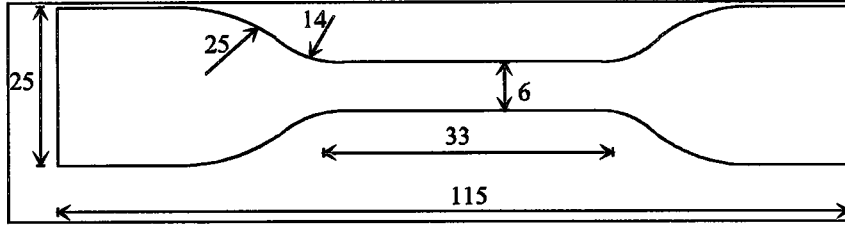


Figure 4.5 ASTM Tension Test Specimen (Dimensions in mm, Thickness 2 mm)

4.4.3. Herrmann Formulation for Incompressible and Nearly Incompressible Material Representation in Finite Element Programs

The nearly incompressible and incompressible material representations including various types of Mooney and Ogden material models require the use of an augmented variational principle based on the Herrmann (1965) formulation.

The instantaneous material behavior is assumed to be isotropic and elastic. The total Green-Lagrange strain is then;

$$E_{ij} = E_{ij}^{el} + E_{ij}^{nel} \quad (4.68)$$

where superscript el refers to elastic strain components and nel refers to nonelastic ones like creep, thermal or plastic. The elastic constitutive theory is

$$S_{ij} = 2G(E_{ij}^{el} + \nu H\delta_{ij}) \quad (4.69)$$

where S is the second Piola-Kirchoff stress, G is the shear modulus ν is the Poisson's ratio (very close or equal to 0.5) and H is the Herrmann mean pressure variable defined as

$$H = \frac{\sigma_{kk}}{2G(1 + \nu)} \quad (4.70)$$

The equilibrium equation is

$$\frac{\partial \sigma_{ij}}{\partial x_j} + q_i = 0 \quad (4.71)$$

where σ is the Cauchy stress and q is the body force per unit volume. The dilatation relation is

$$E_{kk}^{el} - (1 - 2\nu)H = 0 \quad (4.72)$$

Introducing the virtual displacement field $\delta \mathbf{u}$ on the equilibrium equation and a variation on the dilatation relation $2\nu G\delta H$, the augmented virtual work equation is

$$\int_v \left(\frac{\partial \sigma_{ij}}{\partial x_j} + q_i \right) \delta u_i dv - \int_v (E_{kk} - E_{kk}^{nel} - (1 - 2\nu)H) 2\nu G\delta H dV = 0 \quad (4.73)$$

where v is the current volume and V is the initial volume occupied.

Applying Gauss theorem with surface tractions as

$$t_i = \sigma_{ij} n_j \quad (4.74)$$

yields

$$\begin{aligned} \int_v (S_{ij} \delta E_{ij} + (E_{kk} - (1 - 2\nu)H) 2\nu G\delta H) dV = \\ \int_s T_i \delta u_i dS + \int_v Q_i \delta u_i dV + \int_{V^0} E_{kk}^{nel} 2\nu G\delta H dV \end{aligned} \quad (4.75)$$

where

$$\delta E_{ij} = \frac{1}{2} (\delta u_{i,j} + \delta u_{j,i} + u_{k,i} \delta u_{k,j} + \delta u_{k,i} u_{k,j}) \quad (4.76)$$

is the first variation of Green-Lagrange strain.

The elastic constitutive theory substituted into the equation yields

$$\begin{aligned} \int_v 2G (\delta E_{ij} E_{ij} + \nu H \delta E_{kk} + \nu E_{kk} \delta H - \nu (1 - 2\nu) H \delta H) dV = \\ \int_s T_i \delta u_i dS + \int_v Q_i \delta u_i dV + \int_v 2G (E_{ij}^{nel} \delta E_{ij} + \nu E_{kk}^{nel} \delta H) dV \end{aligned} \quad (4.77)$$

which includes large displacement and large strain effects and is to be solved incrementally by the program. Taylor series expansion of the equation and neglecting the higher order displacement terms yields equations linear in terms of displacements. The incremental form of augmented variational principle is then

$$\begin{Bmatrix} \Delta S_{11} \\ \Delta S_{22} \\ \Delta S_{33} \\ \Delta S_{12} \\ \Delta S_{23} \\ \Delta S_{31} \\ \Delta I \end{Bmatrix} = \begin{bmatrix} 1 & 0 & 0 & 0 & 0 & 0 & \nu \\ 0 & 1 & 0 & 0 & 0 & 0 & \nu \\ 0 & 0 & 1 & 0 & 0 & 0 & \nu \\ 0 & 0 & 0 & 0.5 & 0 & 0 & 0 \\ 0 & 0 & 0 & 0 & 0.5 & 0 & 0 \\ 0 & 0 & 0 & 0 & 0 & 0.5 & 0 \\ \nu & \nu & \nu & 0 & 0 & 0 & -\nu(1-2\nu) \end{bmatrix} \begin{Bmatrix} \Delta E_{11} \\ \Delta E_{22} \\ \Delta E_{33} \\ \Delta E_{12} \\ \Delta E_{23} \\ \Delta E_{31} \\ \Delta H \end{Bmatrix} \quad (4.78)$$

where the strain increments are

$$\Delta E_{ij} = \Delta u_{i,j} + \Delta u_{j,i} + u_{k,i} \Delta u_{k,j} + u_{k,j} \Delta u_{k,i} \quad (4.79)$$

and ΔI is the increment of dilatation restraint force. The dilatation restraint force is expressed as

$$I = \int_V 2G(\delta E_{ij} E_{ij} + \nu H \delta E_{kk} + \nu E_{kk} \delta H - \nu(1-2\nu) H \delta H) dV \quad (4.80)$$

The temperature dependent material behavior may be included in the above formulation as well.

4.5 Contact and Friction Models in Finite Element Programs

4.5.1 Deformable to Rigid Body Contact Model in ABAQUS

In ABAQUS although *CONTACT PAIR/*CONTACT SURFACE option exists for automatic handling of contact, the special purpose contact elements (stress/displacement rigid surface elements) to model the contact between a rigid body and three dimensional continuum elements are utilized. The element used in static tire contact analysis is a five node element (IRS4) in combination with a Bézier surface. The element shares the four nodes on the free surface of the linear brick element and the fifth node, which is a control node is on the rigid surface, to which the deformable body will contact. The active degrees-of-freedom at surface nodes are only three orthogonal translations and the fifth control node has rotational degrees of freedom too. Distance of a node to the

rigid surface is measured by the outward normal of the rigid surface passing through that node. In case the distance is negative, a nonlinear contact force is applied to the node so that it is within the prescribed tolerance to the rigid surface.

4.5.2 Coulomb Friction Model in ABAQUS

The equivalent frictional stress is evaluated by

$$\tau_{\text{fric}} = \sqrt{\tau_1^2 + \tau_2^2} \quad (4.81)$$

where τ_i are the frictional stresses in the principal sliding directions. Using Coulomb friction model, no relative motion is possible with

$$\tau_{\text{fric}} \leq \tau_{\text{crit}} = \mu p \quad (4.82)$$

In ABAQUS, it is possible to put a limit on the critical stress shear stress as

$$\tau_{\text{crit}} = \min(\mu p, \tau_{\text{max}}) \quad (4.83)$$

where τ_{max} is the flow stress of the material specified by the user. This limit is intended for more realistic metal forming simulations and may be useful in modeling the tire behavior in a locked wheel.

4.5.3 Deformable to Rigid Body Contact Model in MARC

In MARC, a variable boundary condition method is used to model the contact with rigid surfaces. When a node touches to a rigid surface, a local transformation of coordinates is made into a tangential and a normal direction to the rigid surface. The displacement of the node in normal direction is equal to the rigid surface displacement in the same direction as imposed as a boundary condition.

The basic algorithm of MARC rigid contact may be summarized as follows:

1. At the start of an increment, all nodes that are candidates to contact nodes are checked for the rigid surface(s) and flagged if so.
2. Transformations and imposed displacements are determined for each node that touches to a rigid surface. The rigid body segment to which a node is touching is checked.
3. One increment of the problem is solved iteratively and values for displacement increments are calculated. Step 2 is repeated at each iteration for possible changes in rigid body segments.
4. After the solution has converged, the nodal forces at the contact nodes are checked. For tensile nodal contact forces, the node is released from contact surface and step 3 is repeated.
5. All free boundaries are checked for contact. If any free node is in contact with a rigid surface, the increment size is reduced such that only one new node touches to rigid surface and the process is restarted at step 3.
6. If fixed increment size is specified, the current increment is split into two.
7. Step 1 is returned.

The above stated basic contact algorithm is enhanced by advanced techniques to improve the performance of the program especially in large problems with complex shaped and/or a large number of rigid bodies (MARC, 1984b).

4.5.4 Friction Models in MARC

The Coulomb friction force is modeled by fictitious nonlinear springs in MARC as

$$F_t = -\mu F_n \frac{2}{\pi} \operatorname{atan}\left(\frac{v_r}{C}\right) \quad (4.84)$$

and the friction stress is modeled by

$$\sigma_t = -\mu\sigma_n \frac{2}{\pi} \operatorname{atan}\left(\frac{v_r}{C}\right) \quad (4.85)$$

where, F_n is the normal contact force, σ_n is the normal contact stress, μ is the coefficient of friction, v_r is the relative sliding velocity and C is the relative sliding velocity below which sticking is simulated. Coulomb friction may be based on nodal forces or nodal stresses whereas shear friction can only be based on nodal stresses which are related to the yield stress of the material. It is suggested that C is selected in between 1 to 10 percent of relative sliding velocity. C being too small causes bad convergence due to very sharp change in frictional force at very low relative sliding velocities whereas being too large causes the effect of friction to diminish for practical sliding velocities. For various values of C , the relative friction force versus sliding velocity is plotted in Figure 4.6. For other types of friction models, the friction law may be defined by user subroutine. The most general form of the friction law is then;

$$\mu = \mu(\mathbf{x}, f_n, T, v_r, \sigma_y) \quad (4.86)$$

where \mathbf{x} is the position of the point where friction is calculated, f_n is the normal force at the point, T is the temperature at the point, v_r is the relative sliding velocity at the point and σ_y is the flow stress of the material.

There are other friction models in MARC K7.2, among which the stick-slip friction model is particularly useful in tire models. In stick-slip model, instead of allowing small slips at low relative velocities, sticking condition with static coefficient of friction (which is different than sliding coefficient of friction) is simulated. Stick-slip friction model brings a more realistic friction model in return has increased solution time due to increased nonlinearity. α is the ratio of static to sliding coefficient of friction, β is the stick-to-slip transition tolerance ϵ is a small fixed value so that $\beta\epsilon \approx 0$ and e is the user defined friction force tolerance such that the ratio of friction force in present step to previous step cannot exceed as

$$1 - e < \frac{f_f^i}{f_f^{i-1}} < 1 + e \quad (4.87)$$

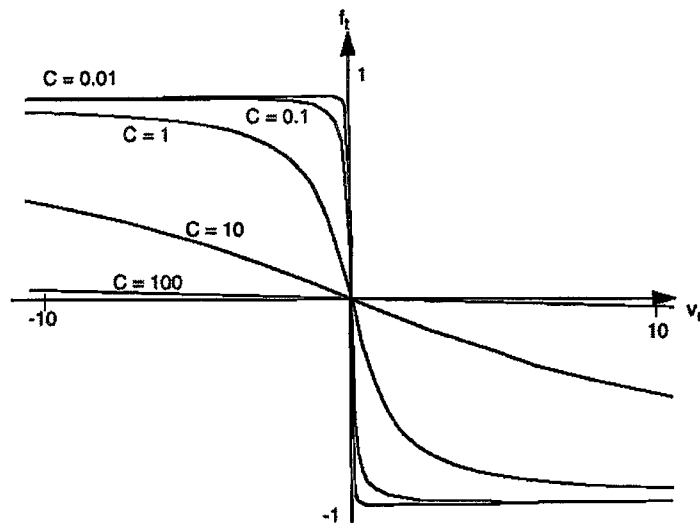


Figure 4.6 Regularized Coulomb Friction for Various C Values ($\mu=1$ and $F_n=1$)

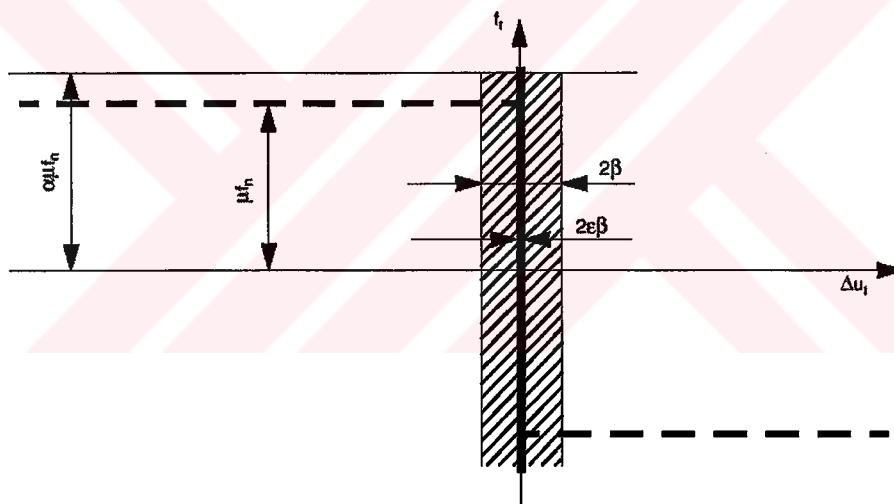


Figure 4.7 Stick-Slip Friction Model in MARC

In MARC, frictional forces are applied as distributed loads. The friction equations are implicit functions of the displacement increments therefore during the iterative solution procedure, they have contribution to the tangent stiffness matrix. For all elements that contain contact surfaces with friction, the stresses, temperature and flow stresses are extrapolated to the nodes. For each surface, the

nodal normal stresses, nodal relative sliding velocities are calculated and frictional force and stiffness contributions are numerically integrated using trapezoidal rule. The analysis starts with zero sliding velocity assumption and in each subsequent increment the relative sliding velocity of previous solution is used as a starting point (MARC, 1984b, 1997a).

4.6 Redefining a Mesh on Deformed Geometry

For large elastic-plastic deformations, updated Lagrange approach which considers the state at the beginning of the increment as the initial configuration is utilized. However, due to large deformations encountered, the finite element mesh may degenerate strongly which causes the results obtained be rather poor, or even some elements may locally turn inside out which makes the further analysis impossible. Redefining a mesh on deformed geometry idea which is termed as rezoning initiated from this necessity. The new mesh defines the same physical problem as the updated old mesh. The idea behind rezoning has three main steps.

1. Definition of a Continuous Field for All Variables:

For rezoning, a continuous field for all variables has to be formed. Among the existing procedures to construct such a field, the local smoothing with triangularization was shown to be the most suitable one (Gelten and Jong, 1984).

The three phases of this local smoothing

- a. Subdividing the local mesh into triangles (for two dimensional models) or tetrahedrons (for three dimensional models) and storing the connectivity of this subdivision. For quadrilateral and brick elements some extra nodal points need to be defined.
- b. The nodes in new mesh are determined in relation to triangles or tetrahedrons. The triangular coordinates are used for this purpose.

- c. Extrapolation of all element variables to nodal point variables by local smoothing technique which evaluates the mean of the nodal value of the elements connected to that node.

The averaging technique to define the field variables in the continuum assumes the continuum to be homogeneous. In case of tires with different layers of reinforcement, the reinforcement causes discontinuities which has a great impact on averaging. To obtain reliable results, rubber matrix having different elastic properties and textile and steel reinforcement must occupy different spatial locations. In physical tire, since these materials work together, proper multi-point constraints (tyings) must be defined among the different materials to achieve the real working conditions.

2. Definition of a New Mesh:

The new mesh should cover in principle the same area or volume as the old deformed mesh does. The new mesh may be completely different than the old mesh with regard to number of nodes, number of elements and element connectivity. User has to decide on the moment of rezoning and the new mesh.

3. Transferring the Field Variables to the New Mesh

The nodes in the new mesh are in a triangle or tetrahedron of the old mesh. The field variables of the new mesh are evaluated by using the triangular coordinates and linear interpolation. For the boundary nodes, however, the new node may be out of the triangle or tetrahedron due to curved boundaries. In this case, using the nearest triangle or tetrahedron, the field variables of the node is determined by linear extrapolation. The element variables are evaluated using the nodal values by either bi or tri-linear interpolation or by isoparametric interpolation.

Due to approximations involved in transferring the variables from old mesh to the new one, equilibrium may not be satisfied exactly after the first

loading step after rezoning. Therefore, it may be useful to perform a zero or very small load step right after rezoning.

4.7 Modeling Centrifugal Loads in Cornering Analysis

In quasi-static tire models, the centrifugal force due to rotation may be implemented as a distributed load by supplying the mass densities of the tire materials, rotation speed (independent of the time increment of the analysis) and the position of the rotation axis. The distributed body force is evaluated by

$$q_i = \rho \omega^2 r_i \quad (4.88)$$

where ρ is the mass density per unit deformed volume, ω is the angular speed of the body and r is the current position vector of the material point, perpendicular to the rotation axis, starting from rotation axis and pointing the material point. The finite element software evaluates consistent nodal loads of the elements depending on their volumes. The angular velocity of the body, ω is defined by the analyst and can be implemented to a static analysis as well.

CHAPTER 5

STATIC FINITE ELEMENT MODELING OF TIRE

5.1 Introduction

A static analysis is performed before going into the more complex cornering analysis of the rolling tire. The goal of the static analysis is twofold. The material data for the rubber-textile and rubber-steel composites are not precisely known, therefore the static analysis is an indicator for the adequacy of the assumptions for the calculation of the material elastic properties. Next, static analysis will reveal some basic problems in finite element modeling of tires. Since static model is simpler than cornering model, it will be simpler to tackle with the problems detailed in the previous Chapter.

A number of trials are performed initially with homogeneous tires (which are not presented here since the material of real tire is a highly anisotropic composite whose behavior is far off from that of a homogeneous tire), before inflation and contact analysis are performed on a composite tire. These trials revealed the proper mesh size especially for the contact analysis.

5.2 Tire Modeled

The tire model is based on geometry and construction of 155 R 13 78 S tire which is a typical small and medium sized automobile tire. The properties of the tire, taken from manufacturer's catalog are presented on Table 5.1.

Table 5.1 Properties of 155 R 13 78 S Tire

Recommended Rims	4.50 Bx13 or 5.00 Bx13
Inflated Section Width	157 mm
Inflated Outer Diameter	578 mm
Maximum Load per Tire	4220 N (430 kgf)
Maximum Inflation Pressure	220 kPa (32 psi)

5.3 Coarse Mesh Tire Model

5.3.1 Mesh

For the first trial using ABAQUS, the mesh generated consists of 24 elements per half sector. The sector mesh is shown in Figure 5.1. Since in static loading, the problem is symmetric -except tread ply which is skew-symmetric but this fact is ignored- only half of the tire sector is modeled with appropriate boundary conditions.

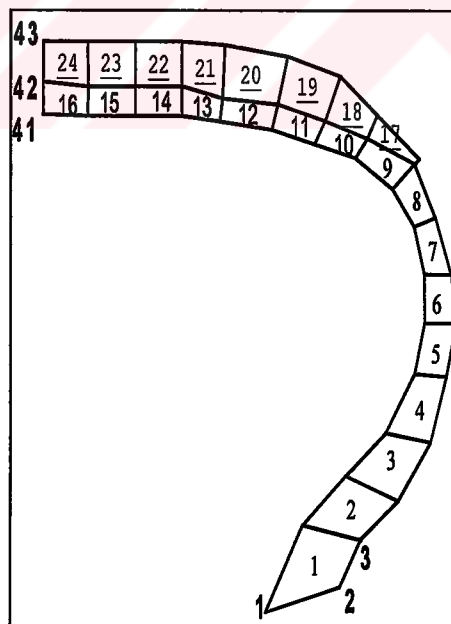


Figure 5.1 Profile of Coarse Finite Element Mesh Used

In this mesh, elements 1 to 9 are sidewall elements with the property of one ply of textile fibers embedded into the rubber. Although there exists a bead bundle made of steel in element 1, this construction is ignored for the time being, assuming that it does not affect the static behavior of the tire significantly. Also the body ply being wrapped around the bead bundle and bead filler are ignored and this section is assumed to contain single ply. Elements 10 to 16 are tread ply elements. Body ply continues in them as the inner ply and there exists two more steel plies over the body ply. These two steel plies are not perpendicular to body ply but mostly have about +20 and -20 degree angle with the meridional line. Each steel ply is 2 mm thick with four 0.25 mm diameter steel wires per 1.32 mm on the average. A schematic sketch of carcass construction is shown in Figure 5.2. Elements 17 to 24 are the tread elements made of rubber only. For the time being the tread pattern is ignored and the tread surface is assumed to be smooth. The boundary conditions on the sector are as follows:

Rim is assumed to be rigid and the tire is assumed to be stuck on it so nodes 1, 2 and 3 are fixed in all three mutually perpendicular directions.

In static loading, tire sector is symmetric, therefore symmetry boundary condition in the horizontal direction, the horizontal motion being prevented is applied to nodes 41, 42 and 43.

The tire is inflated to 180 kPa air pressure which is the rated pressure of this specific tire, also 165 kPa and 200 kPa are applied as well, which are 10 % less and 10 % more than the rated inflation pressure respectively. Pressure is applied to the appropriate nodes which lie on the inner surface of the tire as “element uniform pressure” boundary condition. In large deformation analysis, the pressure always remains perpendicular to the deformed element surface. A detailed treatment of pressure boundary condition including large displacements is in Chapter 4.

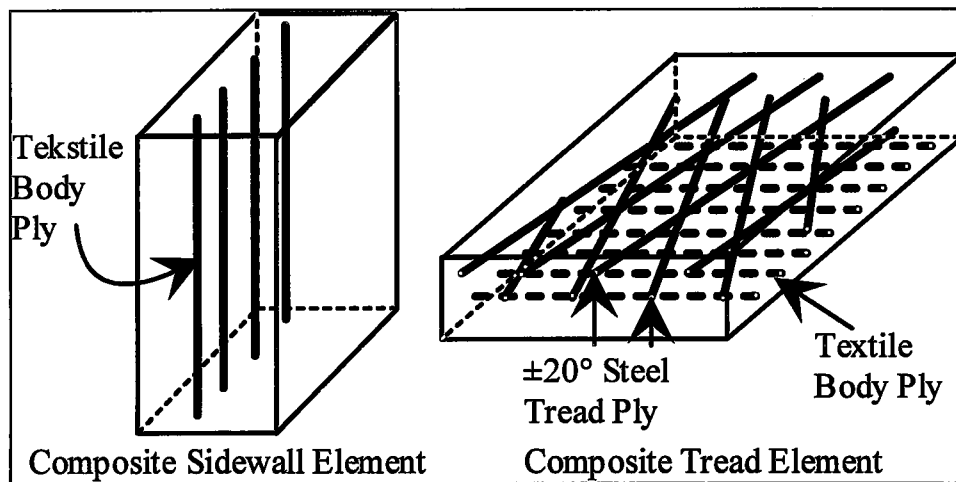


Figure 5.2 Carcass Construction of Steel Belted Radial Tire

Since the aim is not to perform inflation analysis but also the ground contact analysis of the tire, this axisymmetric model is not sufficient. The model has to be swept through 180 degrees. For the first 30 degrees, since contact is expected in this zone, 2 degrees increment is used for a finer mesh and in the remaining 150 degrees, 10 degrees increment is applied. The model thus obtained is shown in Figure 5.3. Since the model is symmetric, the mobility of end nodes in horizontal direction is restricted.

The textile fibers are modeled as linear elastic material in tension and not carrying compression loads by the command *NO COMPRESSION, steel fibers are modeled as linear elastic material, rubber is approximated by linear elastic model since the carcass prevents large strains, although Mooney-Rivlin material model may be introduced to increase the accuracy of the model. The material properties used are presented in Table 5.2.

5.3.2 Inflation Analysis

The first step in the static analysis of the tire is inflation. The rated pressure of the tire is 180 kPa. The deformations occurring on the computer

model are consistent with the deformations observed on similar type of physical tires.

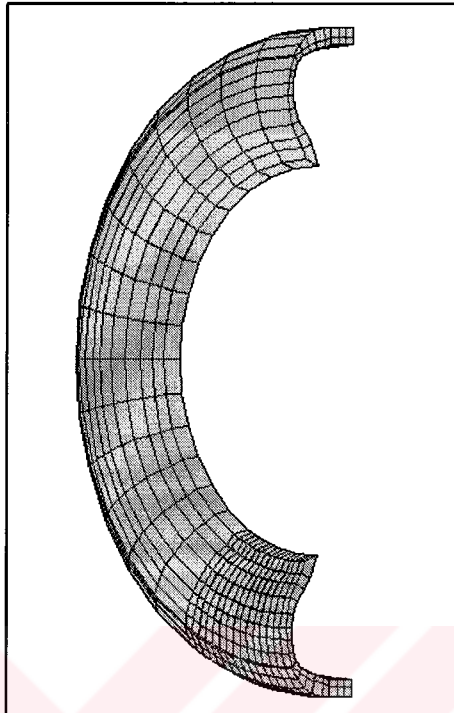


Figure 5.3 Coarse Mesh of Static Tire Model

Table 5.2 Material Properties

Tread		Sidewall		Textile Belts (Only in Tension)				Steel Belts ($\pm 20^\circ$)			
E	ν	E	ν	E	ν	Distance between Fibers	Area per Fiber	E	ν	Distance between Fibers	Area per Fiber
14 MPa	0.45	5.5 MPa	0.45	3.4 GPa	0.3	1.05 mm	0.126 mm ²	200 GPa	0.3	0.33 mm	0.126 mm ²

5.3.3 Ground Contact Analysis

The last step in static tire modeling is ground contact analysis. The inflated tire is pressed to a flat rigid surface having Coulomb friction, with coefficient of friction being 0.8. In ground contact analysis there exists two approaches in determining the boundary condition for ground contact; the displacement of the hub may be specified, or, the tire vertical load may be

specified. In ground contact analysis, the two very significant outputs for testing the model are, the pressure distribution in between tire and ground interface, and the vertical stiffness of the tire. The load-deflection characteristics of 155R13 steel belted radial is presented in Figure 5.4.

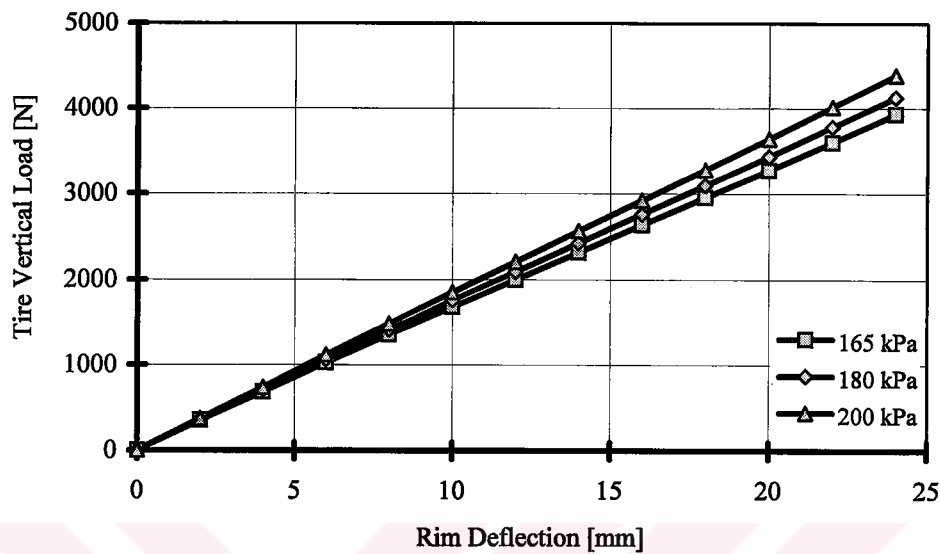


Figure 5.4 Load-Deflection Characteristics of 155 R 13 Tire with Modified Material Elastic Constants

If tread carcass ply is taken to be $\pm 10^\circ$, the vertical stiffness of the tire increases and carcass stiffness dominates over inflation pressure which decreases the dependency of vertical stiffness to inflation pressure as expected. Figure 5.5 presents the same tire with $\pm 10^\circ$ tread ply .

In case of textile belted radial tires, mostly there exists four plies of textile tread carcass instead of two plies of steel. The spacing of textile fibers is 1 per mm, with a fiber diameter of 0.5 mm. The ply angle is again $\pm 20^\circ$. Textile tread plies do not carry compression. Load deflection characteristics of this construction is presented in Figure 5.6 for different inflation pressures.

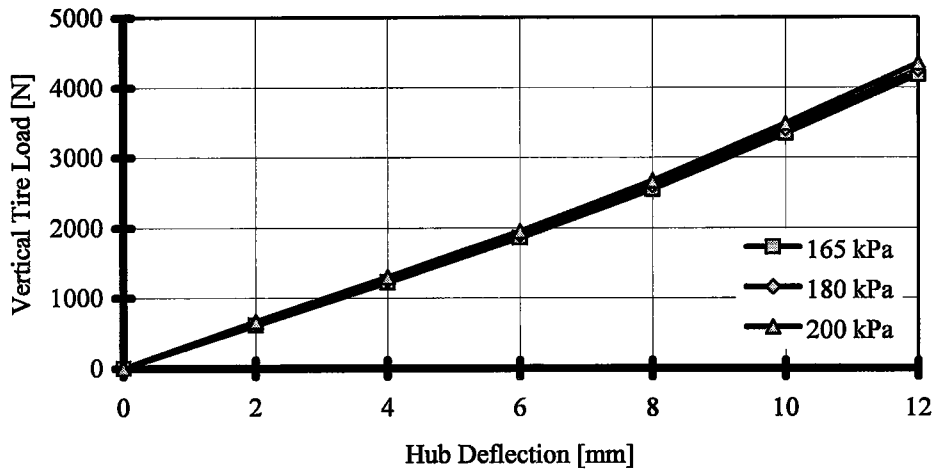


Figure 5.5 Load-Deflection Characteristics of 155 R 13 Tire with $\pm 10^\circ$ Tread Carcass

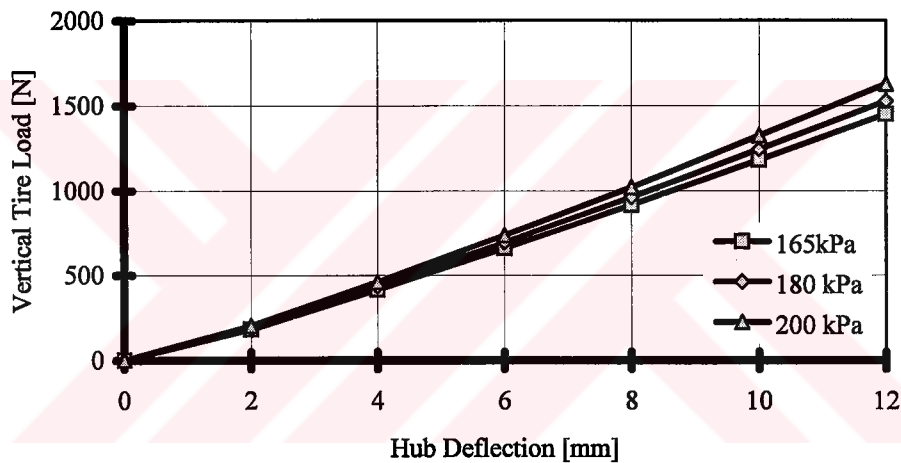


Figure 5.6 Load Deflection Characteristics of Textile Belted Radial Tire

Although 155 R 13 is a radial tire, if it were cross ply, with $\pm 35^\circ$ textile fibers, the load-deflection characteristics would be as shown in Figure 5.7. The cross ply tires are known to be structurally stiffer than radial tires thus they require lower inflation pressures than radial ones to maintain the same vertical load (Davis, 1997). The finite element model not being capable of modeling the rather pronounced pantographic action (interply friction) of ± 35 plies results unrealistic soft cross ply tire model.

The load deflection characteristics of $\pm 20^\circ$ and $\pm 10^\circ$ steel, $\pm 20^\circ$ textile belted radial tires, is compared with that of cross ply tire in Figure 5.8 for the rated inflation pressure 180 kPa.

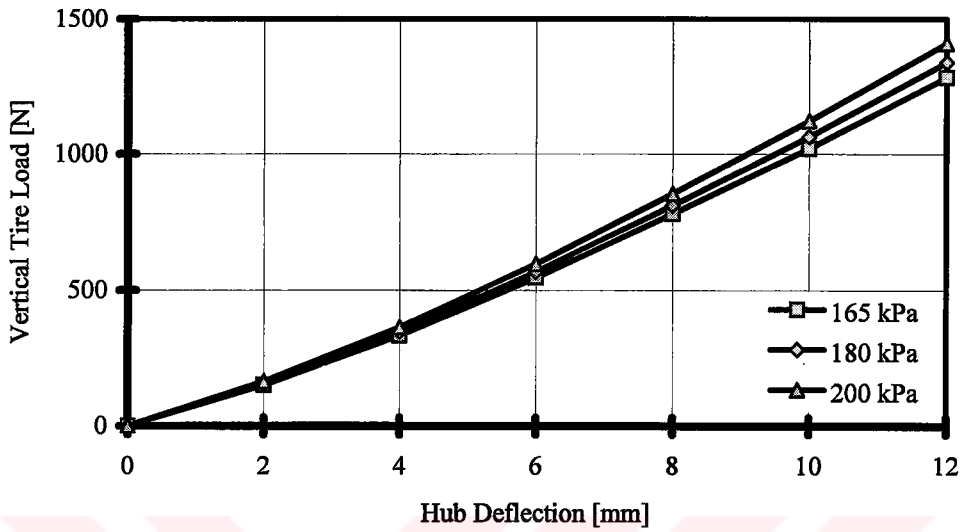


Figure 5.7 Load Deflection Characteristics of Cross Ply Tire

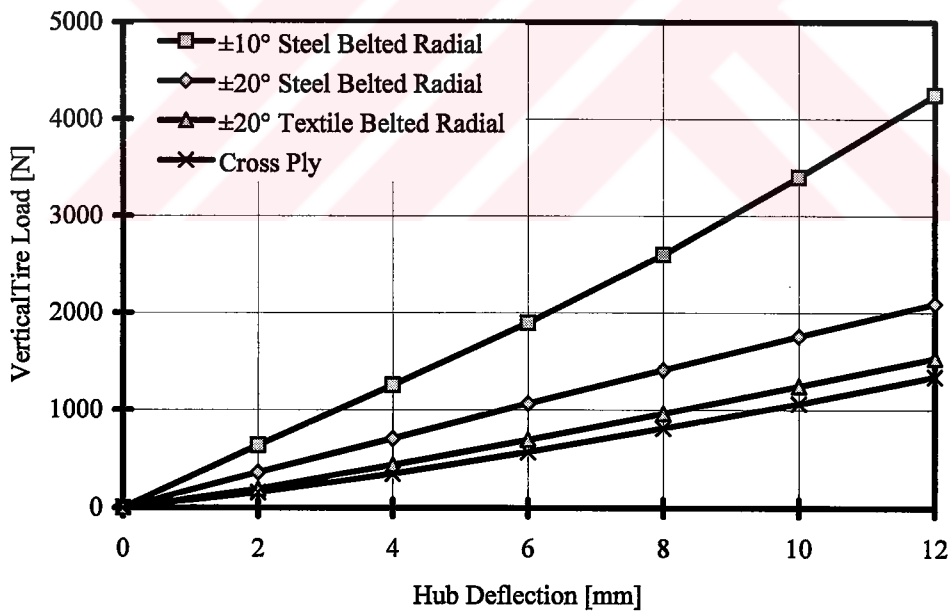


Figure 5.8 Comparison of Load Deflection Characteristics of Steel and Textile Belted Radial and Cross Ply Tires

The quarter-contact patch pressure distribution of the above analyzed four types of tires are presented in Figure 5.9. Vertical tire load is 2200 N, inflation pressure is 180 kPa. The contact patch pressure distribution being higher close to sidewalls and lower at the center of the contact patch resembles the pressure distribution obtained experimentally for a similar radial tire as shown in Figure 5.10.

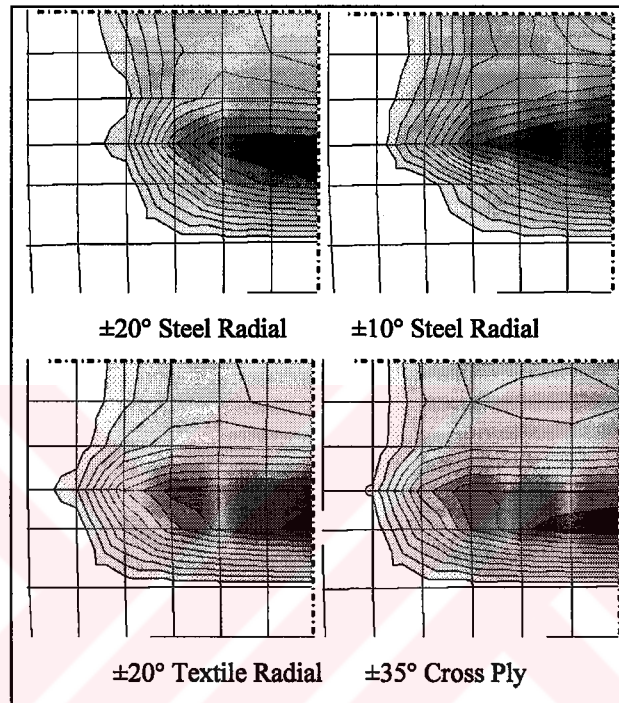


Figure 5.9 Contact Patch Pressure Distribution of Different Tire Constructions

5.3.4 Effect of Tire Tread to Contact Patch

The tire model presented so far has one major property missing, which is the tread pattern. Since the mesh is not fine enough to model the all tread geometry, only the circumferential grooves of the tread is modeled by removing the tread elements 21 and 24 (Figure 5.1) only in the contact patch zone. The model thus obtained may be thought of a rough model for modern tread geometry. The load deflection characteristics of such treaded, one textile body ply two steel tread plies 155R13 tire is presented in Figure 5.11 while a comparison of smooth

and treaded version of the same tire at rated inflation pressure is presented in Figure 5.12.

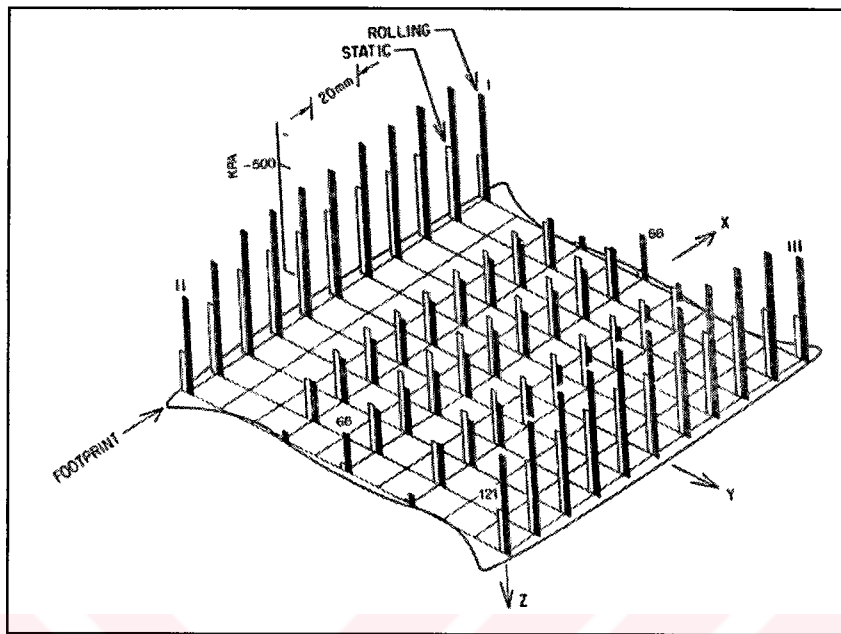


Figure 5.10 Contact Pressure Distribution of a 195/70R14 Tire in Static Case and in Low Speed Rolling (75 mm/s) by Pottinger (1992) Experimentally

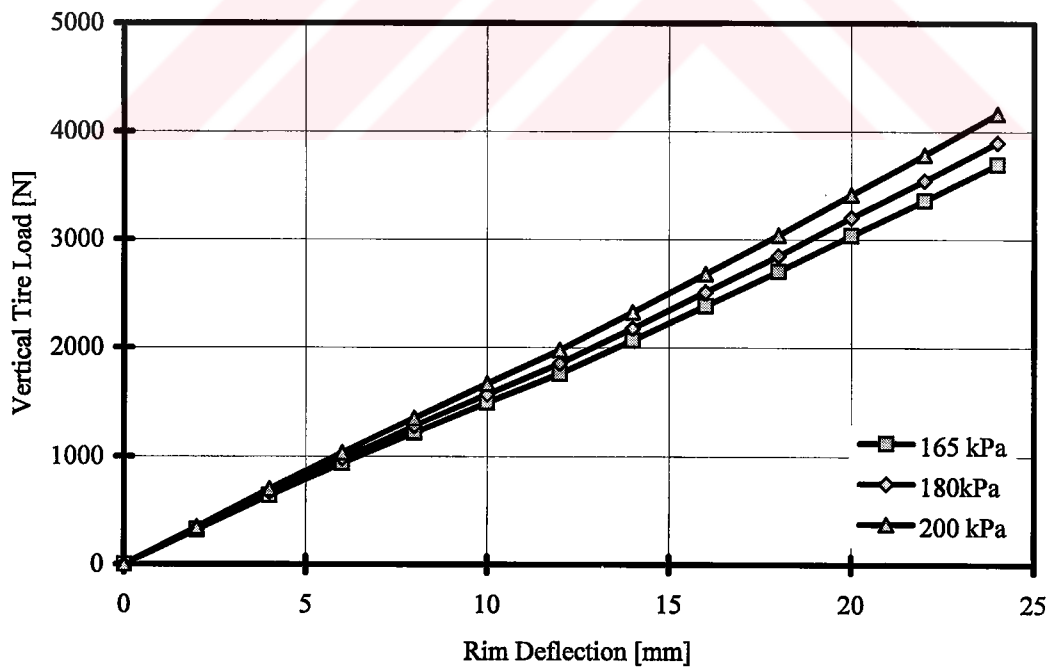


Figure 5.11 Load Deflection Characteristics of Treaded 155 R 13 Tire

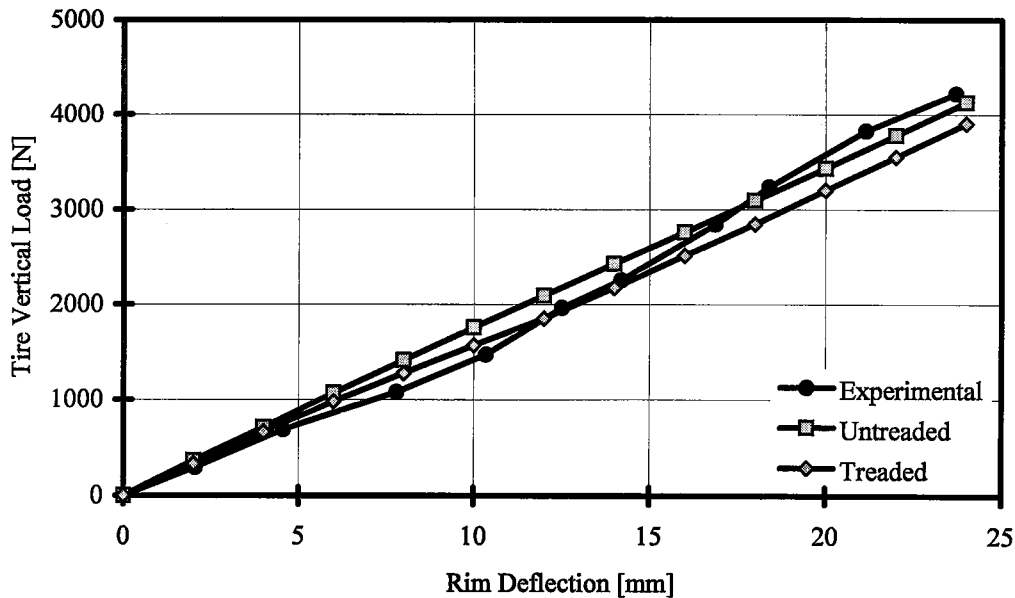


Figure 5.12 Comparison of Smooth and Treaded Tire Models with Experimental Data at 180 kPa Inflation Pressure

5.4 Fine Mesh Tire Model

5.4.1 Mesh

In the first mesh used, although computer time required to solve the model was not too high, it was evident that the mesh was coarse. In the contact region, a node entering into contact or separating caused severe changes in the results especially when only few nodes are in contact with the rigid surface. Furthermore, due to commonly known property of finite element analysis, having a finer mesh *mostly* improves the solution. Due to the stated two facts, a finer mesh with 41 elements per sector is formed, knowing that both the solution time and the computer resources needed to obtain the solution will be increased compared to that of coarse mesh. The tire sector with fine mesh is shown in Figure 5.13.

Elements 1 to 15 contain the body ply, elements 16 to 27 contain both body ply and tread ply and elements 28 to 41 are tread elements for a radial tire.

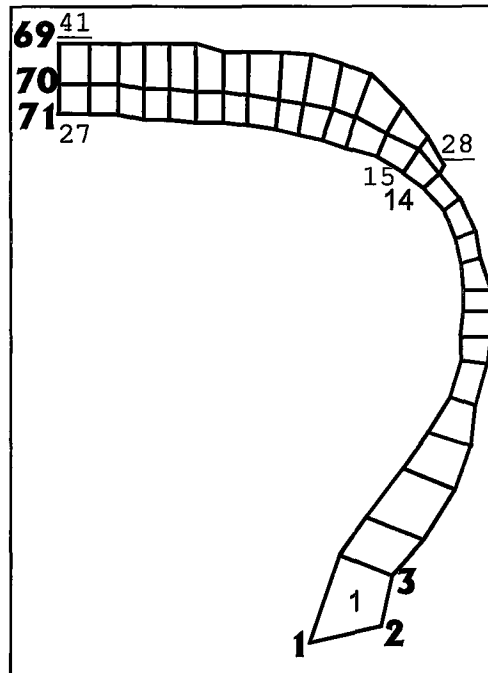


Figure 5.13 Profile of Fine Finite Element Mesh Used

In this mesh, the boundary conditions are as follows: Nodes 1, 2 and 3 fixed, modeling the rim, mobility of nodes 41, 42 and 43 is restricted in horizontal direction. Uniform pressure is applied to the inner surface to model the inflation.

For the region where one may expect contact, this profile is copied in angular direction with 1 degree increment 30 times, then in the remaining 150 degrees, a 5 degrees increment is applied. The tire model having 2460 8-noded brick solid elements and 4331 nodes belonging to those elements is presented in Figure 5.14.

The material elastic properties used for a steel belted radial tire is the same as in Table 5.3 and carcass construction is same as shown in Figure 5.2.

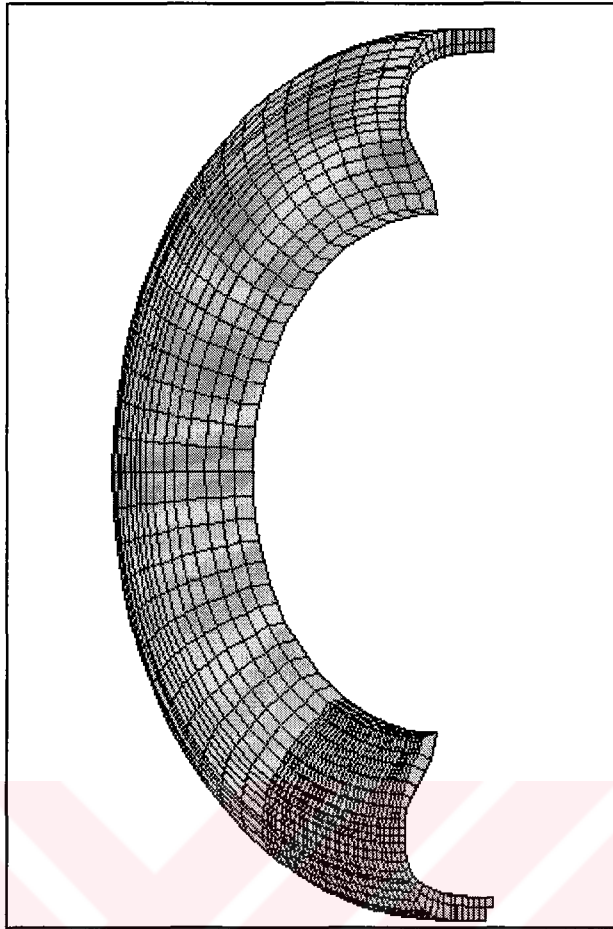


Figure 5.14 Finer Finite Element Mesh of Static Tire Model

5.4.2 Inflation Analysis

Inflation is the first step of the analysis. The tire is inflated to one of 165 kPa, 180 kPa 200 kPa which are 10 % less than rated pressure, rated pressure and 10 % more than rated pressure respectively. The deformations occurring on the computer model are consistent with the deformations observed on similar type of physical tires.

5.4.3 Ground Contact Analysis

The last step of static tire analysis is ground contact. The inflated tire is pressed to a rigid surface by a predefined displacement and ground reaction force

is measured. For 155 R 13 78 S tire with steel tread plies, the force displacement characteristics is presented in Figure 5.15 for three different inflation pressures. The force-displacement characteristics is similar to the one presented in Figure 5.4 except the finer mesh being slightly softer than the coarse mesh.

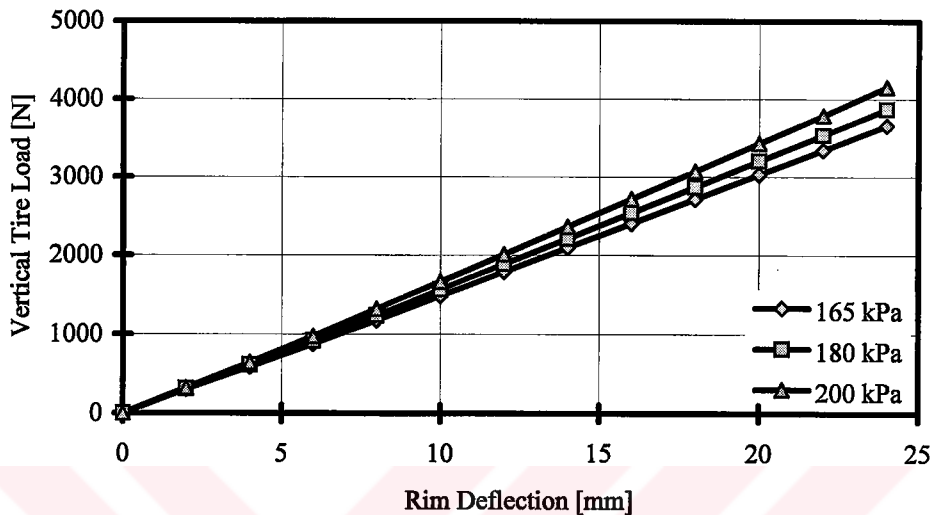


Figure 5.15 Load-Deflection Characteristics of 155 R 13 Tire with Finer Mesh

5.4.4 Effect of Tire Tread to Contact Patch

For the fine mesh, the tread geometry introduced may be improved compared to the coarse mesh. In addition to circumferential grooves, some staggered grooves connecting the circumferential grooves may be introduced by removing some more tread elements as in Figure 5.16. The load-deflection characteristics of such 155R13 tire is presented in Figure 5.17 while the comparison of smooth and treaded models of coarse and fine meshes with experimental data is presented in Figure 5.18.

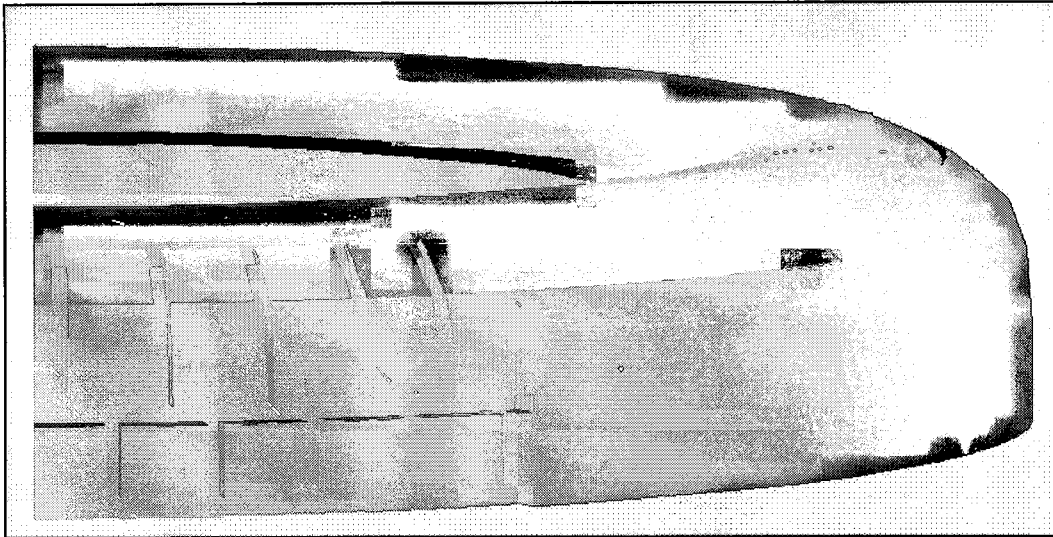


Figure 5.16 Simplified Tread Pattern Geometry Introduced to Contact Patch

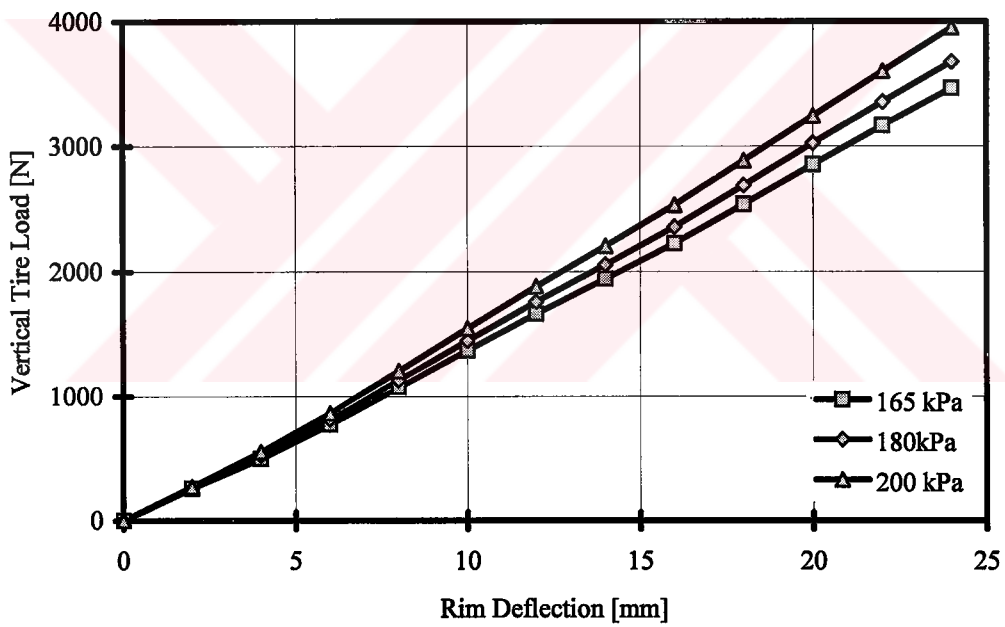


Figure 5.17 Load Deflection Characteristics of Treaded 155R13 Tire

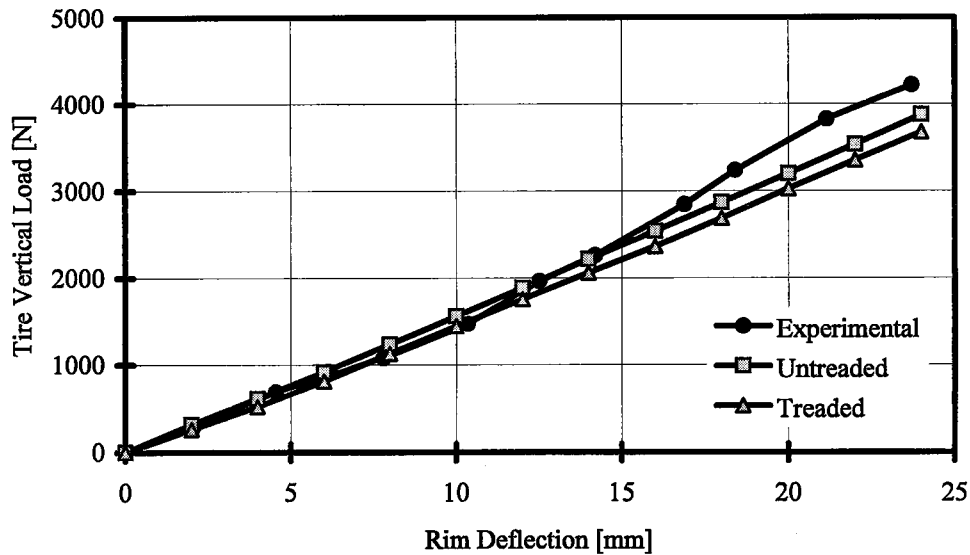


Figure 5.18 Comparison of Load Deflection Characteristics of Smooth and Treaded 155R13 with Experimental Data

5.5 Attempts for More Precise Models

The tire models presented so far have two major simplifications. The use of a linear elastic material model for the rubber, the main constituent of tire is the first major simplification. The second simplification is the use of the Poisson's ratio for rubber as 0.45, due to numerical solution scheme used, although most tire rubbers are nearly incompressible with Poisson's ratio being 0.49. With the increased computational power, Mooney-Rivlin material model, mostly preferred for polymers and incompressible formulation are introduced. The new models have refined mesh for more precise results. Quadratic elements are used in new models, instead of linear ones, which have second order interpolation functions.

5.5.1 Axisymmetric Inflation and Rim Seating Models

The axisymmetric tire model shown in Figure 5.19 consists of 198 8 node axisymmetric, incompressible (Herrmann formulation) elements modeling the rubber matrix. The material properties of various parts of the tire are presented in

Table 5.3 and the material identification of elements in Figure 5.20. The reinforcement of the tire are represented by 8 node rebar elements specially constructed for unidirectional reinforcing bars. The rebar elements have the same connectivity as the matrix element but has different material properties. The material properties of reinforcements are presented in Table 5.4, the distribution and ply angles are presented in Table 5.2, and the locations of these materials in mesh are shown in Figure 5.21.

Table 5.3 Mooney-Rivlin Material Constants of Rubber

Rubber Material	C_{10}	C_{01}
Bead Filler	14.14 MPa	21.26 MPa
Sidewall	171.8 kPa	830.3 kPa
Undertread	140.4 kPa	427 kPa
Tread	806.1 kPa	1.805 MPa

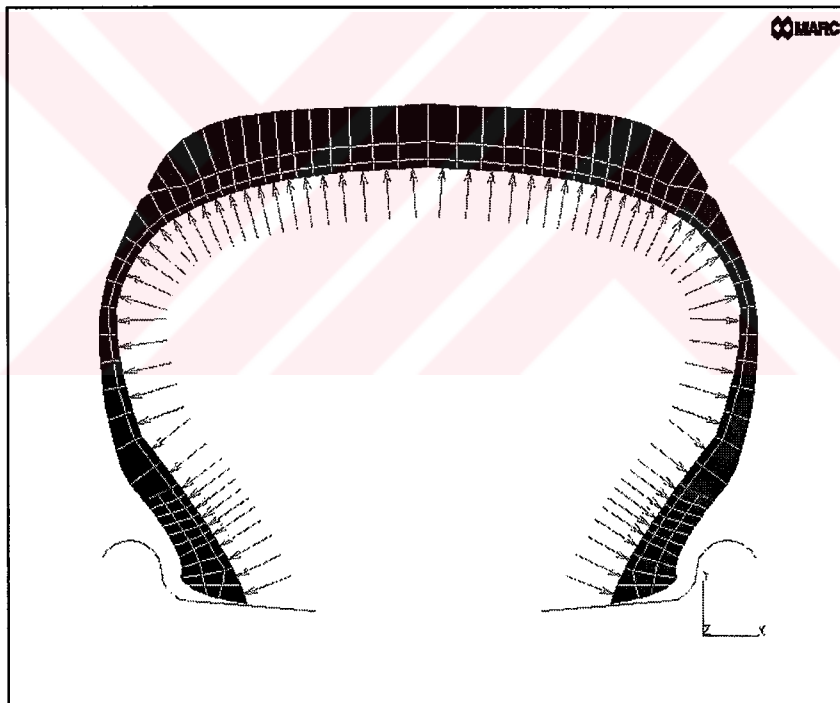


Figure 5.19 Axisymmetric Tire Model

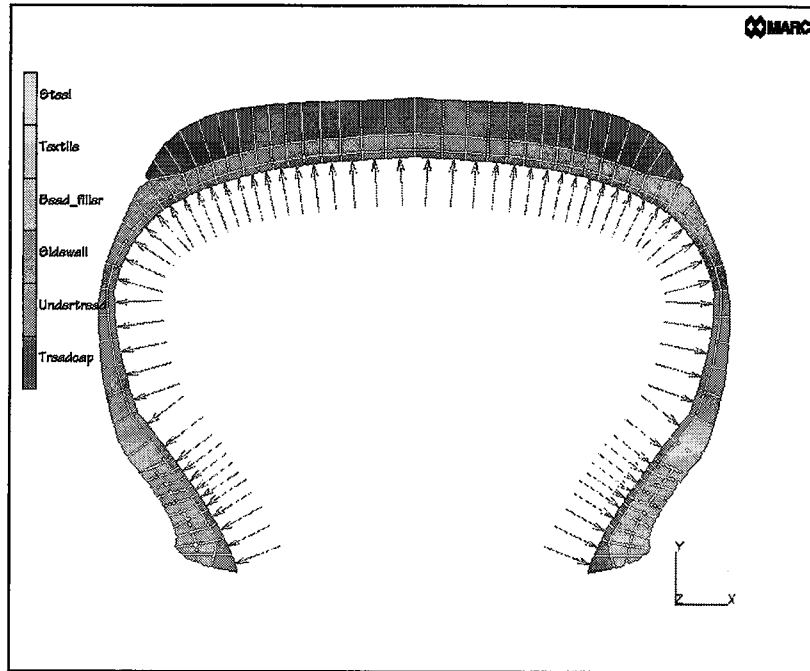


Figure 5.20 Location of Rubber Material in Tire

Table 5.4 Elastic Properties of Reinforcing Materials

Carcass Material	Modulus in Tension	Modulus in Compression
Textile Body Ply	3.97 GPa	198.5 MPa
Steel Breaker Plies	200 GPa	100 GPa

Table 5.5 Geometric Properties of Reinforcing Materials

Reinforcement Type	Ply Angle [°]	Cord Diameter [mm]	Ends per decimeter	Equivalent Thickness [mm]
Bead Bundle	0	1	Not applicable	Not applicable
Body Ply	90	0.68	79	0.120
Breaker (Steel)	±20	0.25	330	0.162
Breaker (Textile)	±20	1.0	112	0.878
Breaker (Zero)	0	0.68	100	0.363

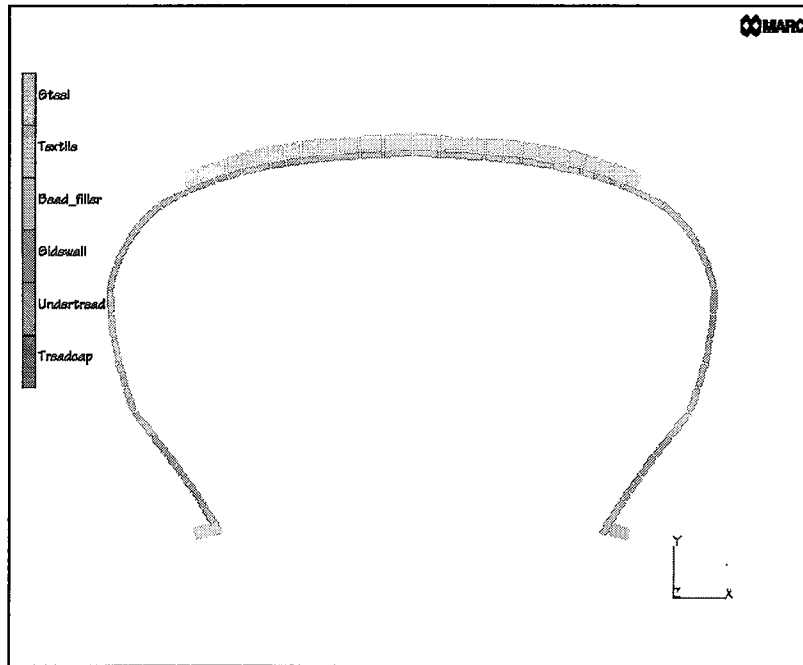


Figure 5.21 Location of Reinforcing Materials

The stresses due to inflation on different rims are analyzed. First, a 155R13 with one textile body ply and two steel tread plies is mounted on 4, 4.5, 5 and 5.5 inch rims where 4.5 and 5 are the recommended rims by the manufacturer while 4 and 5.5 inches are permitted as well. The stress distribution as well as tire profile are presented in Figure 5.22.

The same tire with 0° textile breaker ply added is mounted on 4.5 and 5 inch rims. The 0° ply reduces the stresses on breaker plies. The stress distribution and deformed shapes are presented in Figure 5.23.

Next, tire with 4 ply textile tread carcass is examined. The tire is mounted on 4.5 and 5 inch rims and inflated to rated pressure. Due to softened breaker plies, the stresses are reduced and deformations are increased. The stress distribution in the tire and deformed shapes of the tire are presented in Figure 5.24.

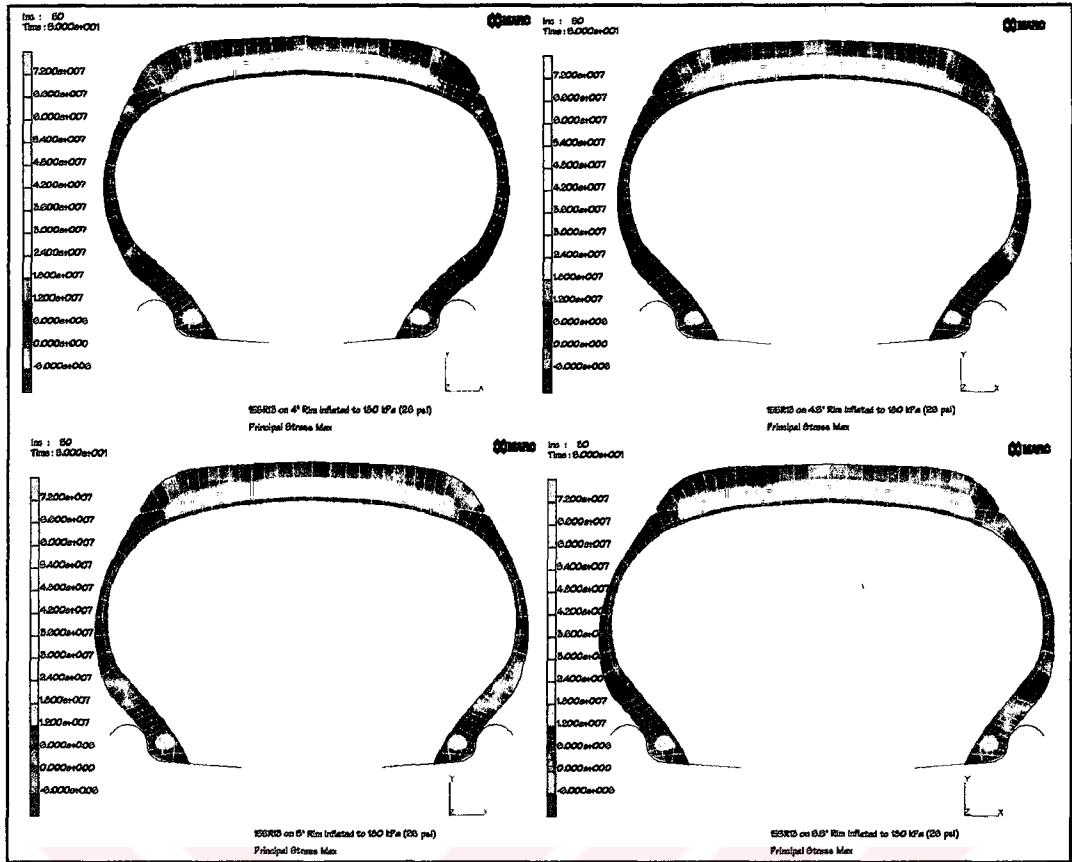


Figure 5.22 155R13 Tire Mounted on 4, 4.5, 5 and 5.5 inch Rims

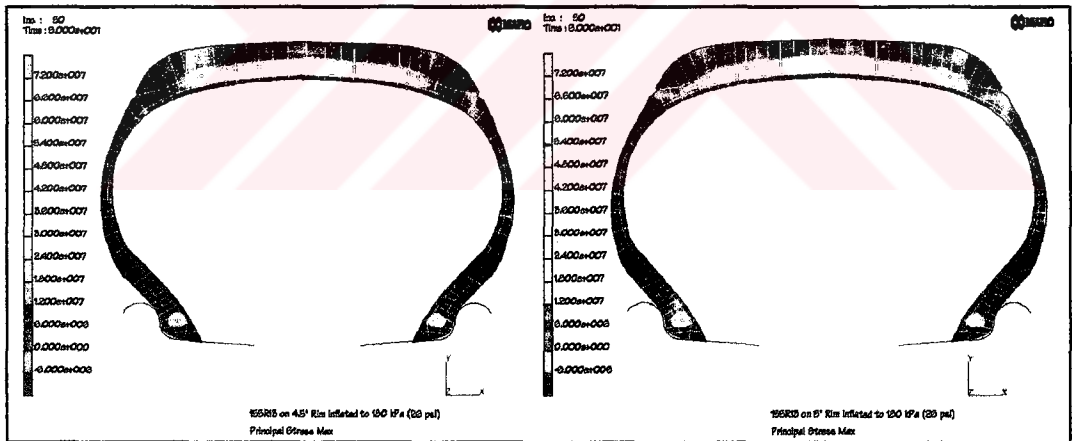


Figure 5.23 155R13 with 0° Textile Breaker Ply Added on 4.5 and 5 inch Rims

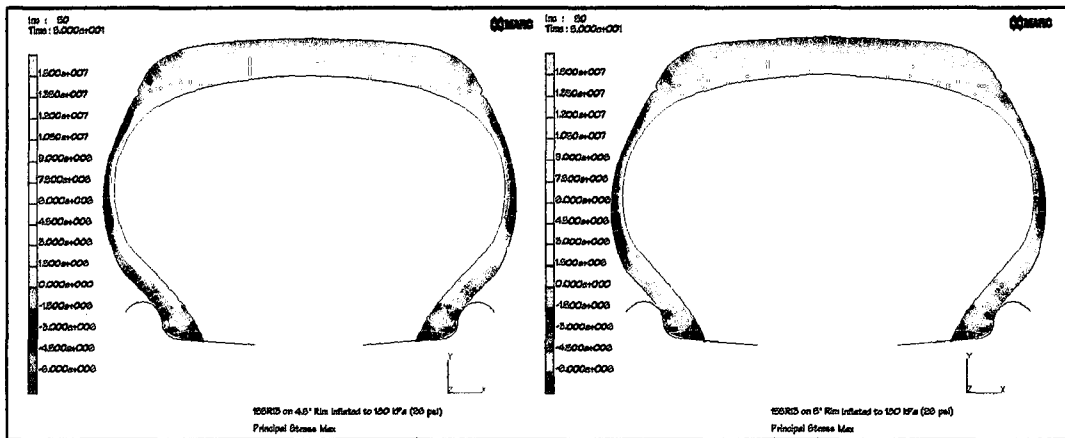


Figure 5.24 155R13 with 4 Textile Breaker Plies on 4.5 and 5 inch Rims

5.5.2 Ground Contact Model

In the first static model attempts, 8 noded brick elements were used which had trilinear interpolation functions. With increasing computational power, 20 noded brick elements were introduced. These elements have triquadratic interpolation functions which allows precise representation of strain fields. The incompressible elements using Herrmann formulation are introduced with Mooney-Rivlin (two coefficient) material model, which is specifically devised for polymers.

The tire mesh at the tire sector is similar to the axisymmetric model (Figure 5.19) but the skew-symmetry of breaker plies are ignored and symmetry boundary condition is applied to the symmetry plane. The rim contact is simplified by fixed boundary conditions therefore the finer mesh around rim contact zone is unnecessary and bead bundle is ignored. The resulting tire sector and quarter tire model are presented in Figure 5.25 and 5.26 respectively. The material properties and distribution are same as in Tables 5.3 and 5.4 and in Figures 5.22 and 5.23 respectively.

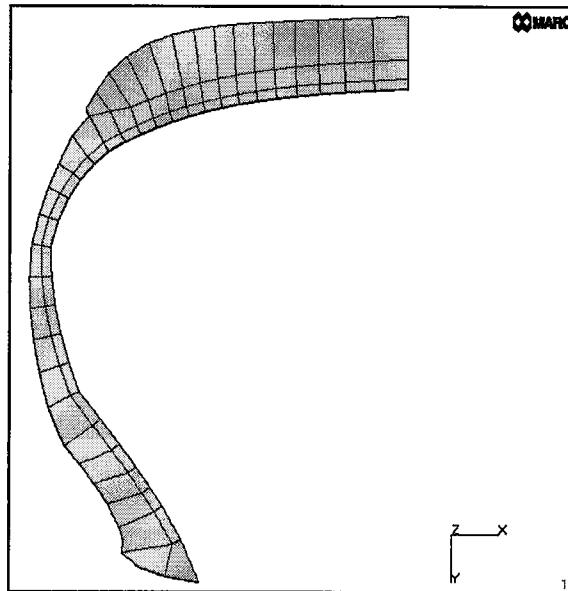


Figure 5.25 Tire Sector for Ground Contact Analysis

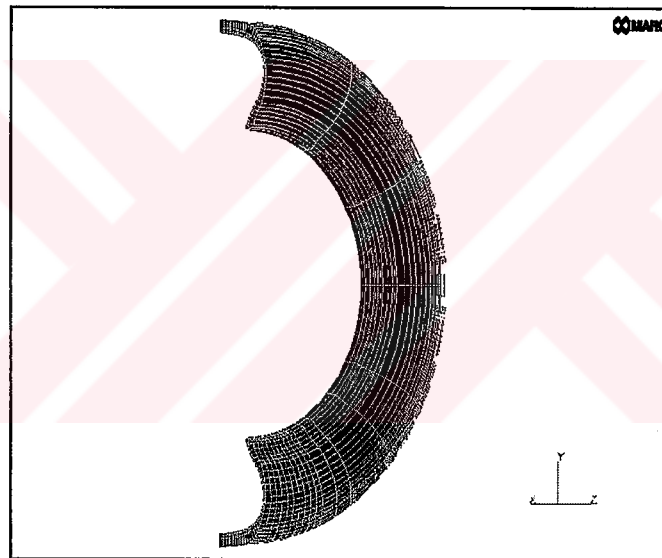


Figure 5.26 Quarter Tire Model for Ground Contact Analysis

The tire model presented in Figure 5.26 consists of 7922 nodes and 2448 elements. Since all tests -static or dynamic- are performed on the tire testing setup more precise than ever, the new tire model is pressed on a cylinder having the radius equal to that of the test machine drum. Due to refined mesh, simplified tread pattern of the tire can be modeled in a more realistic manner as shown in

Figure 5.27. Figure 5.28 shows the force-deflection characteristics of the treaded and smooth tire models compared with the experimental tire with 3 mm tread depth.

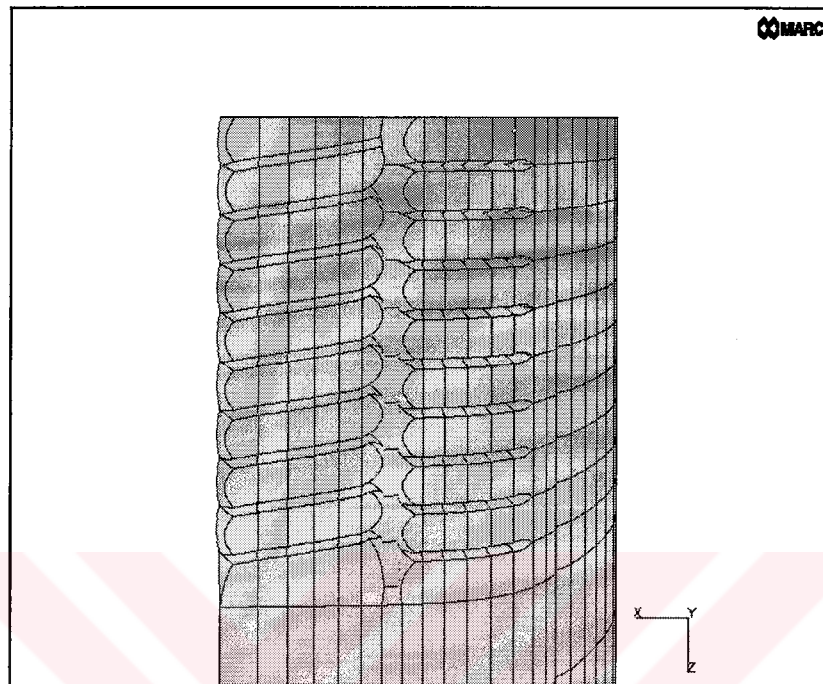


Figure 5.27 Simplified Tread Pattern

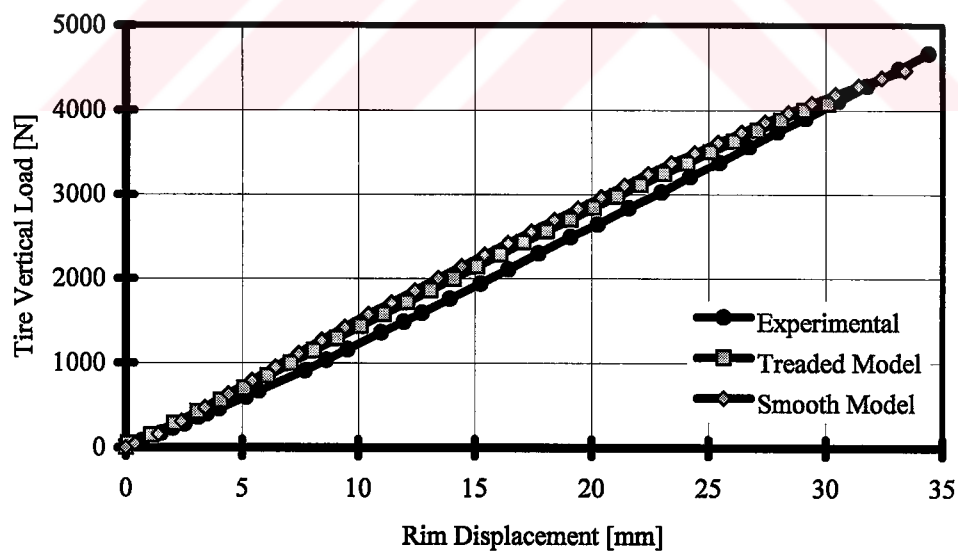


Figure 5.28 Force-Deflection Characteristics on the Drum of the Test Machine

5. 6. Conclusions about Static Tire Models

The results of static finite element tire models are in good agreement with the results from the experimental study and by other researchers. This can be accepted as a verification of the elastic material properties, carcass modeling, and mesh used in the model study. Furthermore, pressure distribution at the contact patch closely resembles the contact patch pressure distributions found in literature. These verifications form the basis for entering the next stage of the study, namely the modeling and analysis of cornering tire.



CHAPTER 6

MODELING THE CORNERING BEHAVIOR OF TIRE

6.1 Introduction

The goal of this study is to obtain the cornering force characteristics of the tire without any experimental data about the tire itself, if possible. To achieve this, starting with simplest computer model, neglecting inertia and viscoelastic effects, a model similar to the one used in static tire model will be used. Due to rolling and nonzero slip angle (diagonal motion), the symmetry assumption in static model is lost even in the simplest model.

After tuning the quasistatic model up, the enhancements like dynamic effects and viscoelasticity, may be introduced to the model. The amount of details introduced increases the precision of the model in the expense of computational time.

6.2 Remeshing Using MARC's Rezoning Capability

MARC can redefine the mesh on a deformed geometry as explained in Section 4.6. This leads to the idea of having fine mesh around the contact patch and coarse mesh elsewhere. As the tire rotates, the fine mesh zone would start moving away the contact patch and coarse mesh zone would come closer. Before coarse mesh enters to the zone where stress and strain gradients are high due to contact, using rezoning, the fine mesh zone would be moved such that the regions moving away from the contact zone would have coarse mesh and the regions

approaching to contact zone would have fine mesh. This approach would reduce the number of nodes and elements considerably without reducing the solution accuracy noticeably. However, as explained in Section 4.6, in order to use rezoning, the finite element software defines continuous field variables in the solution domain. For better approximation of discrete field variables in the continuous domain, any type of discontinuity must be avoided in the solution domain. MARC (1984b) strongly recommends using different spatial positions at the points of discontinuity, and use of proper tying, so that the structure works together. This is necessary because averaging of field variables are done spatially. In this case, with ultimate simplifications, 155R13 tire can be modeled as in three parts, rubber matrix, textile body ply, and steel tread plies occupying different spatial locations as shown in Figure 6.1. Each node on the body or tread ply, is connected to its rubber counterpart by tyings. This model contains many tyings which are created by a special program. However, number of tyings being so large increases the solution time beyond a fine mesh model. Further, each rezoning requires repositioning of nodes and regenerating the large number of tyings again. In this case, rezoning is not an alternative to complete fine meshing the contact trajectory. Therefore, in this study rezoning capability of MARC is not used except for some trials to check its applicability to the problem.

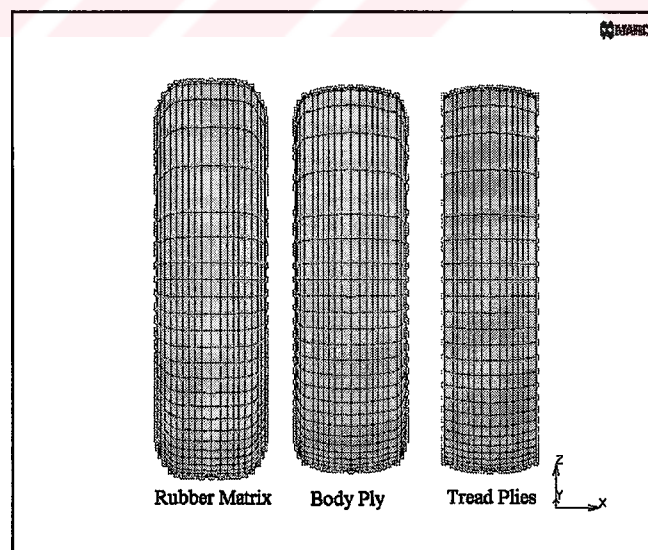


Figure 6.1 Tire Model for Rezoning

6.3 Quasi-Static Cornering Tire Model

6.3.1 Coarse Mesh Cornering Model on Flat Surface

The coarse mesh static tire model with 24 elements in a sector, constructed by using ABAQUS, is taken to be the base of this cornering model. The material data is same as the static model and no mass or damping data is supplied since rolling speed is assumed to be low. The mirror image of the sector is taken first, then the full sector is copied 52 times to obtain the full tire model. The outer surface of the tread is meshed by 5 noded contact elements of ABAQUS. It is a known fact that the cornering force reaches to its steady-state value after some distance has been rolled (Loeb et al., 1990). To achieve rolling, a rim which can rotate around the tire axle is defined using rigid elements of ABAQUS. 180 kPa inflation pressure is applied to the inner surface of the tire as the first step of the analysis. In the second step tire is pressed to rigid ground by a predefined displacement which corresponds to 2 kN vertical load approximately. As the third step, the tire is rolled on the rigid ground by a known slip angle which is 2 degrees, by moving the rigid ground. The cornering force increases as the tire rolls and attains a steady state value of 1015 N after the tire makes half a rotation. On an HP 715/50 workstation, it took 26 days (real time) for the model to reach steady state. The variation of cornering force versus distance rolled is plotted is illustrated in Figure 6.2.

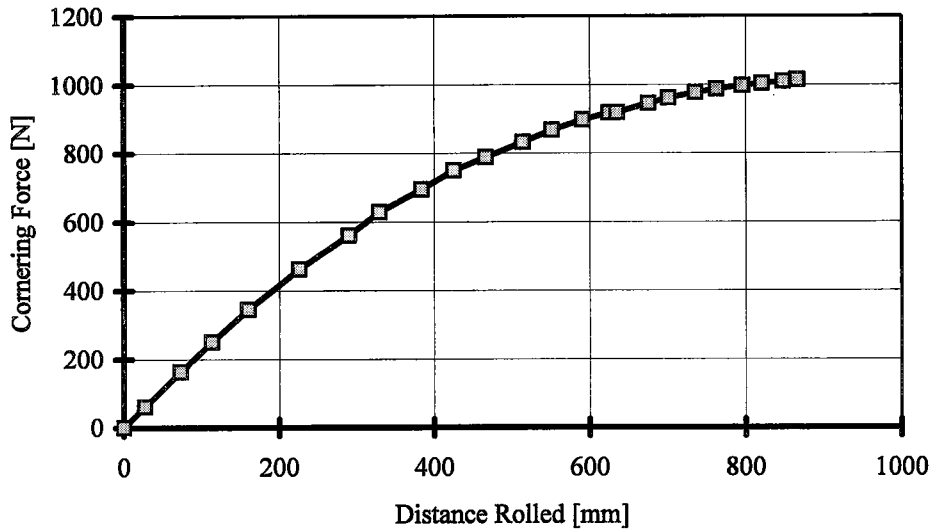


Figure 6.2 Variation of Cornering Force with Distance Rolled at 2° Slip Angle (180 kPa Inflation Pressure, 2kN Vertical Load)

6.3.2 Coarse Mesh Quasistatic Cornering Model on Test Machine's Drum

For the first trials, the tire model rolling and cornering on the test machine's drum has 42 rubber matrix elements, 28 textile body ply rebar elements and 12 steel tread ply elements as illustrated in Figure 6.3. The complete rendered tire model on the drum, is shown in Figure 6.4. and the full tire mesh with rim is shown in Figure 6.5. In the contact trajectory, the nodes are placed with 5 degrees increment. At the end of contact trajectory, there exist the transition regions where nodes have 7.5 degrees spacing and rest of the tire, which does not contact to the drum is meshed with 15 degrees spacing. This models consists of 4430 elements and 3800 nodes.

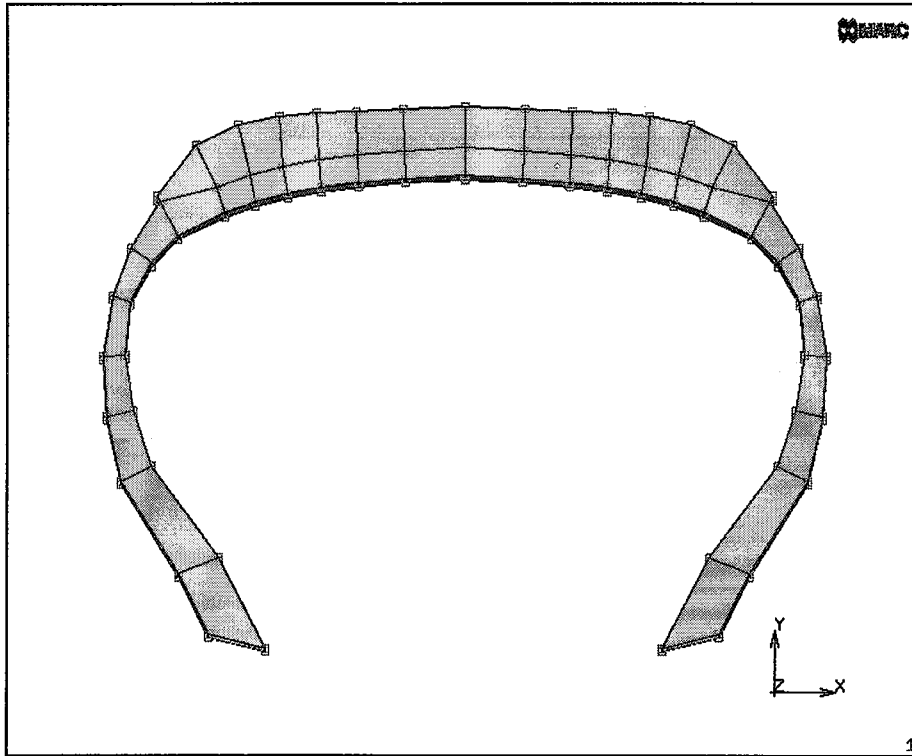


Figure 6.3 Tire Model Sector on the Drum

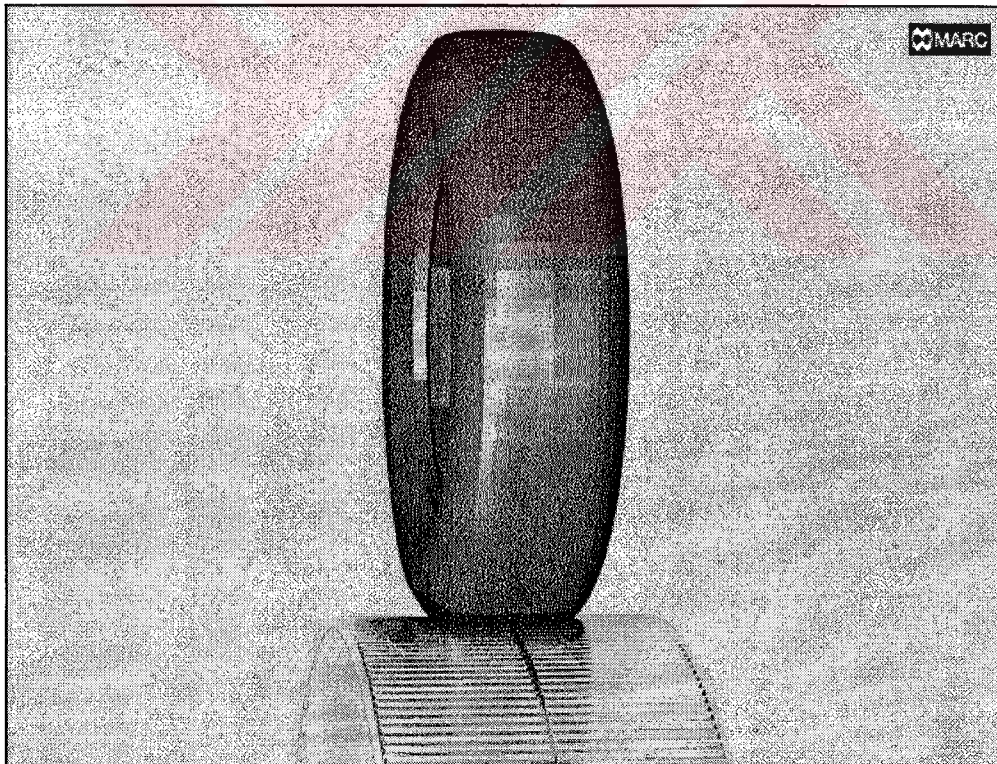


Figure 6.4 Rendered Picture of Tire Model on Drum

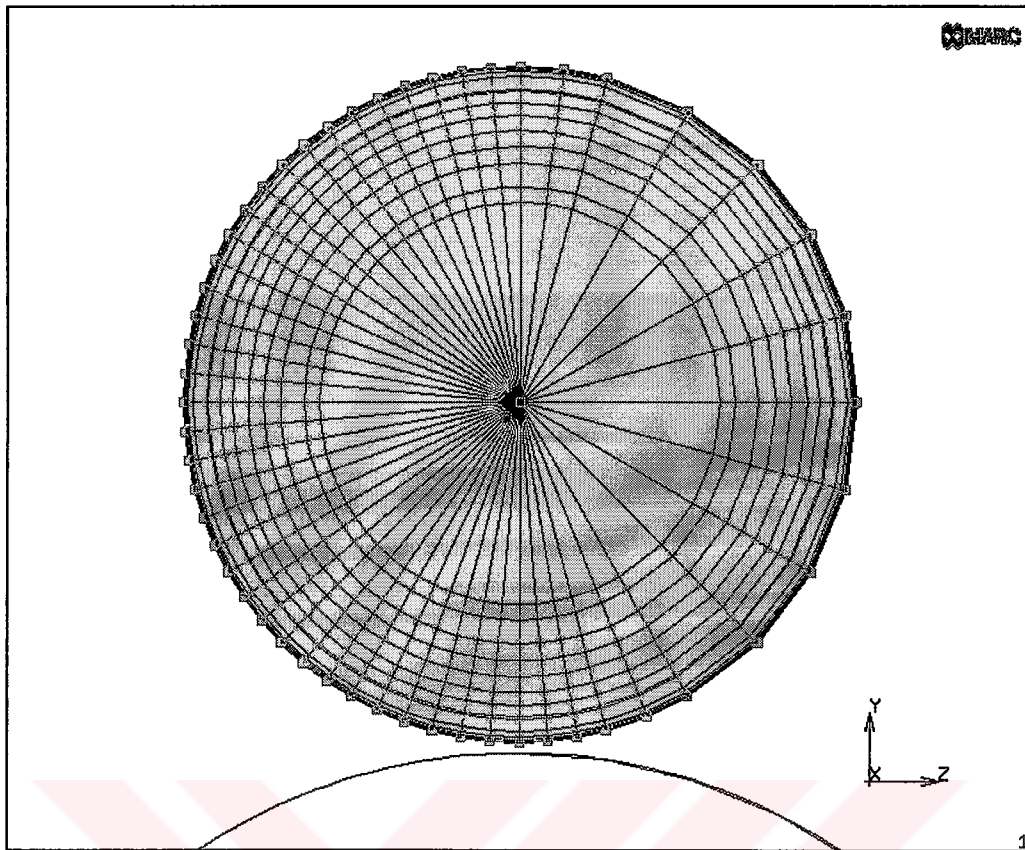


Figure 6.5 Tire Mesh

This model which is a duplicate of physical situation did not yield a usable result. As mentioned in Section 4.2.2, pressure must be normal to the deformed surface and the equivalent nodal forces must be updated if there exists a change in the surface area which is exposed to pressure. In ABAQUS this updating was done quite accurately therefore rolling the tire itself did not cause any trouble. However in MARC, as the tire rotates it was experiencing expansion and warping even if no ground contact exists. After a careful examination with simple pressurized models, it was understood that pressure, combined with steady motion, causes the problem. Since this problem cannot be avoided with any of the available options of follower force in MARC, the only remedy would be to keep the tire fixed and move the drum around the tire to simulate the same situation. This is conceptually a simple kinematic inversion process as shown in Figure 6.6. However MARC has some limitations which makes this simple inversion a rather

tough job. The same limitations introduce some more approximations too. In MARC, a rigid body must have predefined velocity, position change or force, but cannot make a free motion (displacement or rotation) depending on the constraints applied on it. In this case, the drum, which must have a free rotation, has to be formed using deformable elements. In MARC, a rigid body is an analytical entity whose surface normal is evaluated exactly at each point. This enables more precise calculation of contact and frictional forces. This is not available for deformable bodies which are discrete. The drum being deformable brings additional computational effort as well, which will not be used as a result too.

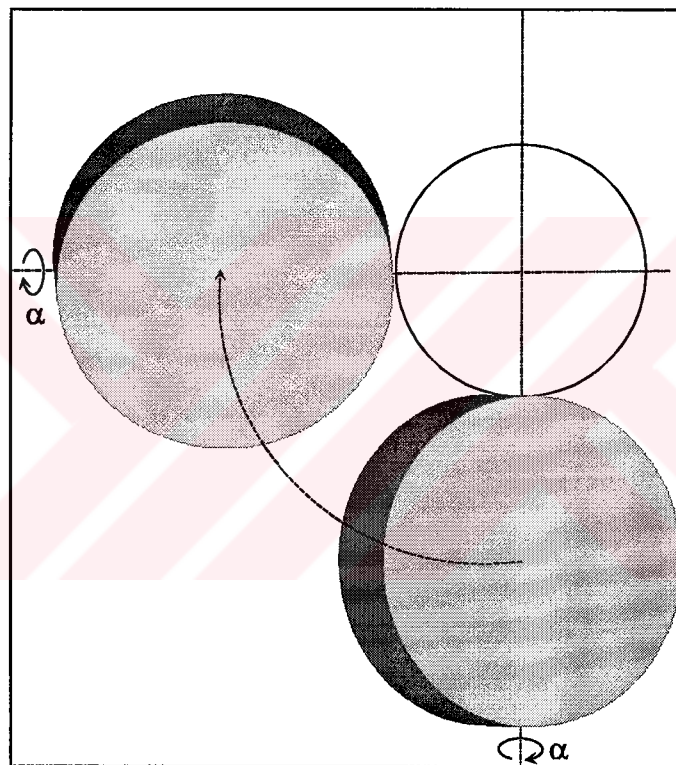


Figure 6.6 Kinematic Inversion to Keep Tire Completely Fixed and Drum Rotating around the Tire

The loci of the two nodes at the rotation center of the drum are evaluated by using the configuration shown in Figure 6.7.

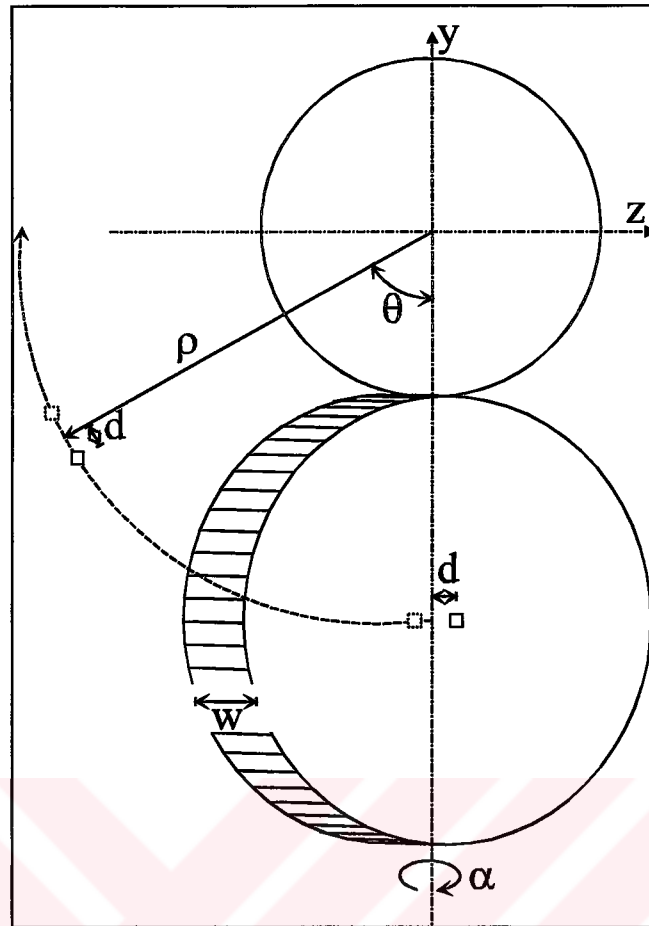


Figure 6.7 Loci of Two Nodes Defining the Drum Center

The position of nodes just before rolling starts is

$$\begin{aligned}
 Y_{\text{front}} &= -\rho \\
 Z_{\text{front}} &= d = \frac{w}{2} \sin(\alpha) \\
 Y_{\text{back}} &= -\rho \\
 Z_{\text{back}} &= -d = -\frac{w}{2} \sin(\alpha)
 \end{aligned}
 \tag{6.1}$$

where front stands for the node whose x coordinate is negative (positive x-axis points into the page in Figure 6.6) and back stands for the node whose x coordinate is positive. ρ is the distance between the drum center and tire center after the vertical load is applied, w is the width of the drum, α is the slip angle. At any time t , the position of the nodes will be

$$\begin{aligned}
y_{\text{front}} &= -\rho \cos(\theta) - \frac{W}{2} \sin(\alpha) \sin(\theta) \\
z_{\text{front}} &= -\rho \sin(\theta) + \frac{W}{2} \sin(\alpha) \cos(\theta) \\
y_{\text{back}} &= -\rho \cos(\theta) + \frac{W}{2} \sin(\alpha) \sin(\theta) \\
z_{\text{back}} &= -\rho \sin(\theta) - \frac{W}{2} \sin(\alpha) \cos(\theta)
\end{aligned} \tag{6.2}$$

where $\theta = \omega t$, ω being the angular speed of the tire and t is the time elapsed since cornering has started. The displacement boundary conditions to be applied to the two nodes of the drum axle during the cornering load step of the analysis is therefore

$$\begin{aligned}
\Delta x_{\text{front}} &= 0 \\
\Delta y_{\text{front}} &= \rho(1 - \cos(\theta)) - \frac{W}{2} \sin(\alpha) \sin(\theta) \\
\Delta z_{\text{front}} &= -\rho \sin(\theta) - \frac{W}{2} \sin(\alpha)(1 - \cos(\theta)) \\
\Delta x_{\text{back}} &= 0 \\
\Delta y_{\text{back}} &= \rho(1 - \cos(\theta)) + \frac{W}{2} \sin(\alpha) \sin(\theta) \\
\Delta z_{\text{back}} &= -\rho \sin(\theta) + \frac{W}{2} \sin(\alpha)(1 - \cos(\theta))
\end{aligned} \tag{6.3}$$

The sine and cosine functions are implemented to the model by tables and formula options of Mentat 3.2. For Mentat to evaluate the values exactly at each time increment, fixed time step size is used and the number of divisions on the tables are made equal to number of time steps.

This model with different vertical loads and slip angles simulates the test conditions done on the tire testing setup. Figure 6.8 shows the deformations on the tire model when it is cornering with a slip angle of 2 degrees and having a vertical load of 2kN. There is visible deformation on tread due to cornering, which is observed during tire tests as well (Figure 7.1). The cornering forces obtained at various slip angle and vertical load combinations are plotted on the cornering characteristics of the experimental data in Figure 6.9. The computer

model results shown with a circle have no centrifugal force while the one shown with a diamond has centrifugal force corresponding to 60 km/h road speed.

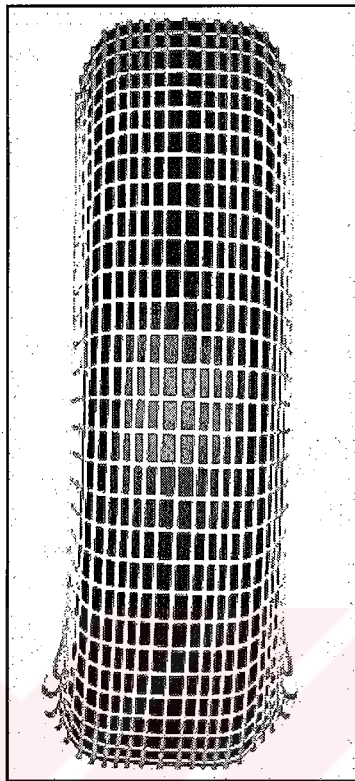


Figure 6.8 Deformations on a Medium Loaded (2kN) Lightly Cornering (2°) 155R13 Tire obtained from Computer Model

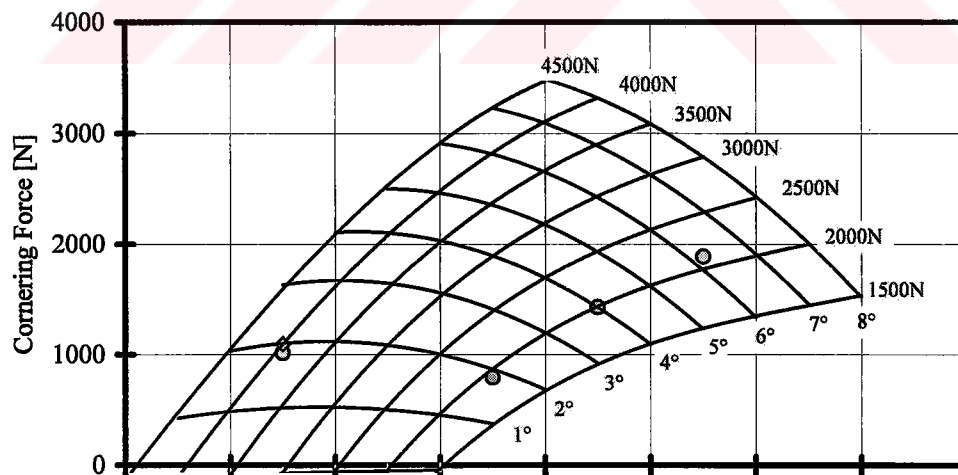


Figure 6.9 Cornering Force Characteristics of 155R13 Obtained from Computer Model, Lines Show Experimental Results (10km/h, 180 kPa)

6.4 Conclusions about Quasi-Static Cornering Tire Models

The cornering force characteristics obtained around 2 kN vertical load shows good agreement with experimental results. However at lower slip angles the cornering force estimated by the computer model is less than the one determined experimentally while for higher slip angles it is higher. This slight discrepancy may be due to one of the reasons stated below or a combination.

- **Friction Model and Coefficient of Friction:** In models presented, mostly regularized Coulomb friction model is used which permits small sliding. For some trials, stick-slip friction model is used to see the difference but although there is considerable increase in solution time, the change in tire behavior is minor. Coefficient of friction of rubber on smooth steel test drum is estimated by an impending motion test which gives an idea about static coefficient of friction. Any inconsistency in friction model or coefficient of friction will have an impact on computer model results.

- **Tire Material Properties:** Each rubber, depending on the proportions of constituents and treatment, has different elastic properties. In this research, elastic properties of rubber are obtained from different references and manufacturers as typical values. The same uncertainty goes with the reinforcement elastic properties which may cause computer models behave different than physical tire.

- **Reinforcement Model:** Textile and steel reinforcement in tire are modeled by unidirectional reinforcing models. These models neglect bending which may be important in case of steel cords and they neglect the coupled behavior of twisted textile fibers. Reinforcement models neglect interply effects which may be rather pronounced in some cases.

- **History and Temperature Dependent Material Behavior of Rubber:** Rubber has pronounced history and temperature dependent elastic properties. In tire tests, tire is “conditioned” before the data is collected which brings the tire to a steady state temperature and deformation history. This rather complicated behavior is not modeled as well as different temperature states at different steady-state cornering conditions.

Since the problem is nonlinear, the effect of each individual effect has to be investigated and only the significant ones must be included in the more detailed models.



CHAPTER 7

CONCLUSION AND RECOMMENDATIONS FOR FURTHER STUDIES

7.1 Introduction

In this work, cornering force characteristics of automobile tires are obtained using finite element computer models and the results obtained are verified experimentally by the tire testing setup constructed. Tire models start with static ones to gain insight about tire materials and behavior and extended to quasi-static rolling models some of which are enhanced with centrifugal load due to rolling.

7.2 Conclusions about Present Work

7.2.1 Tire Testing Setup

The external drum tire testing setup constructed can perform cornering and rolling resistance tests on most of the automobile tires. When compared with other external drum tire testing machines, according to the drum size and driving motor power it is a rather small machine. According to the maximum road speed, maximum tire load and maximum slip angle attainable, the test machine is in a rather good place among others.

The test machine besides supplying the cornering force characteristics, supplies insight about the deformations on a cornering tire as shown in Figure 7.1.

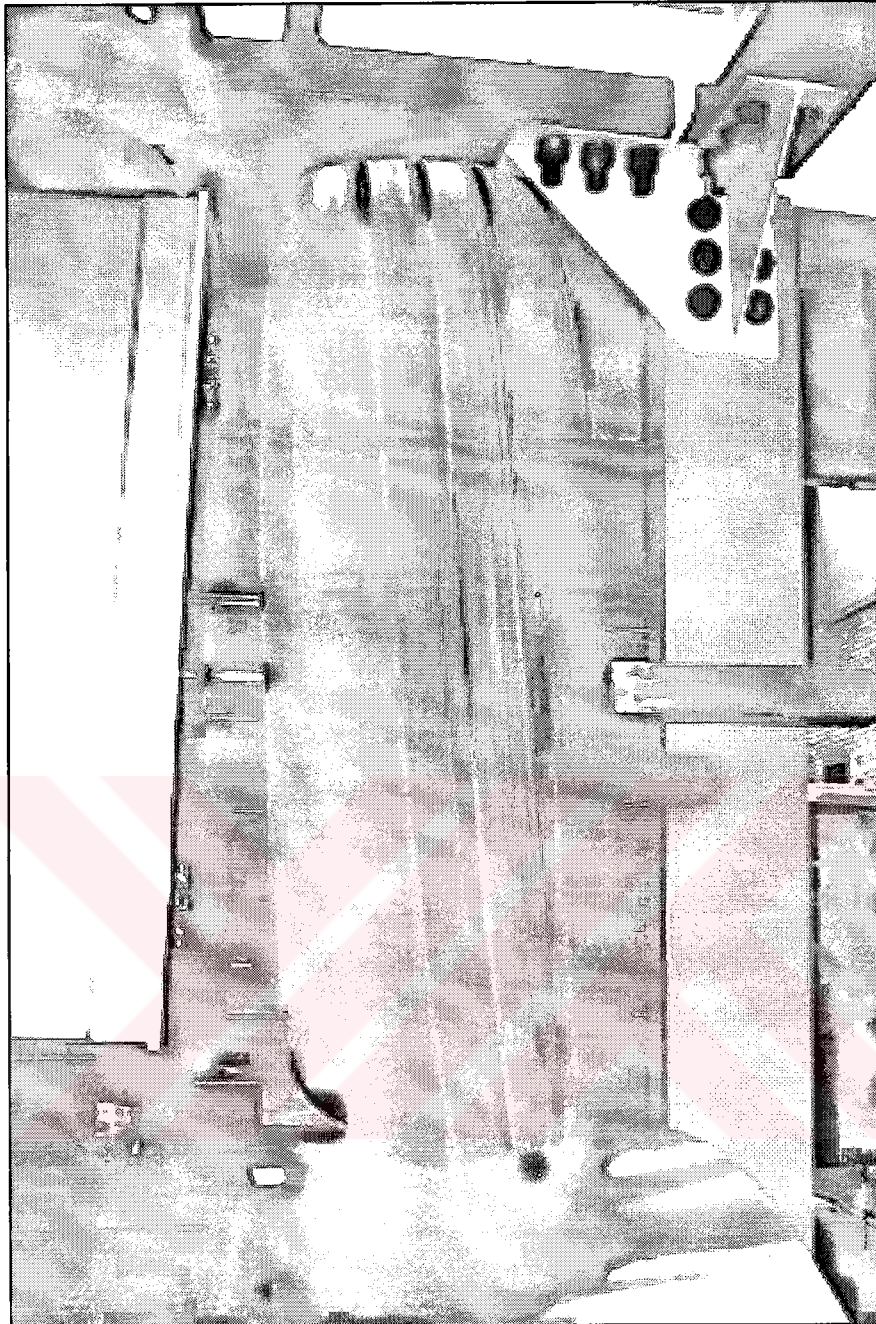


**Figure 7.1 Deformed Photograph of 155R13 Tire
at 8° Slip Angle and 3500 N Load**

7.2.2 Static Tire Models

Static tire models supply a good insight to elastic behavior of pneumatic tires. The effects of reinforcement and the way it is modeled to obtain the same

deformations when a real tire is inflated and pressed on a rigid surface are examined by the static models. Using static models, the effect of material properties and microbuckling in reinforcement are tuned. The effect of different meshes on model results are examined. Different carcass constructions on different rims are rim seated and inflated using axisymmetric models.

7.2.3 Cornering Tire Models

Quasi-static models, although have simplifications, modeled the cornering behavior of pneumatic tires rather precisely. With minor improvements, these models may be used to estimate the cornering behavior of tires in design stage, reducing the need for prototyping and experiments. The same models may be used to understand the cornering phenomena in more detail as well.

7.3 Recommendations for Further Studies

7.3.1 Recommendations for Increased Model Accuracy

As in most modeling processes of a physical phenomena, in tire models, there are three main parts. The data input to the model, the governing equations and theory used, and the simplifications and/or assumptions to make the model manageable and/or to approximate a phenomena which is not known in great detail. For tire models, data input are, geometric properties of the tire, which include tire dimensions, reinforcement properties (ends per decimeter, location and ply angle, yarns per meter for textile), material properties of various components including at least three rather different types of rubber (some authors use up to 8 different rubber types like Helnwein, et al., 1993 for precise modeling purposes) and reinforcement. Determination of frictional properties of rubber with contacting surfaces would improve model accuracy. As for the governing equations, the linear elastic material response and Mooney-Rivlin material

models may be compared using a sensitivity analysis. In modeling the reinforcement, rebar elements are the most precise ones available for tire composites. Rebar elements have some simplifications. They share the same nodes with the matrix element which imposes exactly the same displacements on rebar as the matrix element. This condition is quite similar to perfect bonding between reinforcement and matrix material. This assumption may be obeyed by textile reinforcements quite accurately. However especially in used tires, the steel reinforcements loosen the rubber surrounding them and can move with respect to rubber which is ignored in models. Another simplification in rebar concept is, being unidirectional, rebar elements carry only tension or compression and only in the direction of reinforcement. They have no other stiffnesses whereas bending stiffness of steel reinforcement may be significant when compared to that of rubber, and in such a case it must be considered as well. In case of textile reinforcement, due to twist, a coupled physical behavior is indicated in literature (Padovan, 1998) which is ignored by the present rebar elements. Effect of temperature change (in the operating temperature range) on material properties of rubber as well as on thermal strains should be investigated. However, in order to go beyond the present point in geometric and material properties, it is inevitable to cooperate with a tire company to obtain detailed geometric data about the tire, specimens of various rubber components for different experimental purposes and the experience of the company.

For finite element analysis, another approximation is introduced by discretization. The first improvement would be refining the mesh especially at the contact trajectory. While refining the mesh, the number of elements and nodes must be increased but not the order of the interpolation functions of the elements. Higher order elements do not yield precise results in contact analysis as the linear ones does (ABAQUS, 1994b, MARC, 1994a, 1997b). Finer mesh requires increased computer time and storage resources in return. With finer mesh, the

geometric details of the tire like tread pattern may be modeled with greater accuracy too.

7.3.2 Recommendations for Increased Computational Efficiency

When the details of tread pattern is ignored, tire has a rather simple axisymmetric geometry. Inflation and rim seating processes, when analyzed by an axisymmetric model, do not contain oversimplifications. After completing the inflation and rim seating in an axisymmetric model, transferring this state to a three-dimensional model for further non-axisymmetric loading would reduce the computer time considerably for inflation analysis whereas rim seating would be modeled as well. Another great improvement would be using Arbitrary Eulerian-Lagrangian formulation in rolling tire analysis. The tire rotation is formulated in an Eulerian sense, where the mesh remains fixed in space and as the tire rolls, material flows through the mesh. This keeps the contact patch at a fixed mesh location on the tire where the fine mesh exists and other parts of the tire can be meshed by a relatively coarser mesh. On the other hand, tire deformations are modeled in Lagrangian sense which ensures that the mesh deforms with tire material and no part of the mesh contains a void or material flows out of mesh. ABAQUS (1998) is about to include a special type of arbitrary Eulerian-Lagrangian formulation for axisymmetric structures like tires.

7.3.3 Improvements on Tire Testing Setup

The tire testing setup is constructed with a limited fund, therefore one of the most important design criteria was cheapness which lead simplicity. This simplicity requirement limited the variety of test conditions in some cases and caused problems in other cases.

At higher test speeds, if the slip angle and/or vertical load on the tire are high, the tire heats up to the temperatures where tread pattern is damaged. Heating is not so severe in real operating conditions because tire cools down due to the wind at high speeds. A similar condition may be simulated using a blower. In this case, both high speed high slip angle and/or high vertical tire load tests may be performed. The results obtained would be more realistic since tire would be at a temperature state closer to the real working conditions.

Tire testing setup can perform steady-state cornering experiments at a fixed slip angle. With minor modifications, the slip angle may be varied during tests. In such a case, the driving motor grounding must be isolated from that of the force plate to avoid electrical noise effecting the signals and the need for averaging the data, to filter out the noise in signal would be reduced.

Without any modifications, the tire testing setup may be used for tire rolling resistance experiments, which may be some part of a wider area research on tire rolling resistance.

APPENDIX A

REBAR SUBROUTINES IN MARC

A.1 Introduction

The reinforcement characteristics of a tire play an important role in the dynamic response and performance of a tire. Reinforcement found in most radial automobile tires, including the tire modeled is shown in Figure A.1. The results obtained from finite element tire models therefore, heavily depend on the precision in modeling the reinforcement of the tire. Special reinforcing bar (rebar) elements, which is the most precise way available to model the unidirectional reinforcements, are used. Finite element software MARC needs the three direction cosines of the reinforcing fibers, thickness of the rebar element, relative position of reinforcing layer in the element and equivalent thickness of the reinforcing layer for every integration point belonging to a rebar element. Besides these, number of reinforcing layers in the element, material properties of the reinforcing layer, surface to which the layers are similar to (this is required only in version K7 and higher, for K6 versions, layers can only be similar to 1-2 side or 1-2-3-4 face) must be defined. The undeformed (initial) configuration of the tire is axisymmetric if the tread pattern is ignored, therefore using a global coordinate system, the three direction cosines of the reinforcing bars may be defined easily. When it comes to deformations, which cannot assumed to be infinitesimal, the reinforcing layers must be deformed with the rubber matrix and direction cosines of the reinforcing elements must be updated accordingly. The following subroutines are devised to update the directions of reinforcements for

large deformations. Since the strains in the rather stiff reinforcing fibers are small, the change in their cross-sectional area are neglected. In case of compliant reinforcements, this may be included in the rebar subroutines as well.



Figure A.1 Radial Tire Reinforcement

A.2 General Structure of REBAR Subroutine and BelongToSet Function

A.2.1 REBAR Subroutine for MARC Versions K6.x Family

The general structure of the rebar subroutine is

```
SUBROUTINE REBAR (N, NN, T, PR, TR, A)
IMPLICIT REAL *8 (A-H, O-Z)
DIMENSION A(3)
```

user coding

```
RETURN
END
```

where

N : element number (defined by the program)
NN : integration point number (defined by the program)
T : element thickness
PR : relative position of rebar layer in the element
TR : equivalent thickness of the rebar layer
A : direction cosines of the rebar fibers

Since the vector A is internally normalized by the program, it may be any tangent vector to the fibers.

A.2.2 REBAR Subroutine for MARC Versions K7.x Family

The general structure of rebar subroutine is

```
SUBROUTINE REBAR (N, NN, T, PR, TR, A)  
IMPLICIT REAL *8 (A-H, O-Z)  
DIMENSION A(3), NN(3)
```

user coding

```
RETURN  
END
```

where all the parameters are the same as versions K6.x except

NN(1) : integration point number
NN(2) : rebar layer number
NN(3) : integration point number in this layer.

A.2.3 BelongToSet Function

BelongToSet is a logical function which determines the set name to which an element, node, integration point, layer, degree-of-freedom or increment belongs to. The first variable in BelongToSet determines the type of the target quantity, the second parameter is the number of the target quantity (element number, node number etc.) and the third parameter is the set name to be checked

if the target belongs or not. If target quantity is an element of the set, `BelongToSet` logical variable returns `.TRUE.`, if not it returns `.FALSE.` `BelongToSet` function is very useful in identifying the similar quantities in a set indexed with the set name.

The following is the list of `BelongToSet` function

```

logical function belongToSet (typeTarget, numTarget, setTarget)
implicit real*8 (a-h,o-z)
c
external:
integer      typeTarget      ! must be an ipttyp (see below)
integer      numTarget       ! element number or node number, etc.
                                     ! AFTER RENUMBERING!!!!!!
character*(*) setTarget      ! Setname (LOWER CASE!!!)

c
internal:
character*1  name
character*12 setName
dimension   iiname(12)

c
common blocks:
include '/academic/marck62/common/dimen'
include '/academic/marck62/common/setnam'
include '/academic/marck62/common/space'

c In the common block /setnam/, the following variables are defined:
c   ndset:  number of defined Sets
c   nsetmx: maximum number of Sets corresponding parametercard SETNAME
c   (default: nsetmx =10)
c   iptnam: pointer to the Setname. Each Setname takes 12
c           characters and will be stored in integer format.
c   ipttyp: pointer to the set type:
c           ipttyp  Set type
c           0      Elements
c           1      Nodes
c           2      Integration points
c           3      Layers
c           4      Degrees-of-freedom
c           5      Increments
c   iptnum: pointer to the number of elements in set
c   iptloc: pointer to the stored elements in set
c   iptbeg: pointer to all stored elements

c
loop over all sets
do iset = 1, ndset

    istype = ints (ipttyp + (iset-1))

    if ( istype.eq.typeTarget ) then

        isname = (iptnam +(iset-1)*12)
        do j=1,12
            iiname(j) = ints(isname+j-1)
            write(name,'(A1)') iiname(j)
            setName(j:j) = name
            if (name .ne. ' ') then
                isnamlen = j
            end if
        end do
    end if
end do

```

```

end do

if (setName (1:isnamlen) .eq. setTarget) then

  isnumb = ints (iptnum+iset-1)

  ieptr = iptbeg + ints (iptloc+iset-1)-1

  do i=1, isnumb
    iexx = ints(ieptr+i-1)
    if (numTarget .eq. iexx) then
      belongToSet = .True.
      return
    end if
  end do
  belongToSet = .False.
  return
endif

end if

end do

write(*,*) 'belongToSet: set ',setTarget,'* not found'
belongToSet = .FALSE.

return
end

```

A.2.4 Determination of Current Positions of Nodes

Determination of the current (deformed) position of the nodes is essential to assign the correct current direction cosines of the reinforcing bars. MARC keeps initial (undeformed) coordinates of the nodes and it evaluates the displacements of the nodes at the end of each increment. The following lines return the initial coordinates of the node number II of element N in array variable $CCNODE$ and displacements in array variable $DDNODE$ when added yields the current position of the node which is stored in an array variable called $CURPOS(II, JJ)$ where II stands for node number of the element and JJ stands for coordinate number..

```

include '/academic/marck62/common/blnk'
include '/academic/marck62/common/dimen'
include '/academic/marck62/common/array2'
include '/academic/marck62/common/space'
include '/academic/marck62/common/elmcom'
DIMENSION A(3),CCNODE(12),DDNODE(12),CURPOS(20,12)
DO 2 II=1,20,1
  LINT=LM(II)
  DO 1 JJ=1,3,1
C THIS DETERMINES INITIAL COORDINATES OF THE NODES

```



```

JRDPRE=0
CALL VECFTC (CCNODE, VARS (IXORD), NCRDMX, NCRD, LINT, JRDPRE, 2, 1)
C THIS DETERMINES THE DISPLACEMENTS OF THE NODES
JRDPRE=0
CALL VECFTC (DDNODE, VARS (IDSXT), NDEGMX, NDEG, LINT, JRDPRE, 2, 5)
CURPOS (II, JJ) = CCNODE (JJ) + DDNODE (JJ)
1 CONTINUE
2 CONTINUE

```

A.2.5 Determination of Equivalent Layer Thickness

In MARC, reinforcement is modeled as uniform layers of reinforcing material. Therefore in case of reinforcing bars, the equivalent thickness is evaluated by equating the cross-sectional area of circular reinforcing bars to that of the uniform layer as

$$\begin{aligned}
 A_{\text{rein}} &= \ell n \pi r^2 \\
 A_{\text{eq}} &= \ell t
 \end{aligned}
 \tag{A.1}$$

where A_{rein} is the actual reinforcement area, ℓ is the length of the element, n being number of reinforcement bars per unit length and r being the radius of a single reinforcing member. A_{eq} is the equivalent reinforcement area and t is the equivalent thickness which MARC uses. The tire producers mostly use epd (ends per decimeter) as the unit for the amount of reinforcing in a tire. The epd is one tenth of ends per meter, which is n . Equating both areas in Equation A.1 and solving for equivalent thickness yields

$$t = n \pi r^2 = \frac{n}{4} \pi d^2
 \tag{A.2}$$

where n is number of circular reinforcing bars per meter, r is the radius and d is the diameter of circular reinforcing bars in meters.

A.3 Axisymmetric Rebar Subroutine for Quadratic Elements

In axisymmetric models three or four types of reinforcement are used, these are the bead bundle, body ply, tread plies and sometimes the overlay. The bead bundle and overlay are perpendicular to the axisymmetric plane and their

orientation do not change with deformation. The body ply is parallel to the inner surface of the tire and remains so in any deformation that is possible as shown in Figure A.2. The tread ply is in the plane formed by the tire inner surface and the line perpendicular to the axisymmetric plane, the ply angle is between the reinforcing fibers and the perpendicular to the axisymmetric plane as shown in Figure A.3. The following subroutine evaluates the rebar directions for axisymmetric tire model with quadratic elements. The tire modeled has bead bundle, one textile body ply and two steel tread plies. The subroutine is for MARC K6.x versions.

```

SUBROUTINE REBAR (N,NN,T,PR,TR,A)
C VERSION 3.AXful, Ergin TONUK
  IMPLICIT REAL *8 (A-H,O-Z)
  LOGICAL belongToSet
  include '/academic/marck62/common/blk'
  include '/academic/marck62/common/dimen'
  include '/academic/marck62/common/array2'
  include '/academic/marck62/common/space'
  include '/academic/marck62/common/elmcom'
  DIMENSION A(3),CCNODE(12),DDNODE(12),CURPOS(4,12),
  /B(12),C(12),D(12)
  CON=DATAN(1.D0)/45.D0
  DO 2 II=1,4,1
C THE FIRST NNODE NUMBERS OF LM ARE INTERNAL NODE NUMBERS!
  LINT=LM(II)
  DO 1 JJ=1,2,1
    JRDPRE=0
    CALL VECFTC(CCNODE, VARS(IXORD), NCRDMX, NCRD, LINT, JRDPRE, 2, 1)
    JRDPRE=0
    CALL VECFTC(DDNODE, VARS(IDSXT), NDEGMX, NDEG, LINT, JRDPRE, 2, 5)
    CURPOS(II, JJ)=CCNODE(JJ)+DDNODE(JJ)
  1 CONTINUE
  2 CONTINUE
  DO 3 JJ=1,2,1
    B(JJ)=CURPOS(2, JJ)-CURPOS(1, JJ)
    D(JJ)=CURPOS(4, JJ)-CURPOS(1, JJ)
    C(JJ)=CURPOS(3, JJ)-CURPOS(2, JJ)
  3 CONTINUE
  DMAG=(DSQRT(D(1)**2+D(2)**2)+DSQRT(C(1)**2+C(2)**2))/2.D0
  BL=DSQRT(B(1)**2+B(2)**2)
  CL=DSQRT(C(1)**2+C(2)**2)
  DL=DSQRT(D(1)**2+D(2)**2)
C NORMALIZATION
  DO 4 JJ=1,2,1
    B(JJ)=B(JJ)/BL
    C(JJ)=C(JJ)/CL
    D(JJ)=D(JJ)/DL
  4 CONTINUE
  IF (belongToSet(0, n, 'bead_bundle').EQV..TRUE.) THEN
    A(1)=0.D0
    A(2)=0.D0
    A(3)=1.D0
    PR=0.5D0*DMAG
    TR=0.9D0*DMAG

```

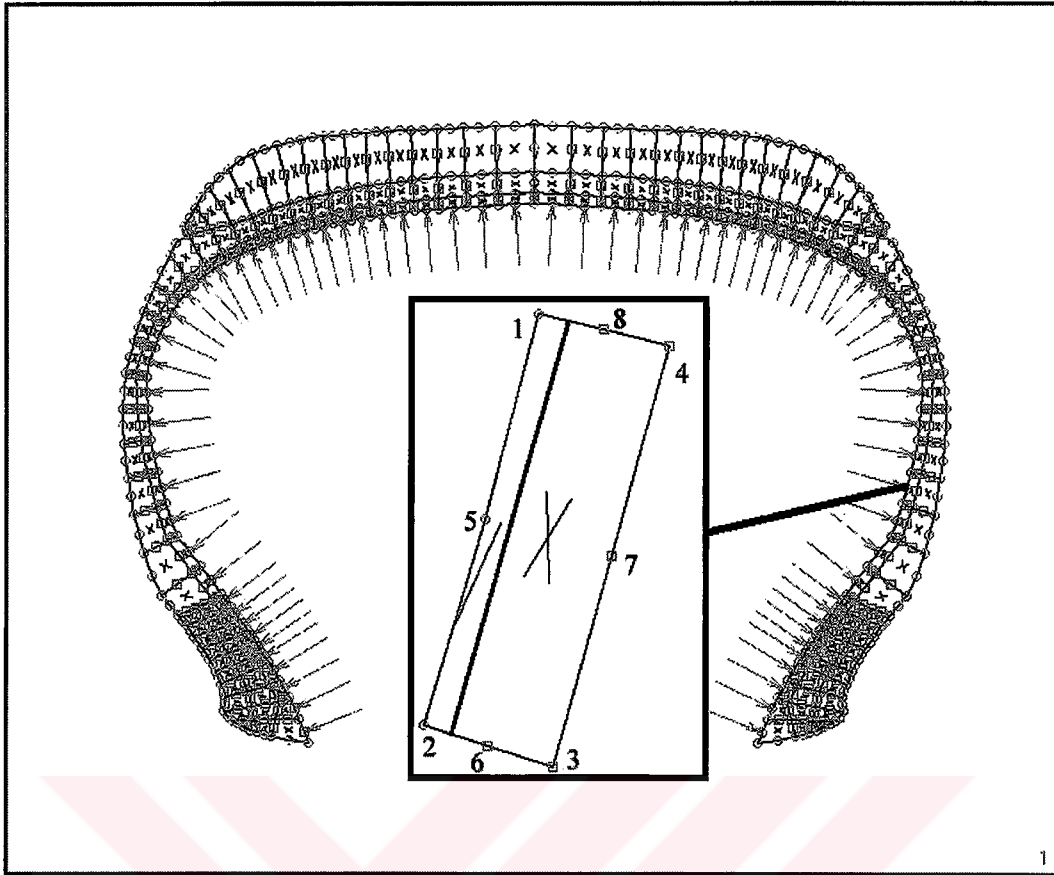


Figure A.2 Body Ply Reinforcement Direction in Axisymmetric Model

```

T=DMAG
ENDIF
IF (belongToSet(0, n, 'body_ply').EQV..TRUE.)THEN
  A(1)=B(1)
  A(2)=B(2)
  A(3)=0.D0
  PR=0.5D0*DMAG
  TR=0.287D-3
  T=DMAG
ENDIF
IF (belongToSet(0, n, 'tread_ply') .EQV. .TRUE.) THEN
  IF (NN .LT. 3) THEN
    ALP=-20.D0*CON
    PR=0.3D0*DMAG
  ELSE
    ALP=20.D0*CON
    PR=0.7D0*DMAG
  END IF
  CA=DCOS(ALP)
  SA=DSIN(ALP)
  A(1)=SA*B(1)
  A(2)=SA*B(2)
  A(3)=CA
  TR=0.162D-3

```

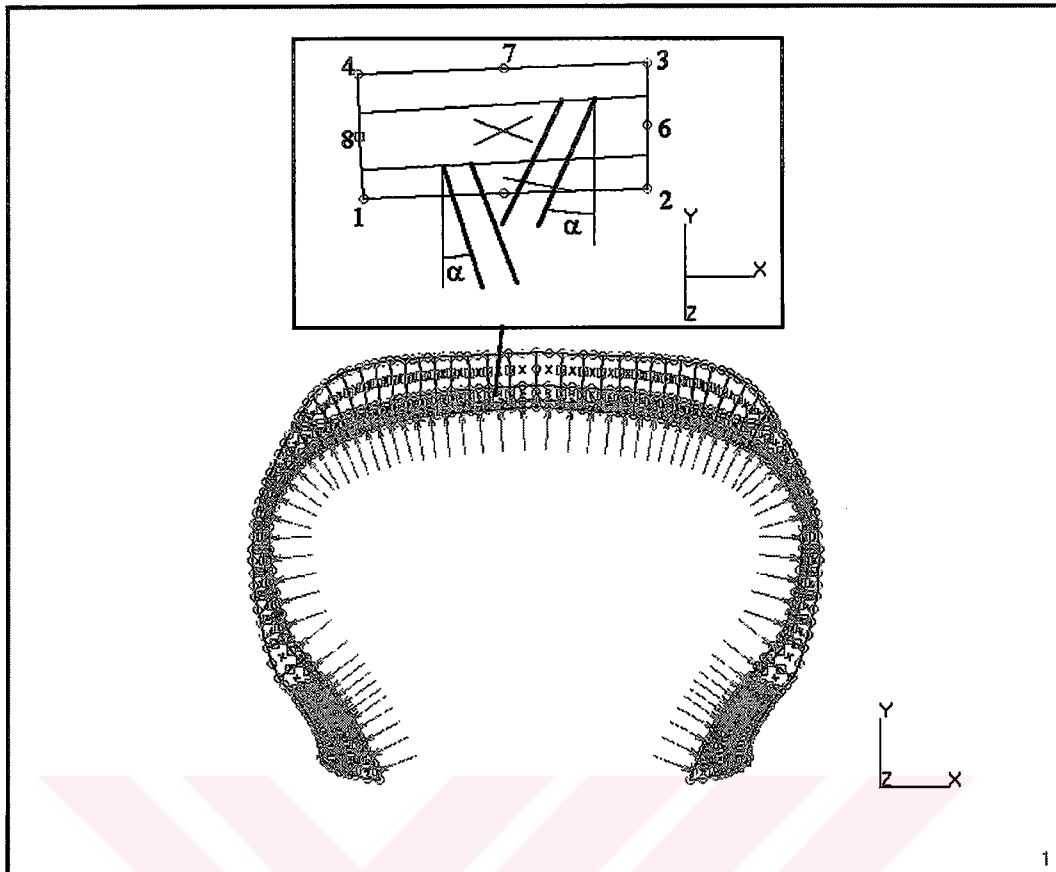


Figure A.3 Tread Ply Reinforcement Direction in Axisymmetric Model

```
T=DMAG
ENDIF
RETURN
END
```

```
logical function belongToSet (typeTarget, numTarget, setTarget)
```

```
implicit real*8 (a-h,o-z)
```

```
integer      typeTarget      ! must be an ipttyp (see below)
integer      numTarget       ! element number or node number, etc.
                                ! AFTER RENUMBERING!!!!!!
character(*) setTarget       ! Setname (LOWER CASE!!!)

character*1  name
character*12 setName
dimension   iiname(12)
```

```
include '/academic/marck62/common/dimen'
include '/academic/marck62/common/setnam'
include '/academic/marck62/common/space'
```

```
do iset = 1, ndset
```

```

istype = ints (ipttyp + (iset-1))

if ( istype.eq.typeTarget ) then

  isname = (iptnam +(iset-1)*12)
  do j=1,12
    iiname(j) = ints(isname+j-1)
    write(name,'(A1)') iiname(j)
    setName(j:j) = name
    if (name .ne. ' ') then
      isnamlen = j
    end if
  end do

  if (setName (1:isnamlen) .eq. setTarget) then

    isnumb = ints (iptnum+iset-1)

    ieptr  = iptbeg + ints (iptloc+iset-1)-1

    do i=1, isnumb
      iexx = ints(ieptr+i-1)
      if (numTarget .eq. iexx) then
        belongToSet = .True.
        return
      end if
    end do
    belongToSet = .False.
    return
  endif
endif

end if

end do

write(*,*) 'belongToSet: set ',setTarget,'* not found'
belongToSet = .FALSE.

return
end

```

A.4 Rebar Subroutines for Three-Dimensional Solid Elements

In three dimensional models, due to ground contact, deformations are larger when compared to the axisymmetric models and may cause circumferential displacements as well. The various rebar subroutines written for three-dimensional analyses considers these deformations as well as displacements due to tire rolling in cornering analysis.

A.4.1 Rebar Subroutine for 20 Node Continuum Element

In three-dimensional models rim is not modeled and fixed boundary condition is applied to tire bead therefore bead bundle loses its essential effect and is not modeled. Body ply is again in 1-2 direction and remains parallel to current (deformed) 1-2 direction. However, due to ground contact, severe deformations occur on tire sidewall and nodes 1-9-2 may deviate substantially from being collinear which necessitates considering different rebar directions depending on the position of the integration point as shown in Figure A.4. The tread ply is parallel to 1-2-3-4 face and the ply angle is measured from side 1-4 as shown in Figure A.5. The following subroutine is for MARC K6.x family and for 20 noded (element 23) rebar.

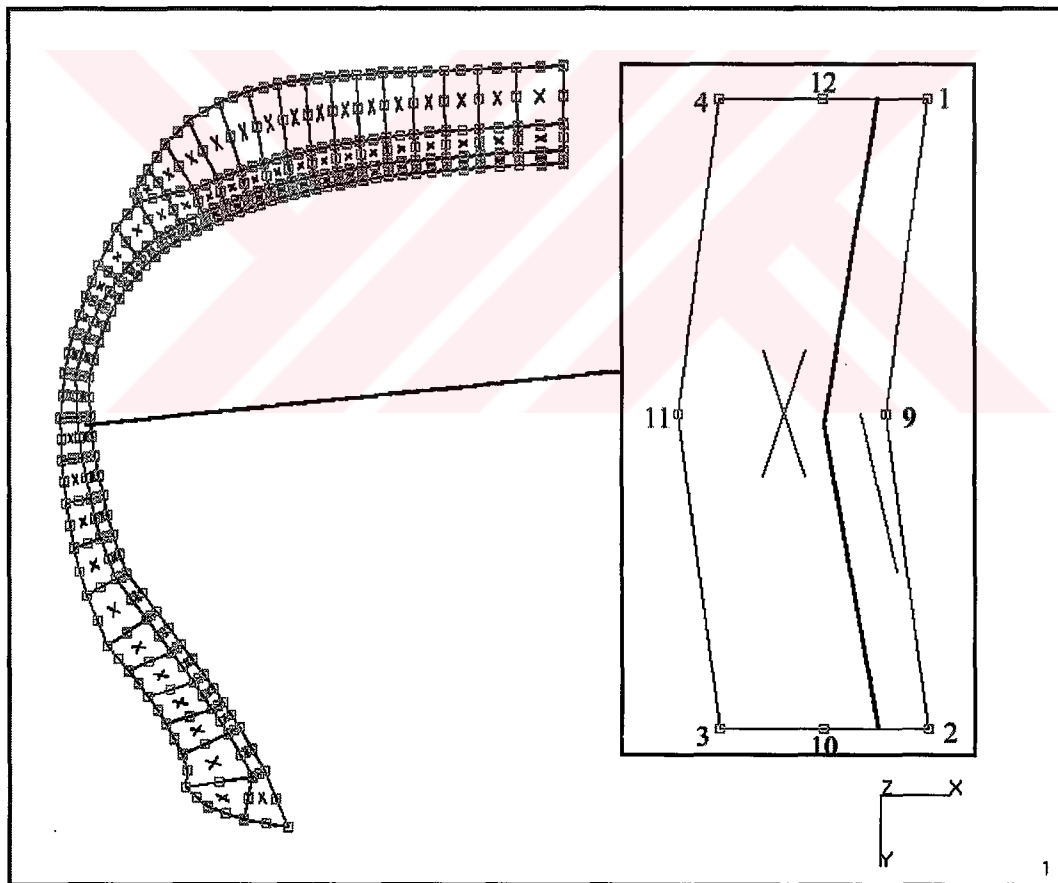


Figure A.4 Body Ply Reinforcement Direction in Three-Dimensional Model

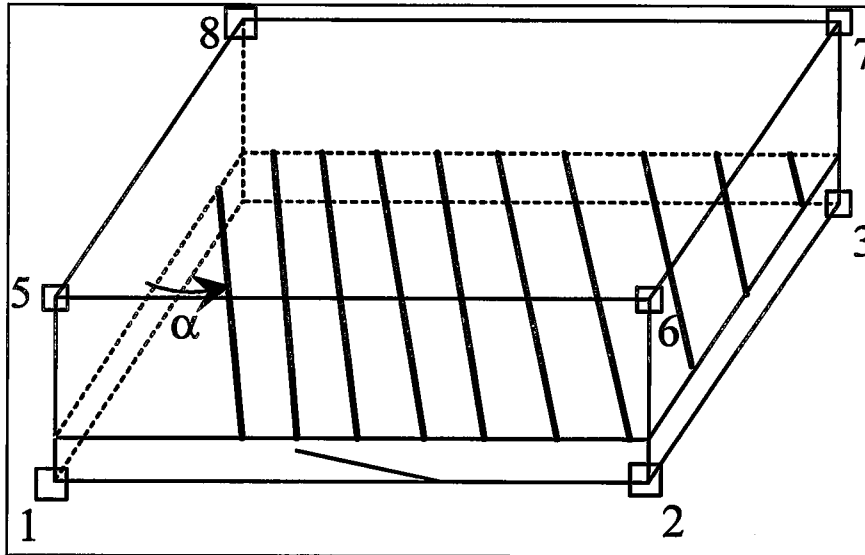


Figure A.5 Tread Ply Reinforcement Direction in Three Dimensional Model
(only Corner Nodes are Shown for Simplicity)

```

SUBROUTINE REBAR (N,NN,T,PR,TR,A)
C VERSION 3.21, 09.10.1997, for 3D Model!
C CONSIDERS LARGE SECTOR ROTATIONS!
C DETECTS THE ELEMENT SET AND DEFINES REBAR DIRECTION AND THICKNESS ACCORDINGLY!
  IMPLICIT REAL *8 (A-H,O-Z)
  LOGICAL belongToSet, RESULT1, RESULT2, RESULT3, RESULT4
  include '/academic/marck62/common/blk'
  include '/academic/marck62/common/dimen'
  include '/academic/marck62/common/array2'
  include '/academic/marck62/common/space'
  include '/academic/marck62/common/elmcom'
  DIMENSION A(3), CCNODE(12), DDNODE(12), CURPOS(20,12), DCM(3),
  /B(12), C(12), D(12), B1(12), B2(12), C1(12), C2(12), D1(12), D2(12)
C DEPENDING ON ELEMENT SET THE REBAR PROPERTIES ARE ASSIGNED BELOW!
C ALPHA IS THE ANGLE BETWEEN THE PLY AND 12 DIRECTION
  DO 2 II=1,20,1
    LINT=LM(II)
    DO 1 JJ=1,3,1
C THIS DETERMINES INITIAL COORDINATES OF THE NODES
      JRDPRE=0
      CALL VECFTC(CCNODE, VARS(IXORD), NCRDMX, NCRD, LINT, JRDPRE, 2, 1)
C THIS DETERMINES THE DISPLACEMENTS OF THE NODES
      JRDPRE=0
      CALL VECFTC(DDNODE, VARS(IDSXT), NDEGMX, NDEG, LINT, JRDPRE, 2, 5)
      CURPOS(II, JJ)=CCNODE(JJ)+DDNODE(JJ)
C      WRITE(*,*) 'Current Position, Node, DOF:', CURPOS(II, JJ), II, JJ
1 CONTINUE
2 CONTINUE
  DO 3 JJ=1,3,1
    B(JJ)=CURPOS(2, JJ)-CURPOS(1, JJ)
    D(JJ)=CURPOS(4, JJ)-CURPOS(1, JJ)
    C(JJ)=CURPOS(5, JJ)-CURPOS(1, JJ)
    B1(JJ)=CURPOS(10, JJ)-CURPOS(2, JJ)
    B2(JJ)=CURPOS(3, JJ)-CURPOS(10, JJ)
    C1(JJ)=CURPOS(17, JJ)-CURPOS(1, JJ)
    C2(JJ)=CURPOS(5, JJ)-CURPOS(17, JJ)
    D1(JJ)=CURPOS(12, JJ)-CURPOS(1, JJ)
    D2(JJ)=CURPOS(4, JJ)-CURPOS(12, JJ)
  
```



```

C      WRITE(*,*) 'Directions',B(JJ),C(JJ),D(JJ)
      3 CONTINUE
C ELEMENTAL UNIT VECTORS (MAY not BE ORTHONORMAL!!)
C ELEMENT THICKNESS 15!!
      BMAG=DSQRT(B(1)**2+B(2)**2+B(3)**2)
      CMAG=DSQRT(C(1)**2+C(2)**2+C(3)**2)
      DMAG=DSQRT(D(1)**2+D(2)**2+D(3)**2)
      CON=3.1415926536D0/180.D0
      T=CMAG
      DO 4 JJ=1,3,1
        B(JJ)=B(JJ)/BMAG
        C(JJ)=C(JJ)/CMAG
        D(JJ)=D(JJ)/DMAG
      4 CONTINUE
      IF (belongToSet(0, n, 'bead_bundle').EQV..TRUE.)THEN
C REBAR IN 15
      IF (NN .LT. 3) THEN
        A(1)=D1(1)
        A(2)=D1(2)
        A(3)=D1(3)
      ELSE
        A(1)=D2(1)
        A(2)=D2(2)
        A(3)=D2(3)
      ENDIF
C      WRITE(*,*) 'Rebar Orientation',A(1),A(2),A(3)
      PR=0.5*CMAG
      TR=1.D-3
      ENDIF
      IF (belongToSet(0, n, 'body_ply').EQV..TRUE.)THEN
C REBAR IN 12 DIRECTION!
      A(1)=B(1)
      A(2)=B(2)
      A(3)=B(3)
C      WRITE(*,*) 'Rebar Orientation',A(1),A(2),A(3)
      PR=0.5*CMAG
      TR=0.12D-3
      ENDIF
      IF (belongToSet(0, n, 'tread_ply') .EQV. .TRUE.) THEN
      IF (NN .LT. 5) THEN
        ALP=20.D0*CON
        CA=DCOS(ALP)
        SA=DSIN(ALP)
        IF (NN .LT. 3) THEN
          A(1)=D1(1)*CA+B(1)*SA
          A(2)=D1(2)*CA+B(2)*SA
          A(3)=D1(3)*CA+B(3)*SA
        ELSE
          A(1)=D2(1)*CA+B(1)*SA
          A(2)=D2(2)*CA+B(2)*SA
          A(3)=D2(3)*CA+B(3)*SA
        ENDIF
        PR=0.3D0*CMAG
      ELSE
        ALP=-20.D0*CON
        CA=DCOS(ALP)
        SA=DSIN(ALP)
        IF (NN .LT. 7) THEN
          A(1)=D1(1)*CA+B(1)*SA
          A(2)=D1(2)*CA+B(2)*SA
          A(3)=D1(3)*CA+B(3)*SA
        ELSE
          A(1)=D2(1)*CA+B(1)*SA
          A(2)=D2(2)*CA+B(2)*SA
          A(3)=D2(3)*CA+B(3)*SA
        ENDIF
        PR=0.7D0*CMAG
      ENDIF

```



```

C      WRITE(*,*) 'Rebar Orientation',A(1),A(2),A(3)
      ENDIF
TR=0.12D-3
ENDIF
RETURN
END

logical function belongToSet (typeTarget, numTarget, setTarget)

implicit real*8 (a-h,o-z)

c      external:
integer      typeTarget      ! must be an ipttyp (see below)
integer      numTarget       ! element number or node number, etc.
                                ! AFTER RENUMBERING!!!!!!
character*(*) setTarget     ! Setname (LOWER CASE!!!)

c      internal:
character*1  name
character*12 setName
dimension   iiname(12)

c      common blocks:
include '/academic/marck62/common/dimen'
include '/academic/marck62/common/setnam'
include '/academic/marck62/common/space'

c In the common block /setnam/, the following variables are defined:
c      ndset:  number of defined Sets
c      nsetmx: maximum number of Sets corresponding parametercard SETNAME
c      (default: nsetmx =10)
c      iptnam: pointer to the Setname. Each Setname takes 12
c              characters and will be stored in integer format.
c      ipttyp: pointer to the set type:
c              ipttyp  Set type
c              0      Elements
c              1      Nodes
c              2      Integration points
c              3      Layers
c              4      Degrees-of-freedom
c              5      Increments
c      iptnum: pointer to the number of elements in set
c      iptloc: pointer to the stored elements in set
c      iptbeg: pointer to all stored elements
c
c
c      write(*,*) 'belongToSet: set type=',typeTarget,
C      -      ' num=',numTarget,' name= ',setTarget,'*'

c      loop over all sets
c      write(*,*) 'nset=',nset,'ndset=',ndset
c      do iset = 1, ndset

      istype = ints (ipttyp + (iset-1))

      if ( istype.eq.typeTarget ) then

      isname = (iptnam +(iset-1)*12)
      do j=1,12
      iiname(j) = ints(isname+j-1)
      write(name,'(A1)') iiname(j)
      setName(j:j) = name

```

```

        if (name .ne. ' ') then
            isnamlen = j
        end if
    end do

    if (setName(1:isnamlen) .eq. setTarget) then
c      write(*,*) 'belongToSet: identified set ', setName(1:isnamlen), '*'

        isnumb = ints (iptnum+iset-1)

        ieptr  = iptbeg + ints (iptloc+iset-1)-1

        do i=1, isnumb
            iexx = ints(ieptr+i-1)
            if (numTarget .eq. iexx) then
                belongToSet = .True.
c          write(*,*) 'belongToSet: matched: type=', typeTarget,
c          -         ' num=', numTarget, ' set=', setTarget
                return
            end if
        end do
        belongToSet = .False.
        return
    endif

end if

end do

write(*,*) 'belongToSet: set ', setTarget, '* not found'
belongToSet = .FALSE.

return
end

```

A.4.2 Rebar Subroutine for 8 Node Continuum Element

During static tire models, the obvious disadvantage of the presented rebar subroutines showed up. All the rebar directions were using the triad formed by nodes 1-2, 1-4 and 1-5 with the modification that the integration points closer to nodes 1 and 4 use 1-9 and other two use 9-2 instead of 1-2 to consider bending. However especially for coarse meshes there are considerable directional differences among the element edges. The difference is due to both sector rotation and deformations. The modification done on rebar subroutines for MARC K7.x family considers the inner tire surface (which may be the face formed by nodes 1-2-3-4 or 1-4-8-5 or 2-1-5-6 that can be selected by user in contrast to MARC K6 versions in which it must be the face formed by nodes 1-2-3-4 only) as the surface to which the rebar layer is similar to. For rebar direction calculations however, the

triad is formed by the three nodal directions which are closest to the integration point are used. In this context, independent of the position of the rebar layer in the element, the inner tire surface is used for the two unit vectors. With the availability of MARC K7 versions, the eight-noded three dimensional rebar elements became available and the tire model is converted to 8 noded solid and rebar elements which produce smaller half-bandwidth and precise solutions in contact. The following rebar subroutine is written for MARC K7 versions and it yields the most precise results because it evaluates the direction cosines of each integration point independently as shown in Figure A.6.

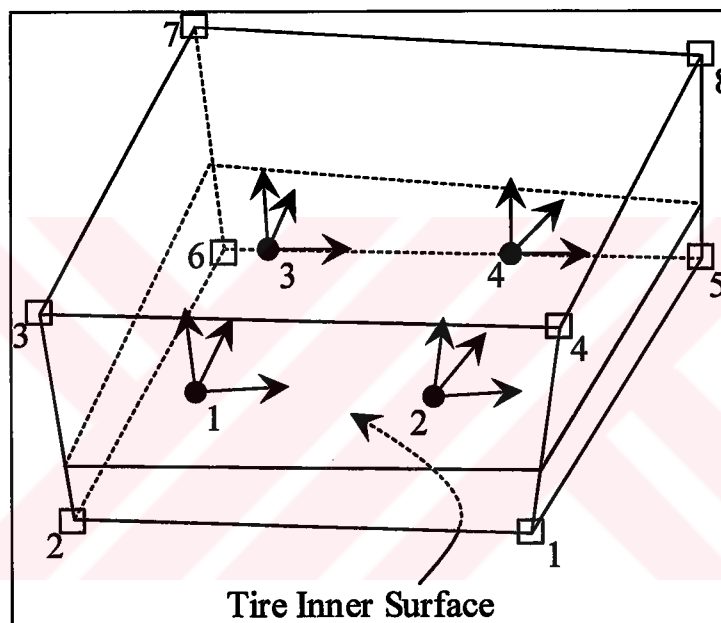


Figure A.6 Triads Determined by Closest Edge

```

SUBROUTINE REBAR (N,NN,T,PR,TR,A)
C VERSION 4.00, 02.07.1998, for 3D Linear Coarse Model!
C !!!new!!! THIS VERSION USES THE NEAREST CORNER TRIAD! !!!new!!!
C CONSIDERS LARGE SECTOR ROTATIONS!
C DETECTS THE ELEMENT SET AND DEFINES REBAR DIRECTION AND THICKNESS ACCORDINGLY!
  IMPLICIT REAL *8 (A-H,O-Z)
  LOGICAL belongToSet
  include '/academic/marck72/marck72/common/blk'
  include '/academic/marck72/marck72/common/dimen'
  include '/academic/marck72/marck72/common/array2'
  include '/academic/marck72/marck72/common/space'
  include '/academic/marck72/marck72/common/elmcom'
  DIMENSION A(3),NN(3),CCNODE(12),DDNODE(12),CURPOS(8,3),
  /S12(3),S14(3),S15(3),S23(3),S26(3),S34(3),S37(3),S48(3),
  /S56(3),S58(3),S67(3),S78(3)

```

```

C DEPENDING ON ELEMENT SET THE REBAR PROPERTIES ARE ASSIGNED BELOW!
  DO 2 II=1,8,1
    LINT=LM(II)
    DO 1 JJ=1,3,1
C THIS DETERMINES INITIAL COORDINATES OF THE NODES
  JRDPRE=0
  CALL VECFTC(CCNODE, VARS (IXORD), NCRDMX, NCRD, LINT, JRDPRE, 2, 1)
C THIS DETERMINES THE DISPLACEMENTS OF THE NODES
  JRDPRE=0
  CALL VECFTC(DDNODE, VARS (IDSXT), NDEGMX, NDEG, LINT, JRDPRE, 2, 5)
  CURPOS(II, JJ)=CCNODE (JJ)+DDNODE (JJ)
C   WRITE (*,*) 'Current Position, Node, DOF:', CURPOS(II, JJ), II, JJ
1 CONTINUE
2 CONTINUE
  DO 3 JJ=1,3,1
    S12 (JJ)=CURPOS (2, JJ)-CURPOS (1, JJ)
    S14 (JJ)=CURPOS (4, JJ)-CURPOS (1, JJ)
    S15 (JJ)=CURPOS (5, JJ)-CURPOS (1, JJ)
    S23 (JJ)=CURPOS (3, JJ)-CURPOS (2, JJ)
    S26 (JJ)=CURPOS (6, JJ)-CURPOS (2, JJ)
    S34 (JJ)=CURPOS (4, JJ)-CURPOS (3, JJ)
    S37 (JJ)=CURPOS (7, JJ)-CURPOS (3, JJ)
    S48 (JJ)=CURPOS (8, JJ)-CURPOS (4, JJ)
    S56 (JJ)=CURPOS (6, JJ)-CURPOS (5, JJ)
    S58 (JJ)=CURPOS (8, JJ)-CURPOS (5, JJ)
    S67 (JJ)=CURPOS (7, JJ)-CURPOS (6, JJ)
    S78 (JJ)=CURPOS (8, JJ)-CURPOS (7, JJ)
  3 CONTINUE
C ELEMENTAL UNIT VECTORS (MAY not BE ORTHONORMAL!!)
C ELEMENT THICKNESS 14 (DMAG)!!
  S12MAG=DSQRT (S12 (1)**2+S12 (2)**2+S12 (3)**2)
  S14MAG=DSQRT (S14 (1)**2+S14 (2)**2+S14 (3)**2)
  S15MAG=DSQRT (S15 (1)**2+S15 (2)**2+S15 (3)**2)
  S23MAG=DSQRT (S23 (1)**2+S23 (2)**2+S23 (3)**2)
  S26MAG=DSQRT (S26 (1)**2+S26 (2)**2+S26 (3)**2)
  S34MAG=DSQRT (S34 (1)**2+S34 (2)**2+S34 (3)**2)
  S37MAG=DSQRT (S37 (1)**2+S37 (2)**2+S37 (3)**2)
  S48MAG=DSQRT (S48 (1)**2+S48 (2)**2+S48 (3)**2)
  S56MAG=DSQRT (S56 (1)**2+S56 (2)**2+S56 (3)**2)
  S58MAG=DSQRT (S58 (1)**2+S58 (2)**2+S58 (3)**2)
  S67MAG=DSQRT (S67 (1)**2+S67 (2)**2+S67 (3)**2)
  S78MAG=DSQRT (S78 (1)**2+S78 (2)**2+S78 (3)**2)
  CON=3.1415926536D0/180.D0
  T=(S14MAG+S23MAG+S67MAG+S58MAG)/4.D0
C NORMALIZE THE VECTORS!
  DO 4 JJ=1,3,1
    S12 (JJ)=S12 (JJ)/S12MAG
    S14 (JJ)=S14 (JJ)/S14MAG
    S15 (JJ)=S15 (JJ)/S15MAG
    S23 (JJ)=S23 (JJ)/S23MAG
    S26 (JJ)=S26 (JJ)/S26MAG
    S34 (JJ)=S34 (JJ)/S34MAG
    S37 (JJ)=S37 (JJ)/S37MAG
    S48 (JJ)=S48 (JJ)/S48MAG
    S56 (JJ)=S56 (JJ)/S56MAG
    S58 (JJ)=S58 (JJ)/S58MAG
    S67 (JJ)=S67 (JJ)/S67MAG
    S78 (JJ)=S78 (JJ)/S78MAG
  4 CONTINUE
  IF (belongToSet (0, n, 'body_ply') .EQV. .TRUE.) THEN
C REBAR IN 12 DIRECTION!
C LAYERS SIMILAR TO 2-1-5-6
  IF (NN(3) .LT. 3) THEN
    A (1)=S12 (1)
    A (2)=S12 (2)
    A (3)=S12 (3)
  ELSE

```

```

      A(1)=S56(1)
      A(2)=S56(2)
      A(3)=S56(3)
    END IF
  C   WRITE(*,*)'Textile:',A(1),A(2),A(3)
      PR=0.1D0*T
      TR=0.287D-3
    ENDIF
  IF (belongToSet(0, n, 'tread_ply') .EQV. .TRUE.) THEN
  C REBAR IN 12-15 PLANE, ALPHA WITH 15!
      IF (NN(2) .LT. 2) THEN
          ALP=20.D0*CON
          PR=0.3D0*T
        ELSE
          ALP=-20.D0*CON
          PR=0.5D0*T
        ENDIF
      CA=DCOS(ALP)
      SA=DSIN(ALP)
      IF (NN(3) .EQ. 2) THEN
          A(1)=S15(1)*CA+S12(1)*SA
          A(2)=S15(2)*CA+S12(2)*SA
          A(3)=S15(3)*CA+S12(3)*SA
        ENDIF
      IF (NN(3) .EQ. 1) THEN
          A(1)=S26(1)*CA+S12(1)*SA
          A(2)=S26(2)*CA+S12(2)*SA
          A(3)=S26(3)*CA+S12(3)*SA
        ENDIF
      IF (NN(3) .EQ. 4) THEN
          A(1)=S15(1)*CA+S56(1)*SA
          A(2)=S15(2)*CA+S56(2)*SA
          A(3)=S15(3)*CA+S56(3)*SA
        ENDIF
      IF (NN(3) .EQ. 3) THEN
          A(1)=S26(1)*CA+S56(1)*SA
          A(2)=S26(2)*CA+S56(2)*SA
          A(3)=S26(3)*CA+S56(3)*SA
        ENDIF
  C   WRITE(*,*)'Tread2:',A(1),A(2),A(3)
      TR=0.162D-3
    ENDIF
  RETURN
  END

```

logical function belongToSet (typeTarget, numTarget, setTarget)

implicit real*8 (a-h,o-z)

```

  C   external:
      integer      typeTarget      ! must be an ipttyp (see below)
      integer      numTarget        ! element number or node number, etc.
                                   ! AFTER RENUMBERING!!!!!!
      character*(*) setTarget      ! Setname (LOWER CASE!!!)

  C   internal:
      character*1  name
      character*12 setName
      dimension    iiname(12)

  C   common blocks:
      include '/academic/marck72/marck72/common/dimen'
      include '/academic/marck72/marck72/common/setnam'
      include '/academic/marck72/marck72/common/space'

```

```

c In the common block /setnam/, the following variables are defined:
c   ndset:   number of defined Sets
c   nsetmx:  maximum number of Sets corresponding parametercard SETNAME
c   (default: nsetmx =10)
c   iptnam:  pointer to the Setname. Each Setname takes 12
c           characters and will be stored in integer format.
c   ipttyp:  pointer to the set type:
c           ipttyp Set type
c             0   Elements
c             1   Nodes
c             2   Integration points
c             3   Layers
c             4   Degrees-of-freedom
c             5   Increments
c   iptnum:  pointer to the number of elements in set
c   iptloc:  pointer to the stored elements in set
c   iptbeg:  pointer to all stored elements
c
c
c   write(*,*) 'belongToSet: set type=',typeTarget,
c -   '   num=',numTarget,'   name= ',setTarget,'*'
c
c loop over all sets
c   write(*,*) 'nset=',nset,'ndset=',ndset
c   do iset = 1, ndset
c
c     istype = ints (ipttyp + (iset-1))
c
c     if ( istype.eq.typeTarget ) then
c
c       isname = (iptnam +(iset-1)*12)
c       do j=1,12
c         iiname(j) = ints(isname+j-1)
c         write(name,'(A1)') iiname(j)
c         setName(j:j) = name
c         if (name .ne. ' ') then
c           isnamlen = j
c         end if
c       end do
c
c       if (setName (1:isnamlen) .eq. setTarget) then
c         write(*,*) 'belongToSet: identified set *'
c -         ,setName(1:isnamlen),'*'
c         isnumb = ints (iptnum+iset-1)
c
c         ieptr = iptbeg + ints (iptloc+iset-1)-1
c         do i=1, isnumb
c           iexx = ints(ieptr+i-1)
c           if (numTarget .eq. iexx) then
c             belongToSet = .TRUE.
c             write(*,*) 'belongToSet: matched: type=',typeTarget,
c -             '   num=',numTarget,'   set=',setTarget
c             return
c           end if
c         end do
c         belongToSet = .FALSE.
c         return
c       endif
c     end if
c   end do
c   write(*,*) 'belongToSet: set ',setTarget,'* not found'
c   belongToSet = .FALSE.
c   return
c end

```

APPENDIX B

ANALYSIS OPTIONS IN MARC FOR CORNERING ANALYSIS

Parameter	Value	Comments
Loadcase	Inflation	
Convergence Testing	Relative, 0.1 N/N	
Adaptive Loading	Equilibrium	
Max # Increments	50	
Desired # of Recycles	3	
Initial Fraction	0.03	
Maximum Fraction	1	
Minimum Load Step Multiplier	0.001	
Maximum Load Step Multiplier	1000	
Minimum Time Step	0	
Solution Control	Full Newton-Raphson	
Contribution of Initial Stress to Stiffness	Full	
Contact Force Removal	Immediate	

Loadcase	Pressing	
Convergence Testing	Absolute, 50 N	Due to large reaction forces at the axle nodes, absolute convergence testing has to be used.
Fixed Loading	18 Steps	
Solution Control	Full Newton-Raphson	
Contribution of Initial Stress to Stiffness	Full	
Contact Force Removal	Immediate	

Loadcase	Rolling	
Convergence Testing	Absolute, 50 N	Due to large reaction forces at the axle nodes, absolute convergence testing has to be used.
Fixed Loading	400 Steps	
Solution Control	Full Newton-Raphson	
Contribution of Initial Stress to Stiffness	Full	
Contact Force Removal	Immediate	

Analysis Options		
Large Displacement	On	
Follower Force	On	
Elasticity Procedure	Large Strain-Total Lagrange	

Job Parameters		
Memory Allocation	25 000 000	Although MARC can dynamically allocate the memory required, for restart purposes using a fixed and conservative amount is preferred.
Element Storage (ELSTO)	On	If ELSTO is off, MARC writes the stiffness matrix that cannot be allocated into physical memory into .t02 automatically, if ELSTO is on, the same data is written into .t03 file.
Bandwidth Optimization	On	This reduces the storage requirements for the stiffness matrix but takes some CPU time before the analysis starts. Since the analysis is rather long, it is preferred to optimize the bandwidth.
State Storage	All Points	Stress state may be stored for all integration points or for centroid.
Solver	Direct Profile	

Contact Control		
Distance Tolerance	0	MARC evaluates the contact tolerance depending on the geometry and for present problem it is less than 0.45 mm.
Distance Tolerance Bias	0	
Deformable-Deformable Method	Single Sided	Since tire does not contact itself during normal operation, to conserve CPU time, the detection of a deformable body touching itself is not checked.
Separation Criteria	Force, 1 N	Separation force, if left blank is taken to be equal to the largest residual force which is not suitable.

Increment	Current	
Chattering	Supressed	
Friction Type	Coulomb	
Method	Nodal Force	
Relative Sliding Velocity	0.001	
Increment Splitting	Iterative	
User Subrotine	r4.f	



REFERENCES

Allen, R.W., Szoatak, H.T., Rosenthal, T.J., Klyde, D.H., 1990. "Field Testing and Computer Simulation Analysis of Ground Vehicle Dynamic Stability". SAE Paper No: 900129.

Allen, R.W., Rosenthal, T.J., Szostak, H.T., 1987. "Steady State and Transient Analysis of Ground Vehicle Handling". SAE Paper No: 870495.

Aston, J.E., Halpin, J.C., Petit, P.H., 1969. "Primer on Composite Materials Analysis", Technomic Publishing Company, Stamford.

Becker, A., Seifert, B., 1997. "Simulation of Wear with a FE Tyre Model Using a Steady State Rolling Formulation". Contact Mechanics III, pp.118-127 Aliabadi, M. H., Samartin, A. (ed.), Computational Mechanics Publications, Southampton, Boston.

Bergman, W., Clemet, H.R., Sheth, N.J., 1971. "Tire Traction Measurement on the Road and in the Laboratory". SAE Paper No: 710630.

Berne, N, 1998. Personal Communication.

Bird, K.D., Martin, J.F., 1973. "The Calspan Tire Research Facility: Design, Development , and Initial Test Results". SAE Paper No: 730582.

Cortese, A.D., Rockafellow, C.S., 1971. "General Motors Proving Ground Tire Cornering Test Vehicle". SAE Paper No: 710092.

Crolla, D.A., El-Razaz, A.S.A., 1987. "A Review of Combined Lateral and Logitudinal Force Generation of Tyres on Deformable Surfaces". Journal of Terramechanics, v. 24, pp. 199-225.

Davis, P. A. , 1997. "Quasi-Static and Dynamic Response Characteristics of F-4 Bias-Ply and Radial-Belted Main Gear Tires". NASA Technical Paper 3586.

Davisson, J.A., 1968. "Test Methods for Evaluating Tire Traction". SAE Paper No: 680136.

Du, X. W., Wei, Y. T., 1998. "Non Linear Finite Element Methodology for Structural Analysis, Rolling Loss and Temperature Field Prediction of Steady Rolling Tires". Presented in the 17th Annual Meeting and Conference on Tire Science and Technology, Akron.

Dugoff, H., Brown, B.J., 1970. "Measurement of Tire Shear Forces". SAE Paper No: 700092.

Fancher, P.S.Jr., Bareket, Z., 1993. "Including Roadway and Tread Factors in a Semi-Empirical Model of Truck Tyres". Tyre Models for Vehicle Dynamics Analysis, Proceedings of 1st International Colloquium on Tyre Models for Vehicle Dynamics Analysis Supplement to Vehicle System Dynamics v.21. Swets and Zeitlinger, Amsterdam, pp.92-107.

Faria, L.O., Oden, T.J., Yavari, B., Tworzydlo, W.W., Bass, J.M., Becker, E.B., 1992. "On the Contact Problem of Tires Including Friction". Tire Science and Technology, v. 13, pp. 111-123.

Gelten, C. J. M., Jong, J. E., 1984. "A Method to Redefine a Finite Element Mesh and Its Application to Metal Forming and Crack Growth Analysis". MARC, Volume F, Part 2, Background Information, MARC Analysis Research Corporation, California.

Gim, G., Nikraves, P.E., 1990. "An Analytical Model of Pneumatic Tires for Vehicle Dynamic Simulations. Part 1: Pure Slips". International Journal of Vehicle Design, v. 11, n. 6, pp. 589-618.

Gim, G., Nikraves, P.E., 1991a. "An Analytical Model of Pneumatic Tires for Vehicle Dynamic Simulations. Part 2: Comprehensive Slips". International Journal of Vehicle Design, v. 12, n. 1, pp. 19-39.

Gim, G., Nikraves, P.E., 1991b. "An Analytical Model of Pneumatic Tires for Vehicle Dynamic Simulations. Part 3: Validation Against Experimental Data". International Journal of Vehicle Design, v. 12, n. 2, pp. 217-228.

Green, A. E., Zerna, W., 1960. "Theoretical Elasticity". Oxford at the Clarendon Press.

Green, A. E., Adkins, J. E., 1960. "Large Elastic Deformations and Non-linear Continuum Mechanics". Oxford at the Clarendon Press.

Helnwein, P., Liu, Ch. H., Meshke, G., Mang, H. A., 1993. "A New 3-D Finite Element Model for Cord-Reinforced Rubber Composites-Application to Analysis of Automobile Tires". *Finite Elements in Analysis and Design*, v. 4, pp. 1-16.

Herrmann, L. R., 1965. "Elasticity Equations for Incompressible and Nearly Incompressible Materials by a Variational Theorem". *AIAA*, v. 3, n. 10, pp. 1896-2000.

Holloway, D.C., Drach, T.J., Mohanty, B., 1991. "An Experimental Investigation of Passenger Car Tire Properties at High Slip and Camber Angles". SAE Paper No: 910233.

Huncler, C.J., Yang, T.Y., Soedel, W., 1983. "A Geometrically Nonlinear Shell Finite Element for Tire Vibration Analysis". *Computers and Structures* v. 17, pp. 217-225.

İpek, Ş., 1969. "Taşıt Mekaniği" Orta Doğu Teknik Üniversitesi Mühendislik Fakültesi Yayın No: 23, Ankara.

Jenkins, J. T., 1982. "The Circumferential Contact Problem for the Belted Radial Passenger Car Tire". *Vehicle System Dynamics*, v. 11, pp. 325-343.

Karafiath, L.L., 1986. "Tire-Soil Interaction Models for Turning (Steered) Tires". *Journal of Terramechanics*, v. 23, pp. 153-169.

Kennedy, R. H., Patel, H. P., McMinn, M. S., 1981. "Radial Truck Tire Inflation Analysis: Theory and Experiment". *Rubber Chemistry and Technology*, v. 54, pp. 751-766.

Kennedy, R., Padovan, J., 1987. "Finite Element Analysis of Steady and Transiently Moving/Rolling Nonlinear Viscoelastic Structure - II. Shell and Three-Dimensional Simulations". *Computers and Structures*, v. 27, pp. 259-273.

Krivetsky, A., 1957. "How to Plot and Read a Carpet Curve". *Product Engineering*, pp. 127-129.

Langer, J.W., Potts, G.R., 1980. "Development of a Flat Surface Tire Testing Machine". SAE Paper No: 800245.

Leister, G., 1997. "New Procedures for Tyre Characteristic Measurement". *Tyre Models for Vehicle Dynamics Analysis, Proceedings of 4th International Colloquium on Tyre Models for Vehicle Dynamics Analysis Supplement to Vehicle System Dynamics* v. 25. Swets and Zeitlinger, Amsterdam, pp. 714-730.

Limpert, R. ,1982. "Vehicle System Components, Design and Safety". John Wiley and Sons, New York.

Loeb, J.S., Guether, D.A., Chen, H.H.F., Ellis, J.R., 1990. "Lateral Stiffness, Cornering Stiffness and Relaxation Length of Pneumatic Tire". SAE Paper No: 900129.

Maalej, A.Y., Guenther, D.A., Ellis, J.R., 1989. "Experimental Development of Tyre Force and Moment Models". International Journal of Vehicle Design, v. 10, n.1, pp. 34-50.

Malvern, L. E., 1969. "Introduction to the Mechanics of a Continuous Medium", Englewood Cliffs, New Jersey.

Mason, A. J., Tanner, J. A., 1997. "Quasi-Static Viscoelastic Loading Measurements of an Aircraft Tire". NASA Technical Memorandum 4779.

Nakajima, Y., Padovan, J., 1987. "Finite Element Analysis of Steady and Transiently Moving/Rolling Nonlinear Viscoelastic Structure - III. Impact/Contact Simulations". Computers and Structures, v. 27, pp. 275-286.

Nakajima, Y., Kadowaki, H., Kamegawa, T., Ueno, K., 1998. "Application of Neural Network for Optimization of Tire Design". Presented in the 17th Annual Meeting and Conference on Tire Science and Technology, Akron.

Ngo, D., Scordelis, A. C., 1967. "Finite Element Stress Analysis of Reinforced Concrete Beam", Journal of American Concrete Institute, v. 64, pp. 152-163.

Noor, A.K., Tanner, J.A., 1985. "Tire Modeling and Contact Problems-Advances and Trends in the Development of Computational Models for Tires". Computers and Structures, v.20, pp. 517-533.

Nordeen, D.L., Cortese, A.D., 1964. "Force and Moment Characteristics of Rolling Tires". SAE Transactions, v.72, pp.325-336.

Osswald, T. A., Menges, G., 1996. "Materials Science of Polymers for Engineers". Carl Hanser Verlag, Kösel, Kempten Germany.

Pacejka, H.B., Bakker, E, 1993. "The Magic Formula Tyre Model". Tyre Models for Vehicle Dynamics Analysis, Proceedings of 1st International Colloquium on Tyre Models for Vehicle Dynamics Analysis Supplement to Vehicle System Dynamics v.21. Swets and Zeitlinger, Amsterdam, pp. 1-18.

Padovan, J., 1987. "Finite Element Analysis of Steady and Transiently Moving/Rolling Nonlinear Viscoelastic Structure - I. Theory". *Computers and Structures* v.27, pp. 249-257.

Padovan, J., Paramadilok, O., 1985. "Tire Modeling and Contact Problems-Transient and Steady State Viscoelastic Rolling Contact". *Computers and Structures*, v. 20, pp. 545-553.

Padovan, J., Tovachakchaikul, S., Zeid, I., 1984. "Finite Element of Steadily Moving Contact Fields". *Computers and Structures*, v. 18, pp. 191-200.

Padovan, J., Zeid, I., 1979. "On the Development of Traveling Load Finite Elements". *Computers and Structures*, v. 12, pp. 77-83.

Padovan, J., Ni, J. F., 1998. "Modeling the Local Mechanics of Twisted Cord Rubber Composites". Presented in the 17th Annual Meeting and Conference on Tire Science and Technology, Akron.

Parratt, N.J., 1972. "Fibre Reinforced Materials Technology", Van Nostrand Reinhold Company, London.

Pottinger, M.G., Marshall, K.D., Arnold, G.A., 1976. "Effects of Test Speed and Surface Curvature on Cornering Properties of Tires". SAE Paper no: 760029.

Pottinger, M. G., 1992. "The Three-Dimensional Contact Patch Stress Field of Solid and Pneumatic Tires". *Tire Science and Technology*, v. 20, pp. 3-32.

Richards, T., Charek, L.T., Scavuzzo, R.W., 1986. "The Effects of Spindle and Patch Boundary Conditions on Tire Vibration Modes". SAE Paper No: 860243.

Ridha, R.A., Satyamurthy, K., Hirscheft, L.R., 1985. "Finite Element Modeling of a Homogenous Pneumatic Tire Subjected to Footprint Loadings". *Tire Science and Technology*, v. 13, pp.91-110.

Rothert, H., Idelberger, H., Jacobi, W., Laging, G., 1985. "On the Contact Problem of Tires Including Friction". *Tire Science and Technology*, v. 13, pp. 111-123.

Sakai, H., 1981. "Theoretical and Experimental Studies on the Dynamic Properties of Tires, Part 1: Review of Theories of Rubber Friction". *International Journal of Vehicle Design*, v. 2, pp. 78-109.

Schieschke, R., Hiemenz, R., 1993. "The decisive Role the Quality of Tyre Approximation Plays in Vehicle Dynamics Simulations". Tyre Models for Vehicle Dynamics Analysis, Proceedings of 1st International Colloquium on Tyre Models for Vehicle Dynamics Analysis Supplement to Vehicle System Dynamics v.21. Swets and Zeitlinger, Amsterdam, pp. 156-166.

Seifert, B., 1998. Personal Communication.

Snymann, M. F., 1998 "Tire Modeling using Finite Element Code ABAQUS" Presented in the 17th Annual Meeting and Conference on Tire Science and Technology, Akron.

Stocker, M., 1991. "A Giant Stride in Tire Testing". Automotive Engineering v. 99, n. 4, pp.29-31.

Stribersky, A., Fancher, P.S., 1989. "The Nonlinear Behavior of Heavy-Duty Truck Combinations with respect to Straightline Stability". Journal of Dynamic Systems, Measurement and Control, v. 111, pp. 577-582.

Tanner, J. A., 1996a. "Computational Methods for Frictional Contact with Applications to the Space Shuttle Orbiter Nose-Gear Tire, Comparisons of Experimental Measurements and Analytical Predictions". NASA Technical Paper 3573.

Tanner, J. A., 1996b. "Computational Methods for Frictional Contact with Applications to the Space Shuttle Orbiter Nose-Gear Tire, Development of Frictional Contact Algorithm". NASA Technical Paper 3574.

Tekkaya, A. E., 1991. ME 580 Finite Element Analysis Lecture Notes (Unpublished).

Tekkaya, A. E., 1994. ME 581 Finite Element Analysis in Solid Mechanics Lecture Notes (Unpublished).

Tönük, E., Ünlüsoy, Y. S., 1995a. "Simple Analytic Tire Models for Vehicle Dynamic Simulations, Part I: Models" (in Turkish). 7th National Machine Theory Symposium, İstanbul pp. 606-615.

Tönük, E., Ünlüsoy, Y. S., 1995b. "Simple Analytic Tire Models for Vehicle Dynamic Simulations, Part II: Benchmarking" (in Turkish). 7th National Machine Theory Symposium, İstanbul pp. 616-623.

Turner, J. L., Nakajima, Y., Branca, T. R., Kelsey, S., 1998. "A 3D Finite Element Modeling Approach for Simulation of Steady State Tire Rolling".

Presented in the 17th Annual Meeting and Conference on Tire Science and Technology, Akron.

Ünlüsoy, Y. S., 1993. "Automotive Engineering II". Unpublished Lecture Notes.

Walter, J.D., 1978. "Cord-Rubber Composites : Theory and Applications", Rubber Chemistry and Technology, v. 51, pp. 524-576.

Watanabe, Y., Kaldjian, M. J., 1983. "Modeling and Analysis of Bias-Ply Motorcycle Tires". Computers and Structures, v. 17, pp. 653-658.

Weber, R., Persch, H.G., 1976. "Frequency Response of Tires-Slip Angle and Lateral Force". SAE Paper No: 760030.

Wong, J. Y., 1978. "Theory of Ground Vehicles", John Wiley and Sons, New York.

Zegelaar, P. W. A., Pacejka, H. B., 1996. "The In-Plane Dynamics of Tyres on Uneven Roads". Tyre Models for Vehicle Dynamics Analysis, Proceedings of 6th International Colloquium on Tyre Models for Vehicle Dynamics Analysis Supplement to Vehicle System Dynamics v. 27. Swets and Zeitlinger, Amsterdam, pp. 22-36.

Zeid, I, Padovan, J., 1981. "Finite Element Modeling of Rolling Contact". Computers and Structures, v. 14, pp. 163-170.

-, 1994a. "ABAQUS/Pre User's Manual Volume II", Hibbitt, Karlsson & Sonensen, Inc., Pawtucket.

-, 1994b. "ABAQUS/Standard User's Manual Volume I, Version 5.4", Hibbitt, Karlsson & Sonensen Inc., Pawtucket.

-, 1995. "ABAQUS Theory Manual, Version 5.5", Hibbitt, Karlsson & Sonensen Inc., Pawtucket.

-, 1998. "ABAQUS/Standard User's Manual Version 5.8 Draft", Personal Communication with Michael Snyman of Hibitt, Karlsson & Sonensen Inc.

-, 1996. "User's Manual for BERTEC Force Plate # N60506 Type 4040A". BERTEC Corporation, Worthington.

-, 1994a. "MARC, Volume B, Element Library Rev. K6", MARC Analysis Research Corporation, California.

- , 1997a. "MARC, Volume A, User Information Version K7", MARC Analysis Research Corporation, California.

- , 1997b. "MARC, Volume B, Element Library Version K7", MARC Analysis Research Corporation, California.

- , 1984a. "MARC, Volume F, Part 1, Background Information", MARC Analysis Research Corporation, California.

- , 1984b. "MARC, Volume F, Part 2, Background Information", MARC Analysis Research Corporation, California.

- , 1996. "MARC, Nonlinear Finite Element Analysis of Elastomers", MARC Analysis Research Corporation, California.

- , 1990. "PCL-718 High Performance Data Acquisition Card User's Manual". Advantech Co. Ltd., Taiwan.

- , 1993. "User's Guide for the Vector Type V1100-7500 Drives for Standard AC Squirrel Cage Induction Motors". Control Techniques, Leutenbach.

Web Sites

- , 1997. "Michelin Web Site", <http://www.michelin.com/>

- , 1996a. "Goodyear School Kit", <http://www.goodyear.com.au/school/index.html>

- , 1996b. "Goodyear Online", <http://www.goodyear.com/>

CURRICULUM VITAE

Ergin Tönük is born in Ankara on March 31, 1968. He received his B. S. degree in Mechanical Engineering Department of Middle East Technical University as a honor student in 1990. In the same year he started to work as a research assistant in the same Department. He finished his M. S. thesis having the title “Synthesis of Coupler Curves of Mechanisms by Pattern Recognition Techniques” in 1992. In the same year he started his Ph. D. work on “Computer Simulation of Dynamic Behavior of Pneumatic Tires” in the Department of Mechanical Engineering. In 1994 he received The Scientific and Technical Research Council of Turkey (TÜBİTAK) Münir Birsal Foundation Ph. D. Scholarship. In 1998, he received The Scientific and Technical Research Council of Turkey (TÜBİTAK) NATO B-1 post doctoral research fellowship. His main areas of interest are, computer simulation and experimental verification of dynamic behavior of pneumatic tires, finite element analysis, analysis and synthesis of mechanisms, machine dynamics, computer aided mechanical system analysis, computer aided theory and dynamics of machines education. His publications are as follows.

Söylemez, E., Tönük, E., 1990. “Optimum Design of Piston Driven High Swing Linkages” (in Turkish). 4th National Machine Theory Symposium, pp. 211-220, Yalova.

Söylemez, E., Tönük, E., 1991. "Function Synthesis with Optimum Force Transmission Characteristics on Spatial Right-Angled Four Bar Mechanisms" (in Turkish). 5th National Machine Theory Symposium, pp. 81-90, Bursa

Tönük E., Söylemez, E., 1992. "Synthesis of Coupler Curves using Pattern Recognition Techniques" (in Turkish). 5th National Machine Design and Production Conference, pp.201-208, Ankara.

Söylemez, E., Tönük, E., 1993. "Design of Piston Driven Six-Link Mechanisms with Large Swing Angle and Optimum Transmission". The 6th IFToMM International Symposium on Linkages and Computer Aided Design Methods v. 1, pp.301-308.

Tönük, E., Ünlüsoy, Y. S., 1995. "Simple Analytic Tire Models for Vehicle Dynamic Simulations: 1. Models" (in Turkish). 6th National Machine Theory Symposium, pp. 606-614. İstanbul.

Tönük, E., Ünlüsoy, Y. S., 1995. "Simple Analytic Tire Models for Vehicle Dynamic Simulations: 2. Verification Against Experimental Data" (in Turkish). 6th National Machine Theory Symposium, pp. 615-623 İstanbul.

Tönük, E., Ünlüsoy, Y. S., 1995. "Modeling of Inflation and Loading of Pneumatic Tires by Finite Element Analysis" (in Turkish). Journal of Machine Design and Production, v. 3, pp.30-34.

Tönük, E., Ünlüsoy, Y. S., 1996. "Static Finite Element Modeling of Radial Pneumatic Tires" (in Turkish). 2nd National Computational Mechanic Symposium, Trabzon, pp.101-110.

Tönük, E., Ünlüsoy, Y. S., 1998. "Static Finite Element Modeling of Radial Automobile Tires". Presented in the 17th Annual Meeting of Tire Society in Akron, April 28-29.

Söylemez, E., Tönük, E., 1998. "Design of Draft Pipes in Hydroelectric Power Plants". Accepted for the 8th International Machine Design and Production Conference to be held in Ankara in September 9-11.

